2018

Developments in static and pulsed magnetic field systems for detection of magnetic resonance in non-uniform magnetic fields

Neelam Prabhu Gaunkar
Iowa State University

Developments in static and pulsed magnetic field systems for detection of magnetic resonance in non-uniform magnetic fields

by

Neelam Prabhu Gaunkar

A dissertation submitted to the graduate faculty

in partial fulfillment of the requirements for the degree of

DOCTOR OF PHILOSOPHY

Major: Electrical Engineering

Program of Study Committee:
David C. Jiles, Major Professor
Mani Mina
Robert Weber
Gary Tuttle
Arun Somani

The student author, whose presentation of the scholarship herein was approved by the program of study committee, is solely responsible for the content of this dissertation. The Graduate College will ensure this dissertation is globally accessible and will not permit alterations after a degree is conferred.

Iowa State University

Ames, Iowa

2018

DEDICATION

....because at the end of the day it is the belief that matters. This thesis, my journey so far and countless memories are all because my family, friends and colleagues believed in me. Their care, patience and belief in me, even when I didn't seem to have any helped me grow both professionally and personally. I would like to dedicate this work to my family and my mentors, at home and at school. Finally, I would like to dedicate this to two people who weren't able to see the entirety of this journey, my mother Dr. Gita Prabhu Gaunkar and Professor Robert Weber.

TABLE OF CONTENTS

Page

LIST OF TABLES

Page

LIST OF FIGURES

Page

ACKNOWLEDGEMENTS

I have very special memories associated with ISU, the departmental community, my community from Durham third floor. People who have enabled me to be "me" and helped me take my first steps towards becoming an independent thinker, researcher and human.

Expressions and support appeared in different forms over the years. Several defining moments of kindness, honesty, humor, grief, success and uncertainty led to new connections, perspectives and relations. I value these and the people who were willing to spend time and effort all through. In no particular chronology/preference I would like to thank the following people.

Prof. David Jiles for his kindness, constant support, encouragement and belief in what I can or could do. The responsibility of being the student of a world-renowned professor is enormous, I am not sure I could do any justice to his greatness nor to his humbleness. As an equal participant in my journey, Prof. Mani Mina for watching out for me at every step, assisting me in redefining my approach to learning, research, people and education. He helped me make thinking a habit, made me define my comfort in who I was and what I could do, ultimately becoming a life mentor. His "sense of reality" helped me survive many difficult days when I was minutes away from quitting and giving up. Prof. Robert Weber for the timeless patience and attention to my ideas and approaching circuit design, he taught me once again that with greatness comes great humility. Thank you Prof. Weber for showing me how to keep persevering and to look at things the way the world sends it my way. I have not known a person who can dream and imagine circuits as you do. Prof. John Basart for advice, many many scientific discussions, smiles and spirit along with tips for improvement. He taught us that a happy and positive approach to research was possible at every level of learning. Prof. Gary Tuttle for his sense of humor, insights about circuit design and asking me to do things which I can care about. His care for students and their learning was apparent in each discussion. Prof. Arun Somani for often seeking to know how I am doing, asking me meaningful questions and

helping me update my approach towards my research. He encouraged me to face tough questions with elegance and to take a stand and defend it to the end. Prof. Ryan Gerdes for remotely encouraging me, fueling inspiring ideas and dreams with his vision and consistently leading us to better questions. Prof. Surya Mallapragada and Dr. Metin Uz, for accommodating my request for measurements in their lab and being so collaborative and friendly in their approach to research. Prof. Meng Lu for giving me my first ever A. Prof. James Rossmanith from the math department, for helping me enjoy math and imbibing values of hard work and perseverance. Prof. Jiming Song, for allowing me to come to so many of his classes, even without registering just because I wanted to know more about electromagnetism. Prof. Diane Rover, my Preparing Future Faculty Program (PFF) Mentor, Prof. Holly Bender, Karen Bovenmeyer, Laura Bestler and Prof. Craig Ogilivie to give us hope, show us different learning techniques and inspired us to come out of our shells and try different things. Prof. Verena Paepcke-Hjeltness and industrial design students and colleagues for teaching us engineers to sketchnote and embracing us for who we are. Prof. Goce Trajcevski, for infinite candy supply, his humor and assigning me names like head nun and her neelamness! Many other professors within the department, who have always acknowledged my presence, often treated me as a colleague and cared to inquire about my well-being, academic aspirations and progress within the curriculum. I also thank Prof. Evans, Prof. Biswas and Prof. Rebecca Flint for helping me look at electromagnetism and differential equations from a physicist's perspective.

Within the department I am grateful to several department chairs and DOGE's, for supporting my numerous applications for fellowships (ASNT, IBM and Zaffarano), providing me teaching assistant positions and encouraging me for professional activities. From the departmental staff I am grateful to Student Services for creating opportunities and a social interaction avenue among graduate students. Vicky, for also being a caring parent in a professional setting. I am also thankful for departmental office members Samantha, Sara, Luann, Sherry, Kristin, Paula, Kay, Emily, Sarah, Lori, Ginny and other student assistants for providing timely resources and attention. Sara Harris for knowing many many rules, appreciating our hardships and being helpful at numerous occasions even with submission of scholarship applications at the eleventh hour! I am yet to learn how to

understand her sarcasm but her motivation is commendable. I am also immensely thankful for the resources and insights provided by the ETG group and a special mention to Lee Harker, Jason(s), Matt, Don, Mark and student assistants for timely inputs and resources.

A lot of my work was funded and supported by industrial organizations and mentors. Sasha Oster, for introducing me to her research group at Intel, mentoring me for a summer and showing me that Mani's way of approaching research made lots of sense. Within Intel, Johanna, Teles, Adel and Sasha were a wonderful team to learn from. Emily Kinser, for magically making so many of my applications successful, without her support and funds from IBM, I wouldn't have had an opportunity to learn and explore in the last couple years. Dr. Yiqiao Song, for introducing us to NMR sensors and providing us research funding in the initial years of my PhD. Dr. Irfan Bulu for always being positive and encouraging and Dr. Shin Utsuzawa for showing me that hard work could help you achieve any depth of finesse. All of them showed me aspects of industry which I wouldn't have experienced under normal circumstances.

Several undergraduate, graduate and postgraduate students were involved in my research in different capacities over the past several years. From the magnetics research group, I am thankful to the lab environment and collegiality of my colleagues Lawrence, Orfeas, Helena, Zhen, Yan, Priyam, Xiaojing, Joe, Winnie, Ravi and Ikenna. From the high speed systems group, I want to acknowledge the contributions of Jiayu, Wei Shen, Jayaprakash, Leif, Tom, Sara and Rachel. Wei, Leif, Jiayu, Tom and the design teams have spent infinite hours in the lab just trying to make things "work" and laughing at many mistakes we made. I am also grateful to Robert, John, Sasha, Ryan and all graduates from this lab who have actively and remotely mentored me through different phases of my journey with the group. Gokcen, David, Tara, Zack, Moe, Cassie, Sarah, Bhuwan and Alok for discussions on electromagnetism and making things possible. I will also acknowledge several undergraduate students, senior design teams and mentors who helped me feel connected to my roots as an engineer and reminded me of things I kept forgetting from my undergraduate years.

In my darkest days I always felt welcomed in the labs with the students and could forget some bad times when I worked with them. Similarly, a stream of family and friends helped me be myself

in tough times and made my journey and time in Ames more meaningful and cheerful. Many of them have moved on in life but I cherish shared memories with all. My friends during my Masters, my roommates, my kind neighbors who were there always with a smile, my sports and exercise buddies, my ECpE friends, GoECpE, Sunanda's colleagues and friends, and my cousins, thank you.

As I look back, none of what I have done today could have been possible without help from my core family and friends. My friends while growing up and undergraduate who stood by me in all thick and thin, thank you. You are always in my heart. My family, my mom who always told my dad that she didn't think I needed to go through the hardships of a PhD, for raising me and making me who I am. You were not there to see me in all these years, but we talked about this and I am glad I could do something we talked about at one point of time. I am sure you are watching over me and are always proud of me in everything I do. My father, my greatest support, I admire his thinking, determination and never give-up perspective. He has impacted me and my whole life, making me question who I am and asking me to reflect on my actions time and again. Words fail me as I attempt to thank him for the countless times he has heard me through, encouraged me to keep fighting, supported me through difficult times, tears and failures. I don't think I could come close to being as awesome as he is and continues to be. Thank you for being the champion in my life. These acknowledgments cannot end without a special mention to my sister, Sunanda, my reliable support in all these years. Sunanda, thank you for bringing me here and caring about me at all instances. Thank you for bearing with me through this emotional roller coaster journey. Thank you for being a brave role model, for showing me that one must keep fighting, living life for all it is worth and being more vocal and willing in communicating and sharing ideas. I still have a hard time in many of our conversations because you ask me to think of things I have difficulty in articulating. Thank you thank you thank you for always believing in me. And thank you to Madhur, for seeking to be as interested as you in my everyday tribulations. Both of you have made Chicago, a home away from home and a family that I can reach out to at all points of time.

ABSTRACT

The evolution of wearable diagnostic devices and more importantly, increasing consumer awareness, have demanded advancements in sensing mechanisms, sensor data analysis and data processing. Magnetics technologies such as current sensing, actuation, switching, navigation and data recording have all evolved technologically with the demand of lower operational power and long-term system stability. However, none of these advancements, have incorporated operations in low magnetic fields since these fields are non-uniform, vary spatially and provide low data resolution. In this work, the possibility of sensor operations in low non-uniform magnetic fields is explored. Magnetic fields produced by neodymium iron boron permanent magnets are studied, simulated and tested with portable pulsed field generation systems to demonstrate the capability of detecting magnetic resonance signals in non-uniform DC magnetic fields. Advances in detection capabilities in non-uniform fields will allow multiple new application areas to develop, potentially revolutionizing medical diagnostic procedures.

In this dissertation, we analyze different aspects of a portable magnetic resonance sensor system in detail. We first study magnetic fields produced by different permanent magnet geometries. The spatial magnetic field variations in the magnet's exterior are simulated using finite element methods. In particular, regions of localized field uniformity in the magnet's exterior are identified for ring magnet geometries. Various modifications to ring magnets such as magnet dimensions, inclusion of magnetic inserts, placement of multiple magnets and their orientations are simulated to identify the optimal geometry with maximum magnetic flux density in locally uniform regions.

We next consider the generation of pulsed magnetic fields using portable electronic circuits. Pulsed magnetic fields are needed to initiate the magnetic resonance process. Thus, pulsed fields are used alongside the static fields in magnetic resonance measurements. We discuss design considerations for creating portable pulsed magnetic field circuits, delivering upto 10 A of current

at operational frequencies ranging from 2 - 5 MHz, via design of two prototype circuits. Both these prototype devices rely on application of pulsed sinusoidals to switching devices connected to inductors.

A combination of the static and pulsed magnetic fields constitutes the NMR sensing and detection system that is used to study ferromagnetic and paramagnetic materials. We present measurements from ferromagnetic materials placed in non-uniform magnetic fields with applications in oil-well industry. We also present measurements of paramagnetic materials within organic media. These measurements validate applicability of such portable sensor systems, thereby ushering in varied possibilities for future portable magnetic resonance measurements in low and non-uniform magnetic fields.

CHAPTER 1. INTRODUCTION

Sensors and sensor systems are increasingly becoming an essential part of our daily lives, at home, at work, at recreation, and most of us seem to have some sensing devices with us most of the times. Sensors have thus become ubiquitous, they find applications in the simplest as well as most complex equipments and missions around us. Many sensors are designed and used for measurements of physical parameters such as distance, velocity, acceleration, force, pressure, gravity, electric current, magnetic flux, etc., and include some common examples such as speedometers, accelerometers, strain gauges, pressure gauges,ammeters, fluxmeters, etc. Other types of sensors are used to detect presence of toxins in food items, to detect and measure polluants in air or even to detect tissue anomalies for diagnostics, to monitor key vital signs of patients or in remote sensing, etc. Depending on the sensing mechanisms employed, requirements of external stimulus for their functioning, if any, or their areas of applicability, sensors can be described as proximity sensors that measure distances, as strain gauges that can measure strains and stresses, as thermocouples that measure temperatures, optical sensors that use photo-detectors , magnetic sensors which can sense magnetic fields including magnetic precession, thin-film sensors, bio-sensors, chemical sensors, high temperature sensors or in more advanced versions as smart sensors which in addition to sensing can trigger other devices.

Often a collection of sensors along with additional analog or signal processing devices are assembled together to form special purpose sensor systems. Sensors for detection of forces, fields and acceleration are used in embedded and automotive systems [1, 2, 3]. Some other sensors are designed to operate under harsh environments which may include high temperatures, elevated pressures, exposure to corrosive substances and even variable fields [4, 5, 6, 7, 8]. Such systems, employed in transportation, military hardware, security, communications, health care, medical diagnostics and bio-medical sectors, power generation and even home automation, are capable of acquiring signals,

digitizing and processing data and providing triggers for activation of other devices for further actions. Recent advances in data storage, data analytics together with miniaturization of electronic systems have further propelled the use of portable sensor systems enabling significant advances in their applications. Sensor system designs are optimized for their suitability for certain range of applications taking into account requirements of the quality of performance, durability and also cost whilst trying to provide solutions to address issues of health care, safety, and global environment. There are thus continuing research and development efforts to design, improve designs, enhance range of their applicability whilst controlling costs of the products based on incorporation of advancing technologies, innovations and new concepts for ever increasing demands from simplest to most complex needs in our daily lives.

In this work, special kind of magnetic sensor systems are studied. In magnetic sensor systems, various physical properties are detected indirectly through magnetic field variations. The detection capability of magnetic sensor systems is dependent on the range of magnetic fields being detected. The sensitivity ranges of various magnetic field sensors, from Fig. 1.1, highlight the field detection capabilities for most magnetic sensors. Magnetic sensor systems used to detect nuclear precession are known as magnetic resonance sensor systems. Such sensor systems operate in the presence of static external magnetic fields [7, 9] making the signal detection process more involved.

In the present work, studies on a portable nuclear magnetic resonance (NMR) system has been undertaken. A simple, systematic and robust approach has been adopted to understand the existing systems and develop a new design of a complete sensor system. The portable and cost effective NMR unit consists on one hand relatively simple probes and on the other hand original solutions for suitable accompanying electronics. Validation of the proof of concept device is illustrated through measurements on representative targets available thus demonstrating an affordable, portable NMR system for medical diagnostics operating in non-uniform magnetic fields.

In the body of this thesis work the design, development and measurements from a sensor system which may be used in varied nuclear magnetic resonance applications will be discussed. The design is optimized for each parameter which can affect NMR signal detection capabilities of

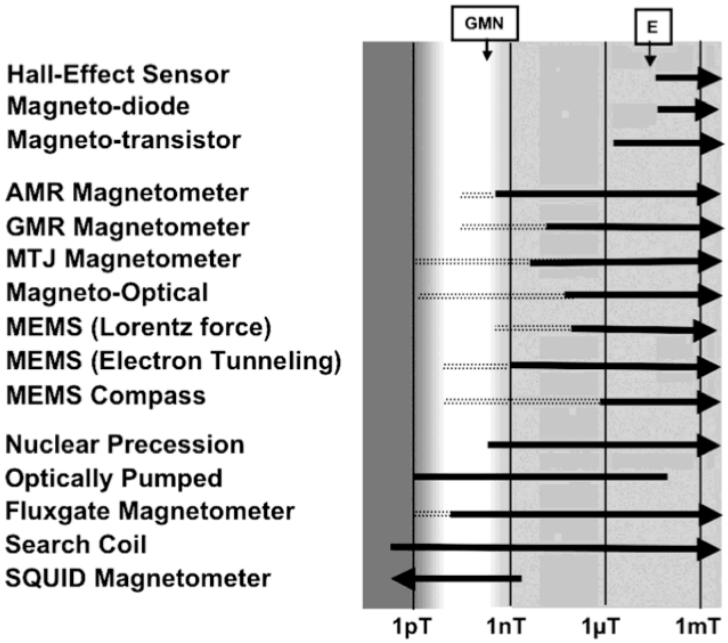

Figure 1.1: Magnetic field sensitivity ranges for varied magnetic sensors [10]. Here GMN corresponds to geomagnetic noise and E corresponds to Earth's magnetic field.

the sensor system. Additionally the effect of non-uniform external static fields on the operation of nuclear magnetic resonance sensors is examined in great detail. Furthermore the utility of magnetic resonance sensors in non-invasive characterization and evaluation of certain representative target materials inclusive of organic matter is explored. An approach of obtaining magnetic resonance signals in spatially varying static magnetic field is proposed and the conditions for its successful operation has been identified.

The key contributions of this work thus include primarily the conceptualization, design, development, measurements, testing of different magnetic sensors and associated magnetic field generation systems. This dissertation also includes a background review, simulations, experimental measurements and analysis needed to understand the sensor system operations.

As a summary, in this chapter, the need for designing a portable magnetic resonance sensor system operating in non-uniform magnetic fields, relevant challenges and possible avenues for further advancement to adapt the system for low cost, portable NMR for diagnostic and analytical applications will be reviewed.

1.1 Research Motivation

Magnetic field sensor systems are used for numerous applications [10, 11, 12, 13]. Many magnetic field sensors include materials which are sensitive to changes in magnetic fields or devices which respond to such changes [14, 15]. Some sensors can operate in the presence of uniform magnetic fields [9] while some might operate under non-uniform magnetic fields [7]. In fact, some applications [16, 17] where non-uniform magnetic fields may be present, modify their sensor design to nullify effects of magnetic field variations. In other applications, different techniques of pulse sequencing [18, 19] or gradient fields [20, 21] are employed.

A question that may arise is why magnetic measurements are difficult in presence of non-uniform magnetic fields. Besides single-sided nuclear magnetic resonance (NMR) applications [22, 23] where non-uniform magnetic fields are pre-dominantly present, field non-uniformities can cause variations in magnetization within bulk samples: in some cases there might be localized regions of magnetization and in some others limited regions of magnetization may occur. Nonetheless, there are certain applications where field non-uniformity is incorporated and taken into account during measurements [24, 25, 26]. Two well known applications are magnetic resonance imaging (MRI) and oil-well logging. While both applications require different measurement protocols, the presence of a uniform external static magnetic field is vital in both[18, 27]. MRI systems create precise field non-uniformity to obtain contrast in images of human tissue [28, 29]. Meanwhile, oil well measurements use different ways to overcome non-linear effects introduced by non-uniform magnetic fields [23].

Since static field non-uniformity is a huge roadblock to design of portable magnetic resonance sensor systems, exploration of new designs utilizing the magnetic field non-uniformity in magnetic sensing applications would greatly enable utility of such sensors in practical application. With this background, our main focus throughout this work will be on developing an understanding of the non-uniform nature of magnetic fields generated by unilateral (or single-sided) NMR sensor systems, determining the field perturbation (if any) introduced by objects placed in such fields and eventually developing a prototype system that incorporates magnetic field non-uniformity

introduced by magnets. It is our hope that these findings will contribute to improvements in non-invasive and portable diagnostics at several medical facilities.

1.2 Magnetic resonance sensors

Magnetic resonance sensors are designed to detect energy exchanges at resonant frequencies [30, 31]. Such sensors can detect resonance at macroscopic and microscopic scales [32]. The phenomenon of nuclear magnetic resonance (NMR), first discovered in the 1950's, has been of considerable value in several applications [33] particularly to the petro-chemical and medical industries. To further understand the design of magnetic resonance based sensors, a brief background about the major milestones in the evolution of nuclear magnetic resonance are discussed.

1.2.1 Evolution of magnetic resonance

Pioneering work by Rabi, Bloch and Purcell [34] led to the discovery that nuclei, such as ^{1}H or ^{15}P absorbed certain frequencies of RF energy in presence of an external magnetic field. Energy absorption occurred when the nuclei were considered to be in a state of magnetic resonance. Furthermore, the structural and chemical information about the molecule was determined [35] through it's signal emissions. For several years, the technique of NMR was then used for chemical spectroscopy and material identification. From this period until early 1970's, different pulse sequences were also designed, probably the most significant of these were from Hahn and Carr in the 1950's [36]. During this time, the oil industry was also actively engaged in using the NMR technique to detect porous structures within ground formations, measuring relaxation and diffusion times. Efforts were also in place to obtain NMR signals from living animals, humans and detect human blood flow. In 1971, Damadian demonstrated that the NMR relaxation times of tissues and tumors differed [37]. Eventually, Lauterbur published the first nuclear magnetic resonance image (now recognized as an MRI) and the first cross sectional image of a live mouse and other organic matter[38, 39].

The technique of NMR was further extended to image the human body during the 1980's. GE Research established the first human body scanner using a 1.5 T external magnet system [40]. Through the 1990's further improvements in the signal optimization and localization were achieved. Higher field MRI machines were created to obtain higher sensitivity and improvements in spatial resolution [41, 42, 43].

Over the last few decades, NMR and MRI have metamorphosed into integral investigation techniques. Magnetic resonance imaging (MRI) or nuclear magnetic resonance (NMR) is being employed to visualize the condition of the tissues and other internal organs. Many MRI systems operate at high uniform magnetic fields (1-10 T or more) and are designed to adjust for gradients in magnetic field. The technique allows a wide variety of radiofrequency pulse sequences which may be used to examine different parts of the human body [44, 45], or image malignant/non-malignant tissues [46] and detect anomalies such as tumors [47]. Medical facilities are increasingly rely on MRI scans as diagnostic tools for neuroimaging, musculoskeletal imaging, fetal imaging, cardiac imaging etc. [48, 49]. More recently, functional MRI (fMRI) is being used to determine brain activity during different actions[50, 51]. However, accurate measurements including size or nature of tumors etc. require longer measurement time and finer measurements using more elaborate techniques [52]. In addition, NMR spectroscopy of complex chemical species, organic compounds, proteins, nucleic acids and even DNA sequences have been obtained[53, 54]. Additionally, the oil industry now utilizes portable, wireless and surface tools. Techniques such as logging while drilling and in-situ detection of rock porosity are observed [55, 56].

1.2.2 Major challenges in magnetic resonance applications

With a focus on the relevant applications, magnetic resonance based imaging and spectroscopy have both evolved into mature techniques. Furthermore, with improvements in signal acquisition and processing several portable systems are found in the markets for non-invasive evaluation of cement, biodegradable materials, wood, paintings, plants etc [23, 57].

While data acquisition and signal processing capabilities have advanced rapidly, modifications in the measurement methods have not been as rapid. In fact, most magnetic resonance experiments still require the presence of a uniform homogeneous static magnetic field [18] for reliable interpretations. Minor variations in the magnetic field strength cause peak broadening in spectroscopy applications and affect spatial resolution of magnetic resonance images [18]. Thereafter, non-uniform magnetic fields haven't been considered to be effective for use in medical applications. However, known field gradients are applied in MRI systems to obtain greater image clarity and resolution. Contrary to medical applications, all NMR operations in the oil industry use a non-uniform magnetic field since the region of investigation is external to the sample. Then, is there a possible merger between the two measurement methods i.e. can non-uniform fields be utilized for medical applications ushering in a whole new opportunity for portable diagnostics?

Before considering possible modifications of magnetic field non-uniformity, it is vital to discuss aspects of spatial resolution and signal to noise ratio (SNR) in nuclear magnetic resonance experiments. In conventional NMR, the strength of the externally applied static magnetic field ,B_0, relates to both the spatial resolution and SNR. Additionally, the spatial resolution depends on the magnetic field gradients, ΔB_0. Thereafter, the SNR of NMR measurements is found to be proportional to the strength and homongeneity of the field based on [58]:

$$SNR \propto {B_0}^2 \propto \frac{1}{\Delta B_0} \tag{1.1}$$

From equation 1.1 it is seen that a high static magnetic field and low variations in the field gradient are considered to be necessary conditions for achieving high SNR in conventional NMR measurements. Ideally, device performance may be improved by changing either of these factors. The best case may be to increase the static field strength and minimize the non-uniformity at the same time. Other parameters such as number of nuclear spins and spin transitions, size of sensitive region etc. also play an important role in NMR signal detection [45]. The presence of field non-uniformity affects the SNR significantly. Thereafter alternative methods of obtaining NMR signals in non-uniform fields are established. These are discussed in upcoming sections.

1.2.3 Initial efforts in unilateral NMR

There are some applications where NMR may be detected in non-uniform magnetic fields with low spatial accuracy [59, 60, 61]. Unilateral NMR is one such technique. Probably the most extensive work in the area of unilateral (single-sided and non-uniform) NMR, single-side magnet designs and open geometries originate in the oil well logging industry. The oil industry needed mobile instruments that could detect rock porosity and oil/water in ground formations [23, 62]. In the early 1950's - 1970's researchers at Chevron [63], Schlumberger [64], Mobil [65], Shell [66] and other oil companies worked on designing NMR based borehole logging instrumentation, developing an understanding of NMR measurement of fluids in rocks and relationships between NMR signal decay times and rock pore sizes [67]. Due to large measurement depths and excessive power consumption the oil industry did not use coils to generate static magnetic fields. Instead, permanent magnet assemblies were utilized. Attempts were also made to use the earth's magnetic field as the static field. Large magnetizing coils were energized and rapidly switched off allowing the magnetization to precess in Earth's field [68]. These initial attempts were not very successful due to poor sensitivity of NMR signals in the Earth's field [67, 69].

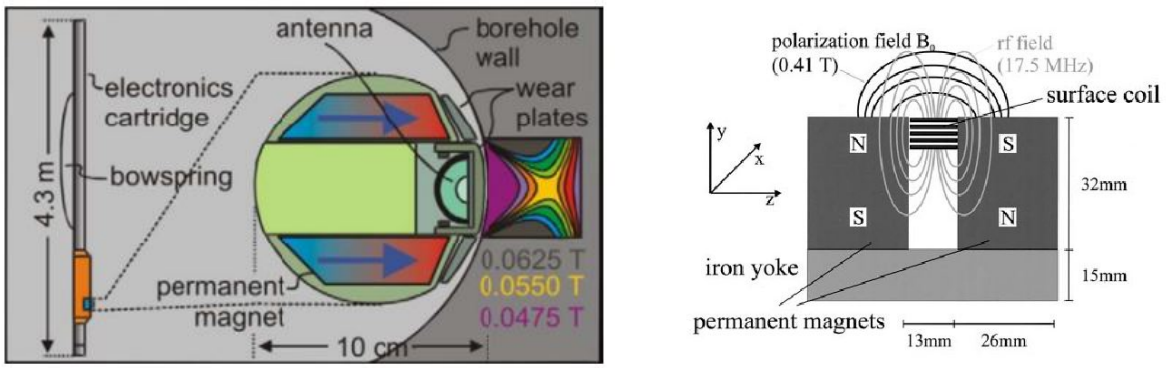

(a) Industrial device

(b) Lab device

Figure 1.2: (a) Schlumberger's [64] initial design for NMR measurements in oil wells, (b) First portable inhomogeneous field based system [61]

Several antenna designs were also explored. Schlumberger was one of the pioneers in utilizing ferrite loaded antennas to overcome signal-to-noise ratio limitations (Fig. 1.2a). However even they faced challenges of magnetoacoustic ringing and used a combination of techniques to overcome ringing [70] due to the ferrites.

A portable magnet and coil detection system are integral parts of the unilateral system. The major findings from the oil industries explorations were the physical requirements for unilateral NMR measurements. The requirements were [64]:

1. A region of relatively uniform static magnetic field
2. A radio frequency field perpendicular to the static field
3. Resonance condition i.e. ratio of oscillating field frequency to the static field strength be the gyromagnetic ratio
4. Short measurement wait time

These requirements were further reinforced by NMR measurements in homongeneous magnetic fields by the medical community. In fact the unilateral NMR sensor designs at that time were focused on developing devices capable of generating localized regions of homongeneous magnetic fields or "sweet spots" [71, 72]. Homogeneous fields allowed comparatively improved signal to noise ratio (SNR), larger sensitive volumes and long lasting NMR signals and were preferred. However, these initial techniques were best only for analyzing rocks that were a few centimeters away from the probes.

1.2.4 Other efforts

Beyond the oil industry, open geometry sensors also started becoming popular in nondestructive testing of materials [73], moisture detection [74, 75], medical diagnostics [76] and so on [57]. With use of permanent magnets and surface coils, different measurement techniques emerged. The "stray-field imaging" or STRAFI technique [77] was one such technique wherein the test samples were moved through the sensitive imaging slice created by strong static field variations. While the

technique is simple, use of superconducting magnets for generation of field gradients and time consuming experiments made this technique less popular [78] among researchers.

Other methods incorporated creation of magnet assemblies that could provide homogeneous magnetic field over larger volumes. Designs based on Halbach magnet arrays [79], radially magnetized discs [80], multiple concentric ring structures [81], HALO (high access low oersted) system [82] etc.[83], were implemented and each presented different challenges such as low SNR, limitations on detection volume and limited control of field variations.

Several designs which utilized the inhomogeneous nature of magnetic fields also emerged. The first fully portable device, NMR MOUSE (Mobile Universal Surface Explorer) was one of the first mobile unilateral NMR systems capable of measuring signals from the side of an object [61].

The first mobile lab device as seen in Fig. 1.2b comprised of a horse-shoe shaped magnet that generated an inhomogeneous static magnetic field B_0 and an RF surface coil that is used to generate the RF field B_1. Use of surface coils restricted the detection area to regions close to the surface of the object. The RF coil used was a 4-layer solenoid with 8 turns per layer. The inductance was of the order of 3 μH. From this design, a deadtime of about 10 μs was obtained. Since the fields are inhomogeneous, single and multiecho techniques such as Hahn echo, Carr-Purcell-Meiboom-Gill pulses and Ostroff-Waugh 4 were used to measure the NMR signal decay time [57]. The technique developed in this work was used for detection of different polymers with a penetration depth of 5 mm.

Another design by [84] was utilizing a tailored permanent magnet array which produced flat sensitive volumes up to 40 mm from the mobile inspection head. Automated slice selection was conducted by using a set of switched capacitors in the tuning and receiver circuits. A single channel spectrometer was used to drive the the multi-slice acquisition. The RF coil and magnet array geometries were tailored to house field gradient sets to further improve the image rendering capabilities. This work identified that the main challenge for image rendering using a single-sided sensor is to achieve spatial resolution away from the probe head. Many other developments such

as the NMR MOLE (Mobile Lateral Explorer) [85] and application specific devices using different permanent magnetic geometries and arrangements emerged in this duration.

1.2.5 Non-uniform field NMR

As discussed, controlled non-uniformity in static fields is advantageous in medical imaging and even stray-field imaging. Based on Table. 1.1, non-uniform NMR can occur in low field conditions and can be used for portable NMR solutions.

Table 1.1: Comparison of parameters for uniform and non-uniform field NMR [86]

Parameter	**Uniform NMR**	**Non-uniform NMR**
B_0	1 - 5 T (some upto 35 T)	Upto 2 T
B_1	Frequency dependent	0.0001 - 0.01 T
B_0 source	Superconducting magnets	Permanent magnets
Operational frequency	B_0 dependent (Upto 340 MHz)	Upto 30 MHz
Investigation depth	Frequency dependent (Upto 100 cm)	Low (0 - 30 mm)
Spatial Resolution	nm - um	Low (um - mm)
Signal to noise ratio	High	Low

Correspondingly several questions arise. While the first and most challenging question is still on how one may achieve improvements in SNR and spatial resolution in non-uniform fields the second question may be the feasibility of obtaining reliable signals in low external magnetic fields (approximately 0.01 T). These questions demand a better understanding of the noise or background signal due to the presence of the magnet, surrounding environment, nature of anomalies to be detected etc. and an understanding of the measurement constraints on SNR, spatial resolution etc. These will be addressed in some detail in Chapter 3.

1.3 Towards a portable non-uniform NMR system

Several ongoing efforts towards creating portable NMR systems exist. Many of the existing systems are designed to be application specific. Thereafter, there is a generic need for improved portable NMR systems that can operate well in field non-uniformity. The system proposed in this

work incorporates the aspect of portability and brings forward possible approaches of operations in non-uniform fields. The design considerations for the permanent magnet assembly, pulsed field generator and measurement assembly will be described in this document. It is expected that through this work the research community will understand the challenges and possibilities in low non-uniform field NMR measurements.

1.4 Conclusions

The primary goal of this work was to investigate the possibility of obtaining NMR signals in non-uniform magnetic fields. Two different application areas were considered. Initially, operations of unilateral NMR sensors used in oil industries were investigated to obtain a perspective on potential challenges for non-uniform field measurements. The design, operation and measurements from an existing unilateral NMR sensor were analyzed. More specifically, the effect of different magnetic materials used within the sensors were tested under application of a DC magnetic field bias alongside a RF magnetic field. The unilateral sensor measurements highlighted the effects of non-uniform magnetic fields on the test samples and led us to further investigate the relation between non-uniform fields and NMR detection. The design of a ring magnet was evaluated for portable unilateral NMR purposes. A pulsed magnetic field generator was designed and a commercial assembly of the magnet and field generator were tested together to measure NMR signals in non-uniform fields.

1.5 Contributions

Through the course of this research work several aspects of unilateral NMR systems have been examined, designed and experimented upon. Of these, the primary contributions from this work include:

1. Methods to pre-estimate static magnetic field variations in free space for varied permanent magnet geometries

2. Design of pulsed field generation systems to generate low pulsed magnetic fields (upto 0.01 T)

3. Design of appropriate transmit and receive geometries (surface coils)

4. Systematic integration of different stages and sufficient testing and experimentation to validate proof of concept prototype

5. Documentation of techniques, methods and considerations for future improved portable unilateral NMR systems

CHAPTER 2. OVERVIEW OF NUCLEAR MAGNETIC RESONANCE

The central theme of this work is acquisition of nuclear magnetic resonance signals from various samples placed in non-uniform magnetic fields. This chapter is a review of the necessary background and definitions related to nuclear magnetic resonance (NMR), and associated measurement parameters.

2.1 Basic principles of NMR

NMR is a phenomenon wherein atomic nuclei (protons and neutrons) respond to externally applied magnetic fields. Atomic nuclei, with odd atomic numbers possess an inherent magnetic moment (nuclear spin) that creates an intrinsic magnetic field. In the absence of external fields, the nuclear spins are randomly oriented. When atomic nuclei experience an external magnetic field, they reorient in the direction of the externally applied field. The nuclei align either to an energetically favorable parallel or anti-parallel direction [18]. Additionally, the external static flux density, B_0, exerts a torque on the nuclei causing them to precess about the external field axis. The precession occurs at a frequency, related to the applied field, known as the Larmor precession frequency, ω_0, and is given by [18]:

$$\omega_0 = \gamma B_0 \tag{2.1}$$

Application of radio frequency (RF) pulses to the precessing nuclei causes energy transfer to occur between the different energy levels occupied by the spins. Nuclei absorb RF energy that corresponds precisely to the energy difference between available energy levels and release RF energy at the same frequency when the RF pulse is removed. Electromagnetic radiations are emitted during this process. The entire process of energy absorption and relaxation (energy release) occurs when the RF energy corresponds to the energy difference between the spin states. This is termed resonance, and since it occurs between magnetic nuclei, the phenomenon is known as nuclear magnetic resonance

(NMR). Electrons also possess spin magnetic moments and will also precess in externally applied magnetic fields. However, the electrons precession frequency is much higher than that of protons (GHz's in contrast to MHz's) and thus require a larger static magnetic field and a high frequency pulsed field. For example, in a static magnetic field of 1 T, the Larmor precession frequency for an electron is $1.76 \times 10^{11} s^{-1}$ and for a proton is $2.67 \times 10^{8} s^{-1}$ [87]. Thus, many NMR-based procedures such as oil-well logging or magnetic resonance imaging (MRI) are based on proton (or hydrogen) NMR instead of electrons like in electron spin resonance (ESR).

NMR can occur when any nucleus which has an odd number of protons or neutrons or both [88] undergoes spin transitions from one energy level to another in externally applied magnetic fields. NMR occurs only because the nuclei have a non-zero spin. Such nuclei possess a magnetic moment, μ, which is affected by external magnetic fields. Mathematically, the magnetic moment is expressed as,

$$\mu = \gamma J \tag{2.2}$$

Here, γ is the gyromagnetic ratio, a proportionality coefficient between the magnetic moment and the angular momentum specific to each nucleus and J is the angular momentum. When an external static magnetic field B_0 is applied to the nucleus, the magnetic moments tend to align either with (lower energy orientation) or against (higher energy orientation) the external field as shown in Fig. 2.1.

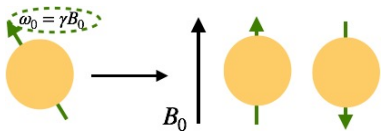

Figure 2.1: Possible orientations of nuclear magnetic moments (parallel/antiparallel to external field) (adapted from [89])

In general, most of the nuclei tend to align in the lower energy orientation while some will align in the higher energy orientation (Fig. 2.2). At the same time, the nuclei are constantly precessing along the static magnetic field direction. Then, when an RF pulse at the nuclear precession frequency is

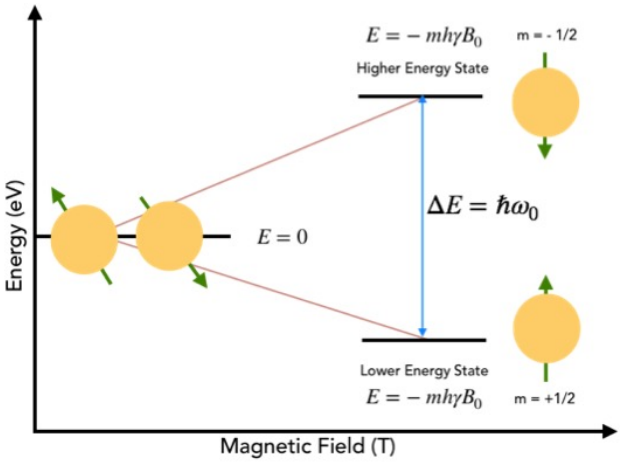

Figure 2.2: Splitting of degenerate nuclear energy levels under an applied magnetic field (adapted from [89])

applied, a spin flip or transition occurs between the two energy states. An exact quantum of energy is required for this transition, as seen in Fig.2.3. For a spin 1/2 nucleus, there are only two energy levels, the lower energy level (i.e. occupied by spins aligned with B_0) and the higher energy level (i.e. occupied by spins aligned against B_0). Energy in each level is described as

$$E = -m\hbar\gamma B_0 \tag{2.3}$$

Here, m is the magnetic quantum number, $\hbar = \frac{h}{2\pi}$ is the reduced Planck's constant and the energy difference between energy levels for a spin 1/2 system is

$$\Delta E = 2m\hbar\gamma B_0 \tag{2.4}$$

Since spin transitions occur for a collection of nuclei, on a macroscopic scale, on application of RF pulses, the net magnetization is affected. The macroscopic magnetization, M_0 is defined as the net magnetic moment per unit volume. For N nuclei per unit volume, it is defined as [45],

$$M_0 = N\frac{\gamma^2 h^2 I(I+1)}{3(4\pi^2)kT}B_0 \tag{2.5}$$

where k is Boltzmann's constant, T is the absolute temperature in Kelvin, h is Planck's constant and I is the spin quantum number of the nucleus. From equation 2.5 it is observed that the

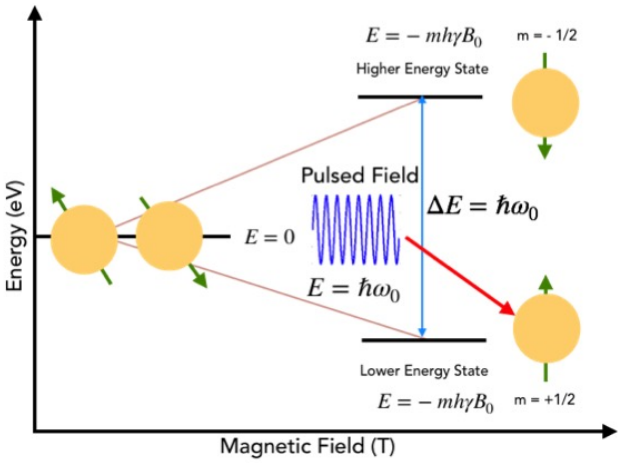

Figure 2.3: Absorption of radio frequency radiation to promote a transition between available nuclear energy levels (adapted from [89])

magnetization directly depends on the static field strength and the number of nuclei. This implies that a higher static field and number of nuclei are desirable in most NMR measurements.

For every NMR experiment, a transition or a spin flip between the two/variable energy states is initiated via application of a pulsed field. The energy required for such a transition is expressed as

$$E = h\nu \text{ where } \nu = \frac{\gamma B_o}{2\pi} \tag{2.6}$$

As shown in equation 2.3 the extent to which one energy state is favored over the other is determined by the external magnetic field strength B_0 and the strength of the small nuclear magnet (i.e. proportional to the gyromagnetic ratio). RF pulses are applied for particular pulse widths in order to initiate spin transitions and alter population ratios. The application of a pulsed field causes the protons to precess in phase. Additionally, the pulses reorient the net magnetization vector by specific angles. If the pulsed field B_1 is applied for a time duration τ, the rotation angle is

$$\theta = 2\pi\gamma\tau B_1 \tag{2.7}$$

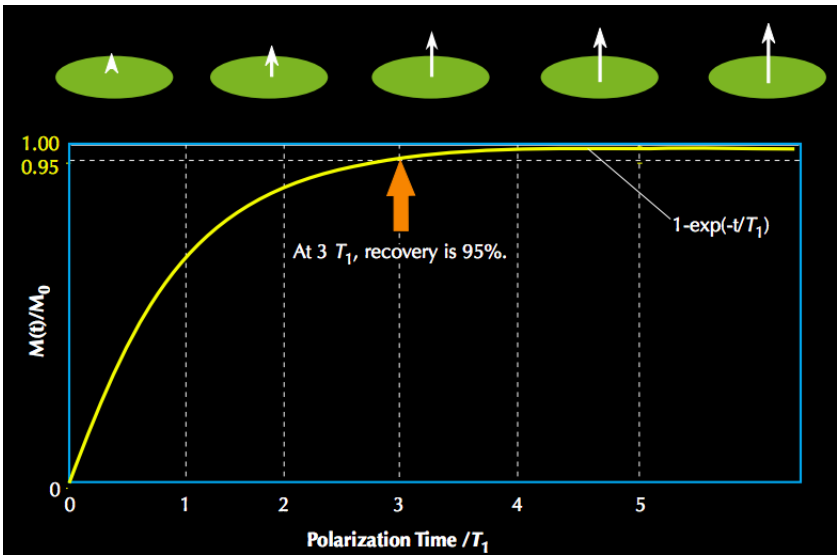

Figure 2.4: Longitudinal magnetization recovery and T_1 relaxation process for a proton population ([88])

Generally, the RF pulses reorient the net magnetization by an angle of 90^o ($\pi/2$ pulse). Transverse magnetization components (x-y plane) offer greater measurement sensitivity to field variations.

Once the RF excitation pulse is removed, the nuclei begin to return to their thermodynamically stable states along the DC field direction. The protons start precessing out of phase and the net magnetization of the system decreases. The energy absorbed during the transition from the lower energy state to the higher energy state is released, Fig. 2.6, and the decay process, termed as "relaxation" occurs. Since two types of magnetic fields exist, the static field and the RF pulsed field, there are two types of relaxation processes. Once the RF pulsed field is removed, the time associated with the recovery of the magnetization along the longitudinal direction is termed as T_1 or spin-lattice relaxation, Fig. 2.4.

In this process, the energy of the spin system is transferred to neighboring atoms (the lattice). The recovery of the longitudinal magnetization, M_z, to its equilibrium value M_0 is described via equation 2.8 and the net longitudinal magnetization is described in equation 2.9. Additionally, the decay time associated with the recovery in the transverse plane, M_{xy}, as in Fig. 2.5, is known as spin-spin or T_2 relaxation and is defined as the time for the magnetic resonance signal to decay

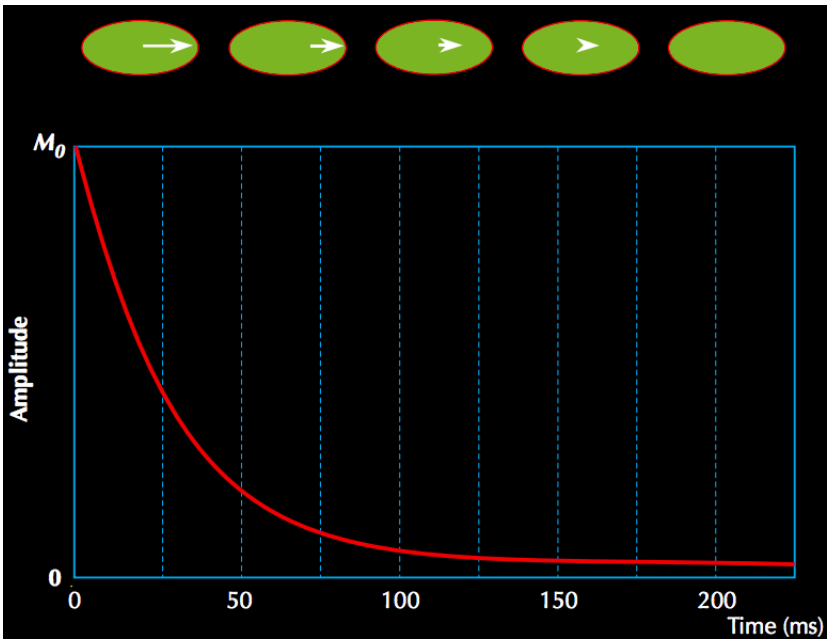

Figure 2.5: Transverse magnetization recovery and T_2 relaxation process for a proton population ([88])

to 37 % of its initial value once the magnetization has tipped into the transverse plane (equations 2.10 and 2.11).

$$\frac{dM_z}{dt} = \frac{M_0 - M_z}{T_1} \tag{2.8}$$

$$M_z = M_0(1 - e^{-\frac{t}{T_1}}) \tag{2.9}$$

$$\frac{dM_{xy}}{dt} = \frac{-M_{xy}}{T_2} \tag{2.10}$$

$$M_{xy} = M_{xy0}e^{-\frac{t}{T_2}} \tag{2.11}$$

In essence, an NMR signal is a record of the energy absorption and relaxation processes when the applied radio frequency (RF) pulse is removed. It is generally a time varying exponential signal which decays rapidly (tens of microseconds). In practice, a huge number of nuclei (approaching Avogadro's number) are placed in the magnetic field. The distribution of nuclei in the different energy states under conditions in which the nuclear spin system is unperturbed by application of

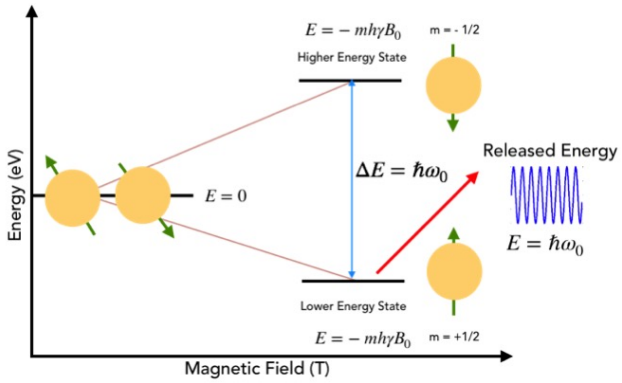

Figure 2.6: Relaxation process (adapted from[89]) occurs on application of appropriate RF pulses

any RF energy is given by the Boltzmann equation:

$$\frac{N_{upper}}{N_{lower}} = e^{\frac{-\triangle E}{kT}} = e^{\frac{-h\nu}{kT}} \tag{2.12}$$

Here, N_{upper} and N_{lower} represent the number of nuclei in upper and lower energy states, respectively, k is the Boltzmann constant and T is the absolute temperature in Kelvin.

The relaxation process is generally recorded using pick-up coils placed along and transverse to the direction of the static field. The detected signal is known as free induction decay (FID), Fig. 2.7, and the signal decay rates relate to the relaxation processes. To detect the energy transitions, the net system magnetization is rotated by 90^o transverse to the static field by applying an excitation pulse for a specific time duration as estimated by equation 2.8.

The 90^o pulse causes rotation of the magnetization by 90^o and an equalization of population in the two energy states. Often a 180^o pulse is applied after the 90^o pulse resulting in an inversion of population between the two energy states. In this case the higher energy state has a larger number of nuclear spins (Fig. 2.8). Moreover, the 180^o pulse can re-phase the protons i.e faster protons would move slower and vice versa. This implies that the signal decay and recovery are both observed at the receiver and a signal known as the spin echo is observed (Fig. 2.7).

Relaxation processes that neither emit nor absorb radiation permit the nuclear spin system to redistribute the population of nuclear spins. Some of these processes lead to nonequilibrium spin distribution exponentially approaching the equilibrium distribution over time. When RF energy

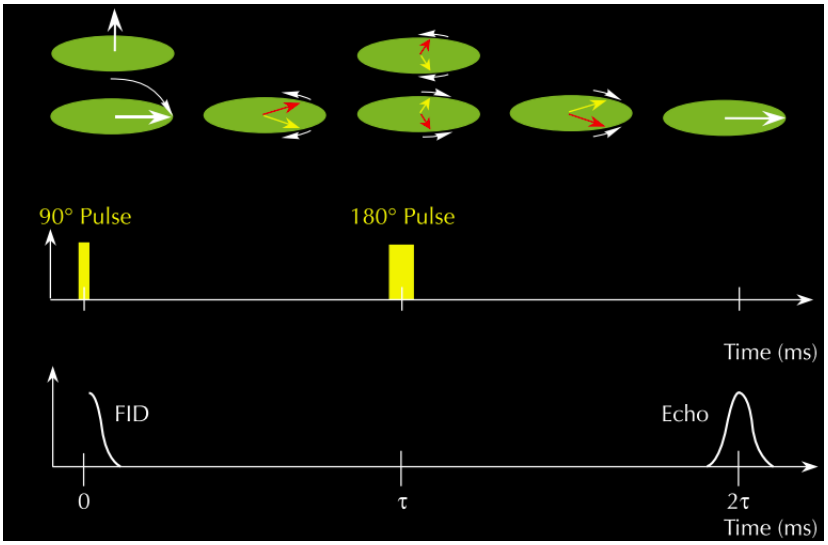

Figure 2.7: Free induction decay and spin echo after application of a 90^o and 180^o pulse respectively ([88])

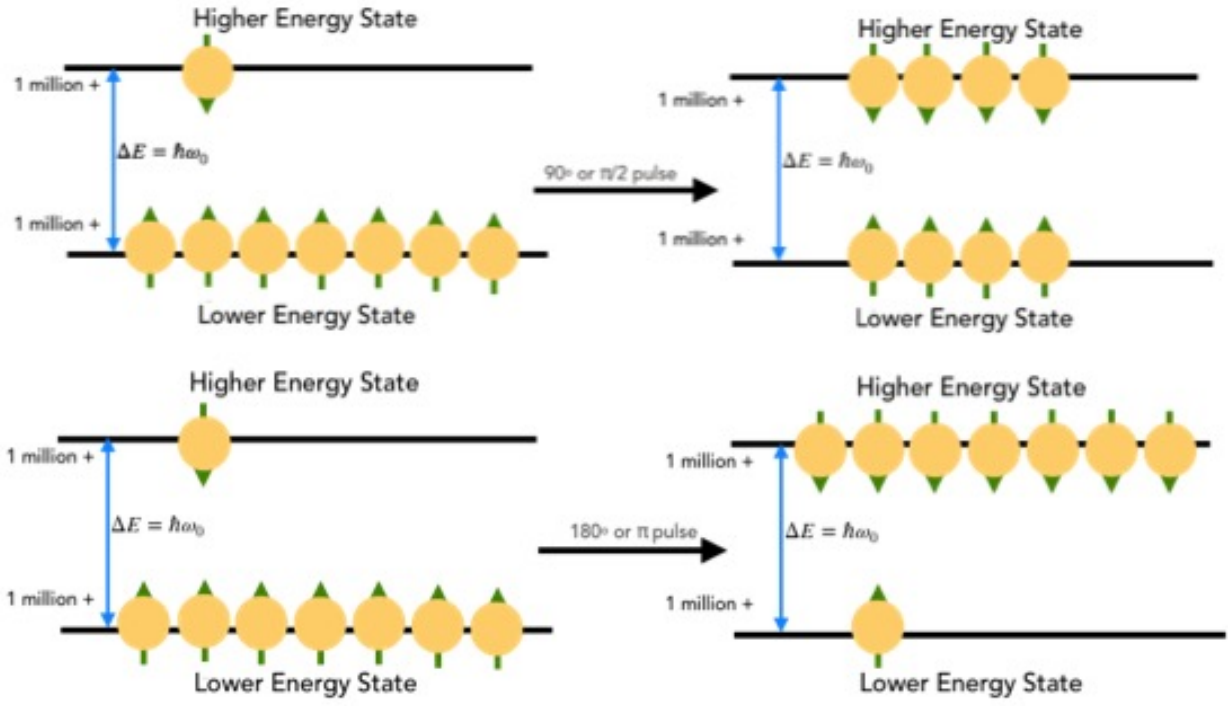

Figure 2.8: Effect of 90^o and 180^o RF pulses on nuclear spin populations (adapted from [90])

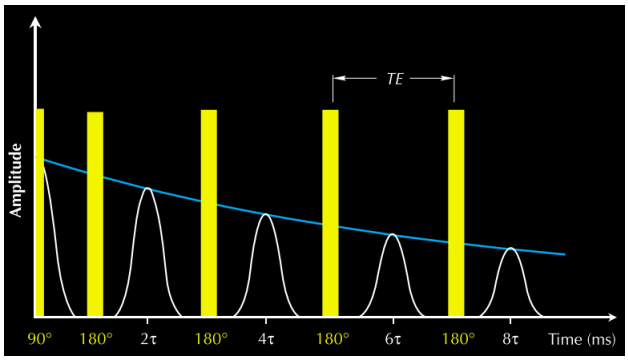

Figure 2.9: Typical behavior on application of a CPMG pulse sequence ([88])

is applied to the nuclear spin system at the precession frequency, the probability of an upward transition is equal to that of a downward transition. Since there is a greater number of nuclei in the lower state there will be more transitions from the lower state to the upper state than vice versa resulting in a nonequilibrium distribution of nuclear spins. When the difference between the number of protons in each state is equalized, the NMR signal will disappear and the signal is termed to be saturated.

2.2 Relation to this work

As expressed in equation 2.1, in a given test sample, all the magnetic moments precess about the static field direction at the Larmor precession frequency.

$$\omega_0 = -\gamma B_0 \tag{2.13}$$

However, in a non-uniform magnetic field, the static field spatially varies and in such cases there is a variation in the precession frequency across the length of the object and in space. The variations in precession frequency affect the spatial precession rates of magnetic moments. Therefore, a possible representation of equation 2.1 after incorporating spatial variations can be

$$\omega_{actual} = -\gamma B_{actual} \tag{2.14}$$

Using equation 2.14 a method of accurately identifying regions producing NMR signals may be identified. Detection of NMR signals despite spatial variations and non-uniform fields is performed using various pulse sequencing techniques. One of the popular sequences designed by Carr-Purcell-Meiboom-Gill (CPMG) [91] is used to measure a modified version of the transverse spin-spin relaxation time T_2* which includes the effect of field non-uniformities. In this pulse sequence, multiple 180^o pulses are repeatedly applied to rephase the protons and obtain several spin echoes. The magnetic field non-uniformity has an irreversible effect on the molecular interactions and diffusion. Therefore, the amplitude of the spin-echoes decreases with time. An exponential fit through the peak's of the spin echoes is a measure of the transverse decay time, T_2. Often the relaxation time reduces to a smaller value T_2*. Empirically, the measured time T_2* is given by

$$\frac{1}{T_2*} = \frac{1}{T_2} + \frac{1}{T_2^i} \tag{2.15}$$

where $1/T_2^i = \gamma \Delta B$ is the relaxation rate due to non-uniformity measured across a specific region.

Thus, in this work, in order to incorporate the non-uniform behavior of magnetic fields, CPMG pulse sequences are employed for a few measurements with the designed sensor. The measurements of ferromagnetic materials placed in such non-uniform magnetic fields are also evaluated via use of other simpler pulse sequences. Additionally, detailed analysis on the static field variations will lead to identification of new static field control mechanisms for improving spatial resolution in non-uniform fields.

CHAPTER 3. STATIC FIELDS DUE TO PERMANENT MAGNETS

From prior discussions it is understood that nuclear magnetic resonance (NMR) is a well-established measurement technique commonly used for the detection and estimation of different nuclear species. As we also saw in the previous chapters, uniform static magnetic fields are necessary in most NMR/MRI experiments for creating the DC bias conditions that are eventually integral for detecting the presence of nuclear species [92]. Permanent magnet based NMR systems bring the capability of portable NMR detections at the expense of low static field strengths (0.01 - 0.1 T), low signal-noise ratios (SNR) and limited regions of detection [59, 60, 61]. Despite these drawbacks, several low-field, stray field and non-uniform field NMR measurement techniques have been designed and implemented by other researchers.

In this chapter, finite element simulation models have been used to estimate external magnetic field distributions for different permanent magnet geometries. Simulation results show that concentric ring magnet geometries possess regions of stable and uniform magnetic fields even in the magnet's exterior. Such stable field regions are further studied with the intention of obtaining flexible control and movement of localized uniform field locations. Using the simulated static field distribution, expected NMR signal from samples placed in such regions is calculated for different ring magnet geometries. The findings from this chapter inform the choice of static field generation methods and specifically design of permanent magnet geometries for obtaining regions of uniform static field in the magnet's exterior.

In summary, we seek to understand the magnetic field variations of a permanent ring magnet for portable NMR applications. The magnetic field exterior to the magnet is evaluated to determine regions of localized field uniformity. Also, it is expected that with an improved understanding of spatial magnetic field variations, localized NMR detection may be improved. In turn, these findings would enhance capabilities of future portable medical diagnostic NMR systems. The main goal of

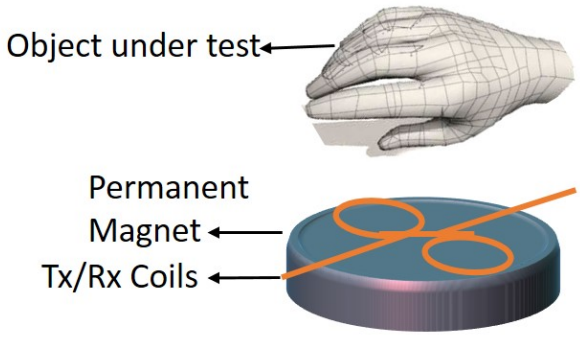

Figure 3.1: 3D view of proposed sensor. A transmit/receive coil is placed on top of the permanent magnet assembly.

this work is to identify parameters which can be used to control occurrence, location and size of localized stable field regions or saddle points where optimal field uniformity gets achieved.

3.1 Proposed system design

A representation of the proposed portable NMR sensor inclusive of the magnet, measurement coil and object under test are seen in Fig. 3.1. In this design, the magnets will be magnetized along the axial direction, a set of surface coils will be placed on top of the magnet to produce a pulsed magnetic field B_1 perpendicular to the applied static magnetic field and the sample under test (here, a human hand) is placed at reasonable distances from the sensor surface.

Due to the use of permanent magnets, the generated static field is spatially non-uniform and low. Nonetheless, unilateral systems are capable of generating localized regions of homogeneous magnetic fields or "sweet spots" [23, 67, 93]. These small homogeneous regions allow for improved signal-to-noise ratio (SNR), larger sensitive volumes and NMR signals. It is possible that detection in such localized regions may be valuable for medical applications making MRI portable and accessible to all. Moreover, such regions of localized field homogeneity could allow for precise detection of small tumors and their locations.

3.2 NMR voltage in non-uniform fields

As discussed above, magnetic field variability leads to difficulties in spatially estimating NMR signals and causes low SNR. Prior work [67, 93, 94] showed ways to estimate the NMR voltage induced in a receiving coil under conditions of variable fields. In non-uniform magnetic fields, the NMR voltage is described as per equation 3.1 [93].

$$V_{NMR} = \frac{2\chi}{\mu_o} \int dr \phi(r) B_0^2(r) \frac{\omega_1(r)}{I} F(\delta\omega_o(r)) m_{x,y}(r,t) \tag{3.1}$$

Here, χ is the nuclear susceptibility, B_0 is the static magnetic field produced due to the permanent magnets, $m_{x,y}(r,t)$ is the local transverse magnetization at point r and time t, $F(\delta\omega_o(r))$ is the frequency response of the detection system, I is the current in the coil needed to give rise to $\omega_1(r)$ and $\phi(r)$ denotes the local density of spins.

From equation 3.1, it is apparent that besides the receiver characteristics, the voltage signal is dominated by the strength of the static field and the magnetization of the magnetic moments in the x-y plane. For the consideration of this discussion, the receiver characteristics will be ignored. Then, the induced NMR voltage signal will be proportional to various parameters described as

$$V_{NMR} \propto \int dr B_0^2(r) \frac{\omega_1(r)}{I} m_{x,y}(r,t) \tag{3.2}$$

Additionally, as per equation 1.1, it is well known that the SNR of NMR measurements is proportional to the strength and homogeneity of the static magnetic field [58] and inversely related to the gradients in the static field. This implies that to achieve higher SNR the competing requirements of high static magnetic fields and high field gradients need to be balanced. In fact, minimal variations in static field strength would lead to higher SNR. Thereafter, in this work, we propose to obtain higher SNR from regions of localized static fields or identifying regions that have high static fields and lower field gradients. Such regions will be found by controlled positioning and orientations of the permanent magnets.

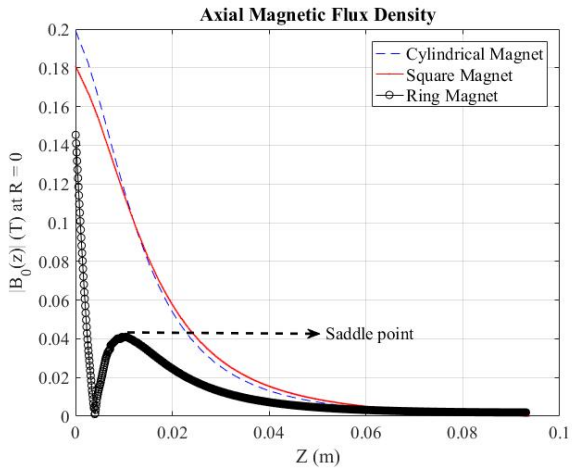

Figure 3.2: Representation of magnetic flux density (B) from various permanent magnets

3.3 Magnetic fields of permanent magnet geometries

The magnetic fields due to permanent magnets are low and have high magnetic field variability in the magnet's exterior. As seen in Fig. 3.2, for most magnet geometries, the magnetic flux density decays with increasing distance from the magnet's surface. This means that if NMR signals were measured using such magnets, users would need to place the samples near to the magnet surface to benefit from the high static field. However, from Fig. 3.2 it is observed that for a ring magnet geometry, there is a small region away from the magnet surface where the field is uniform enough before its decay.

In fact, several NMR magnet designs show the presence of localized regions of uniform magnetic field [61, 60, 95]. Such regions, often termed as "saddle points" (or sweet spots), occur when the magnetic fields due to the magnet poles superimpose constructively. Mathematically, a saddle point occurs at the location where the partial derivatives, $\frac{\partial B}{\partial x}$, $\frac{\partial B}{\partial y}$ and $\frac{\partial B}{\partial z}$, are zero but the point is neither a maxima or a minima. The presence of localized field uniformity within non-uniform fields implies that saddle points can be used for detecting NMR signals from sample's placed in a magnet's exterior.

3.4 Simulations of fields produced by permanent magnets

Finite element simulations for permanent magnet geometries can assist in understanding the effects of the magnetic field produced by permanent magnets in space and in objects with varying states of magnetization such as paramagnets, diamagnets or ferromagnets. Permanent magnet materials retain magnetization and correspondingly create a persistent magnetic field. Due to the material's state of magnetization, it is well known that no external current sources are required to create a stable static field. This is advantageous in creating portable devices that require low magnetic fields. Since permanent magnet's act as dipoles, the magnetic field lines form closed loops between the north and south poles, thereafter ensuring that the magnetic flux density, B, has zero divergence. Thus, Gauss's law holds true and the net divergence at a point exterior to the magnet's surface can be written as follows,

$$\nabla.(B_{0x}\hat{x} + B_{0y}\hat{y} + B_{0z}\hat{z}) = 0 \tag{3.3}$$

and

$$\frac{\partial B_{0x}}{\partial x} + \frac{\partial B_{0y}}{\partial y} + \frac{\partial B_{0z}}{\partial z} = 0 \tag{3.4}$$

Generally, a vector field which doesn't possess a divergence is considered to have rotational behavior. However, due to the absence of current sources in the exterior of the magnet, from Ampere's law, one may state that,

$$\nabla \times B = 0 \tag{3.5}$$

Therefore, an approximation for the static field components can be,

$$\frac{\partial B_{0z}}{\partial y} = \frac{\partial B_{0y}}{\partial z}, \frac{\partial B_{0z}}{\partial x} = \frac{\partial B_{0x}}{\partial z}, \frac{\partial B_{0y}}{\partial x} = \frac{\partial B_{0x}}{\partial y} \tag{3.6}$$

For a spatially varying magnetic field, the spatial dependence of the magnetic field is expressed as

$$B_{0z}(x) = B(x = 0) + \frac{\partial B_{0z}}{\partial x} + \frac{1\partial^2 B_{0z}}{2\partial x^2} + ... \tag{3.7}$$

Ignoring higher order terms, the spatially dependent magnetic field may be approximated as the field at the magnet's surface and the variations often described as a field gradient,

$$G_x = \frac{\partial B_{0z}}{\partial x} \tag{3.8}$$

Here the spatial dependence is considered to be limited to only one direction. Correspondingly, the Larmor precession frequency as described in equation 2.1, can be modified to

$$\omega_0 = \gamma(B_{0z} + G) \tag{3.9}$$

Here G represent the field gradient of B_{0z} along all possible orientations. One must note that these approximations wouldn't hold true within or on the magnet's surface. They are valid for all points exterior to the magnet basically in free space.

3.5 Magnetic field simulations for planar magnets

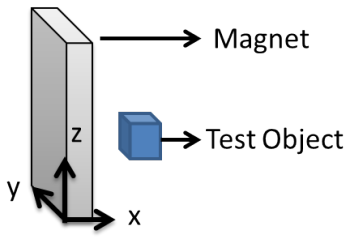

Figure 3.3: Schematic of the magnet and object

Initial simulations were conducted with a NdFeB permanent magnet (0.05 m x 0.05 m x 0.01 m) with a cuboidal object placed above the magnet as seen in Fig. 3.3. The magnet was assigned a remanent magnetic flux density of 1.32 T (as per manufacturer specifications) and it was assigned a magnetization along the z direction. The position of the cubical object was varied from 0.01 m to 0.076 m away from the magnet. Originally, the test object was assigned a permeability of free space and then assigned a relative permeability of 4000. From Fig. 3.4 it is observed that the magnetic field undergoes an expected field accumulation in the presence of the magnetic object. As expected, the magnetic field decays with increase in distance from the magnet surface.

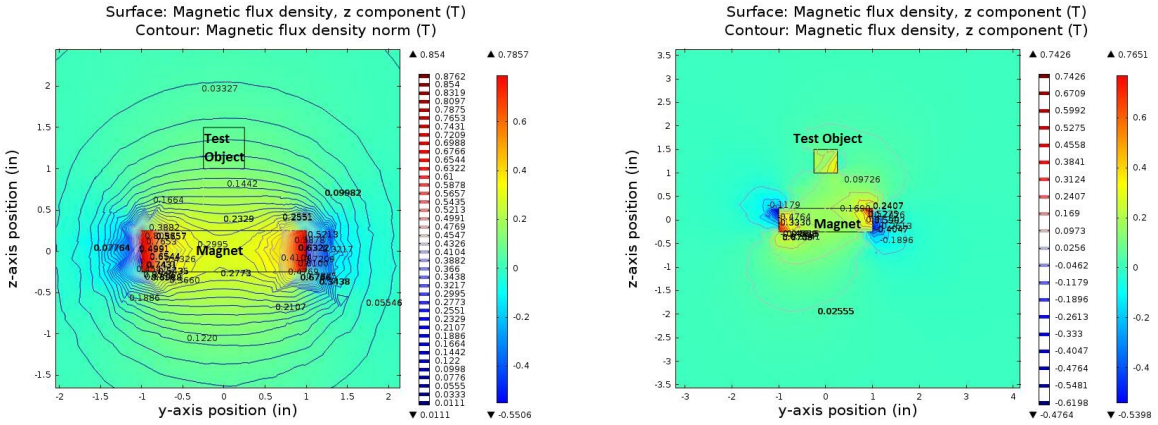

(a) Permeability = 1

(b) Permeability = 4000

Figure 3.4: Cross-sectional view of magnetic flux density through (a) Non-permeable object and (b) Permeable object

Thereafter, to perform magnetic resonance experiments with rectangular magnets, the test samples need to be placed as close to the magnet as possible. The effect of using magnetized samples in magnetic resonance experiments will become apparent in Chapter 7. Protons in water samples will resemble the object with the permeability of free space.

Finite element simulations were also performed to estimate the NMR signal which may be obtained on using different magnet geometries with comparable static field. It was assumed that the paramagnetic species, ^{1}H, was the test sample. Simulations were performed using planar geometries such as rectangular magnets (both NdFeB and SmCo), cylindrical magnets and hollow cylindrical magnets (ring magnets). As in Fig. 3.4a, Fig. 3.5b and Fig. 3.6b, it is observed that the magnetic field decays uniformly with increasing distances from the magnet surface for the planar and cylindrical magnets respectively. This implies that for improved SNR and sensitivity samples should be placed near the magnet surface. From this perspective, ring magnets are advantageous due to the presence of stable field regions in the magnet's exterior. Table. 3.1 shows that the estimated signal level is significantly different for ring magnets due to the localized uniform magnetic field

region. Therefore, in the following section, a detailed analysis of the the ring magnet geometry is performed and discussed.

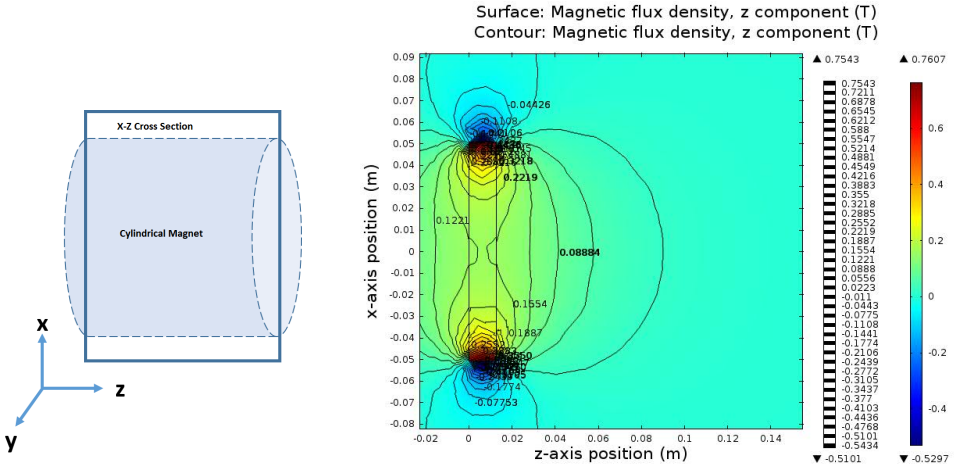

(a) Schematic (b) Magnetic flux density

Figure 3.5: Magnetic flux density for a cylindrical magnet

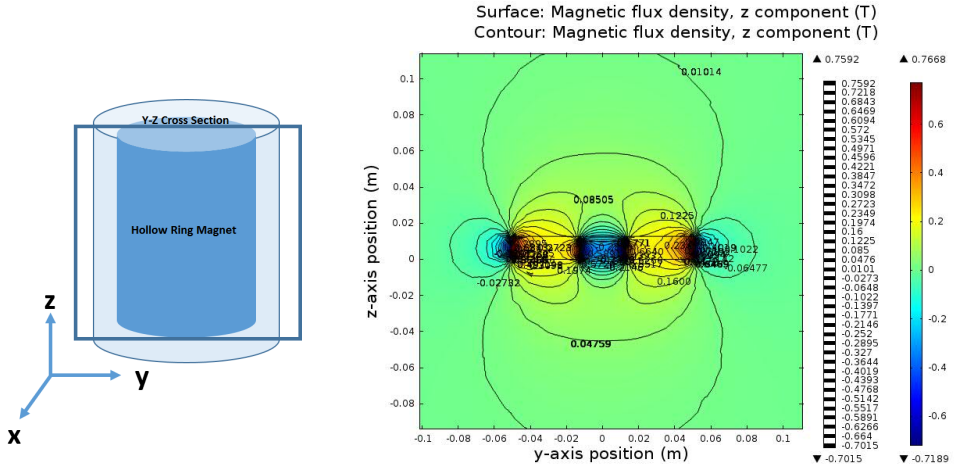

(a) Schematic (b) Magnetic flux density

Figure 3.6: Magnetic flux density for hollow ring magnets

Table 3.1: Comparison of estimated signals from different magnet geometries

Geomery	Estimated Signal (nV)	B_0 (T)	Frequency (MHz)
Rectangular	0	0.005	0.2
Cylinder	0	0.14	6.01
Ring	9	0.14	5.94

3.6 Ring magnet considerations

As shown in the prior section, the dependence of NMR voltage on the static field introduced by ring magnets, and as demonstrated by [95, 96], ring magnets properties have various advantages for sensor design and need further examination. Finite element simulations for obtaining the maximum uniform field in the magnet's exterior and to obtain static field distribution maps were performed in COMSOL Multiphysics software. From the static field maps, the saddle point locations and induced NMR signal were estimated for different magnet parameters.

Initial simulations were performed to optimize the design of the magnet geometry. A magnet with a 0.025 m diameter and a height of 0.025 m was used. A remanent magnetic flux density of 1.32 T was used to define an axial magnetization (along z) for the NdFeB ring magnet. The magnet's inner radius (IR), outer radius (OR) and height (H) were varied to obtain the highest static flux density at a reasonable distance from the magnet surface.

First, as seen in Fig. 3.7a, the axial location of the saddle point is dependent on the magnet's inner radius. For a fixed outer diameter of 0.025 m and a height of 0.025 m, it is observed that the saddle point occurs above the magnet at distances equal to the inner radius. Additionally, for smaller inner radii, the overall magnetic flux density increases.

From Fig. 3.7b, it can also be seen that a larger outer radius would contribute to a higher magnetic flux density. Additionally, the axial location of the saddle point shifts with changes in the outer radius.

Lastly, simulations for height variations as a function of distance from the magnet's center, Fig. 3.7c show that after attaining a particular height, the improvement in the magnetic flux

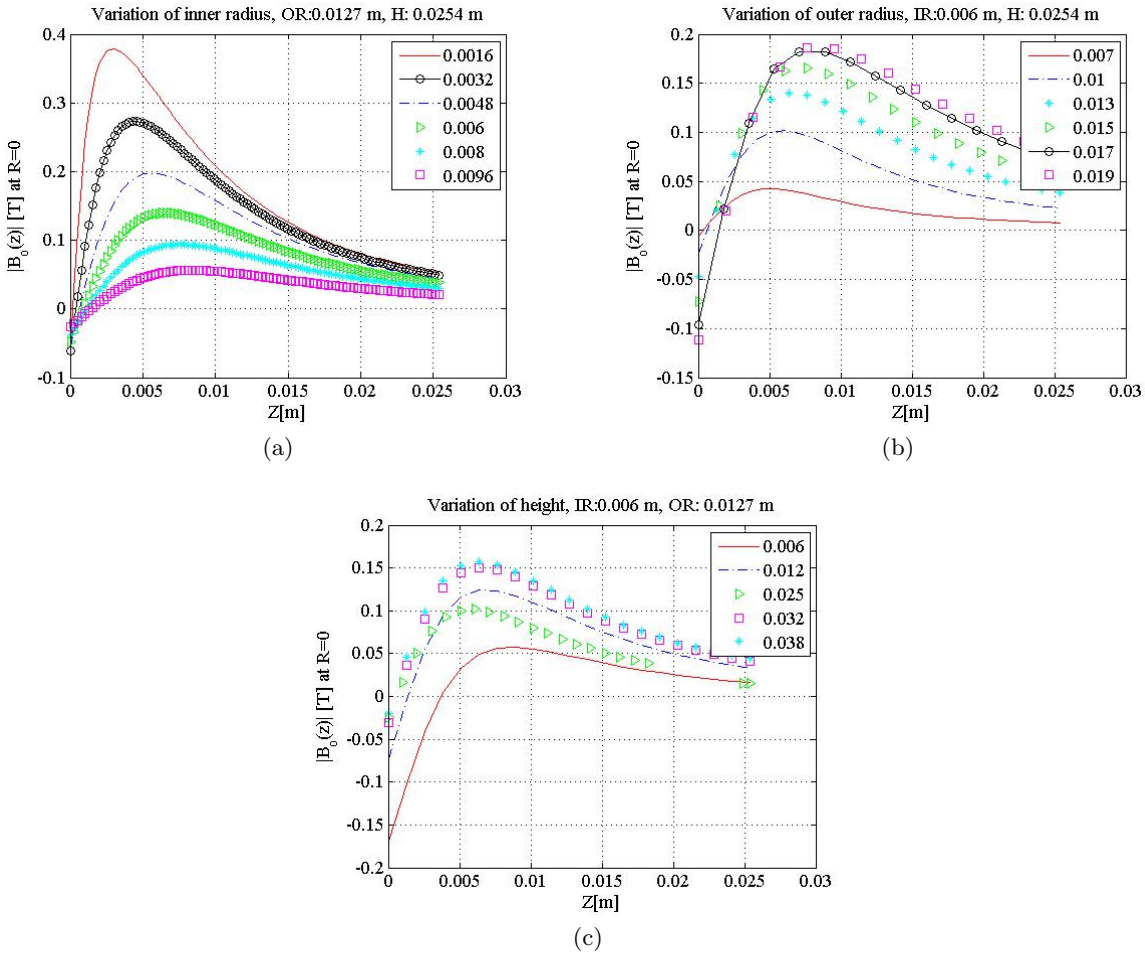

Figure 3.7: (a) Inner radius variations (b) Outer radius variations (c) Height variations.

density is marginal. Moreover, the saddle point's distance from the magnet's surface appears to be independent of any height variations.

In applications, an array of permanent magnets will be stacked to achieve a saddle point at specific locations (1-10 mm) above the magnet surface. The object under test will be placed at the saddle point. To overcome large magnetic field gradient effects, specific pulse sequences such as Carr-Purcell-Meiboom-Gill (CPMG), spin echoes or Hahn echoes[18, 23, 97] will be applied to acquire desired NMR signals from samples under test.

On the basis of initial simulation findings as seen in Fig. 3.7, several variations in the magnets dimensions and geometry were performed. These variations were tailored to obtain the highest

Figure 3.8: Cross-sectional view of different magnet assemblies tested. Here N and S represent the magnet poles. IR - Inner radius, OR - Outer radius, H - Height

estimate of the NMR signal from the protons present in the sample at the saddle point. Table. 3.2 is a summary of the magnet dimensions and approximations of estimated NMR voltage (using equation 3.2) for an assumed B_1 of 0.001 T and a coil current of 5 A. In real applications, the spatial variation in B_1 needs to be incorporated in such calculations.

Table 3.2: Summary of estimated NMR voltage for different inner radii and resonant frequency

Inner Radius (m)	B_0 (T)	V_{NMR} (nV)	f (MHz)
0.0016	0.38	12	16.12
0.003	0.27	12	11.63
0.006	0.14	9	5.95
0.009	0.06	5	2.40

As previously discussed, further flexibility in the position and location of the saddle point can be obtained by placement of concentric magnetic inserts within the ring magnet. In order to test this, a concentric ring magnet and a cylindrical insert were tested and the effects on the position and size of the saddle point were recorded. An inner radius of 0.006 m was used to provide sufficient inner diameter for placing a magnetic insert.

Fig. 3.8, shows a cross-sectional view of the different geometries tested. From Fig. 3.9, it is observed that the static flux density increases with addition of a magnetic insert. This implies that the precession frequency also increases. For the geometry involving two concentric rings, it is observed that the saddle point has a higher magnetic flux density and it's location is closer to the magnet surface. At the same time in the case of the concentric cylinder, the location of the saddle

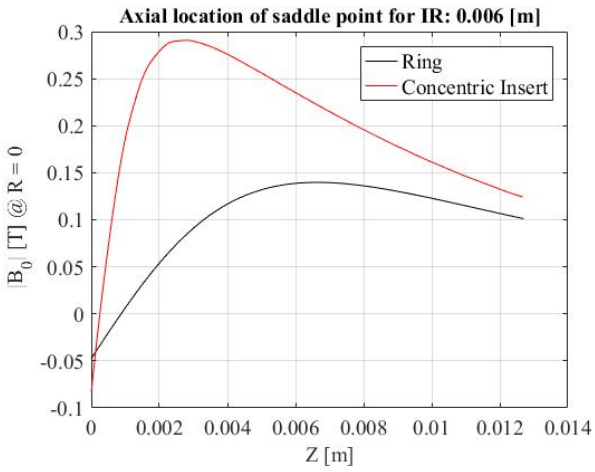

Figure 3.9: Location of saddle point for different magnet assemblies

point is the same as the concentric ring. In fact, from the voltage sensitivity maps, Fig. 3.10b and 3.10c, it is observed that multiple off-axis saddle points may exist for such geometries.

The axial saddle point using magnetic flux density maps for different magnet geometries may be observed in Fig. 3.10. Here, the voltage sensitivity is estimated using equation 3.2. After fine tuning the position of the inserts to obtain maximum NMR voltage at the saddle point, it is observed that the effect of the magnetic insert is comparable for the concentric ring and cylinder, Table. 3.3. Minor off-axis saddle points are observed though these points haven't been used for estimating the NMR voltage. On addition of the insert, the saddle point location shifts closer to the magnet surface and the required detection frequency has increased.

Another view of the magnetic flux density for varied inserts may be observed in Fig. 3.11 and Fig. 3.12. These are cross-sectional views for ring magnets with cylindrical and ring inserts of different heights. The insert position is varied to obtain large saddle points. Since the magnetic flux density increases with insertion of another magnet, the resonant frequency also increases. The magnetic flux density simulations show that with a full ring/cylindrical insert, the estimated NMR signal almost doubles with a slight increase in precession frequency.

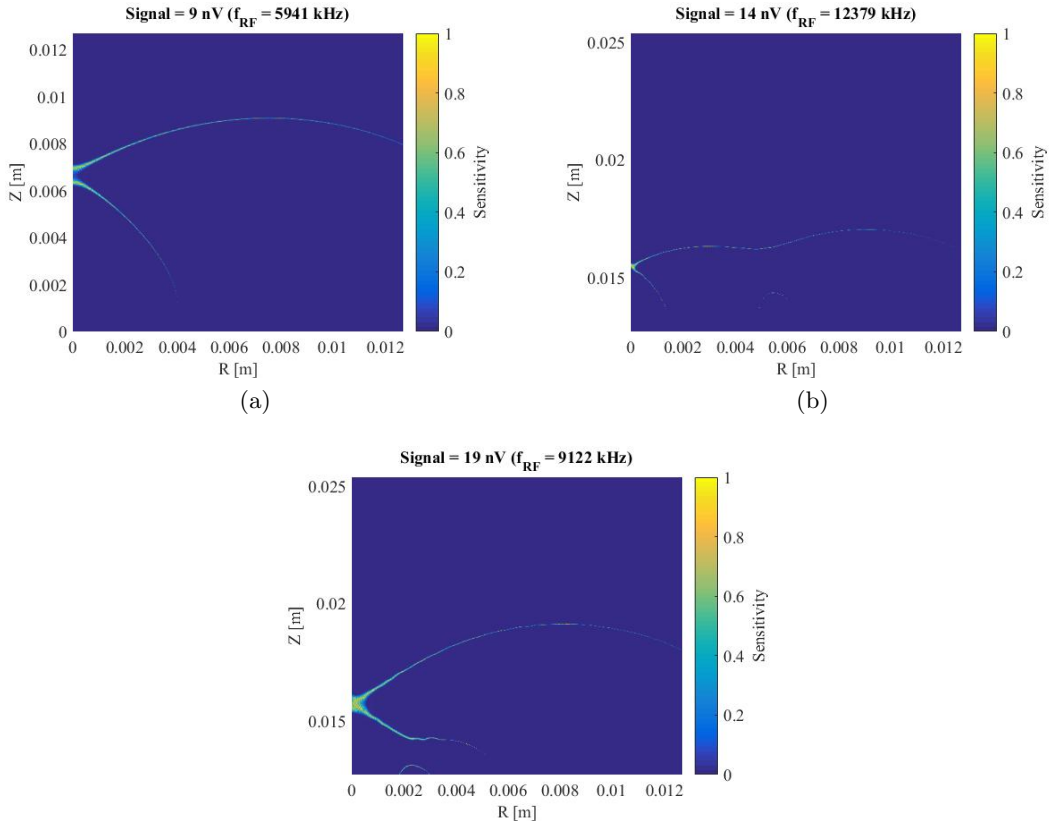

Figure 3.10: Saddle point for (a) Ring (b) Unaligned concentric insert and (c) Aligned concentric insert with IR: 0.006 [m]

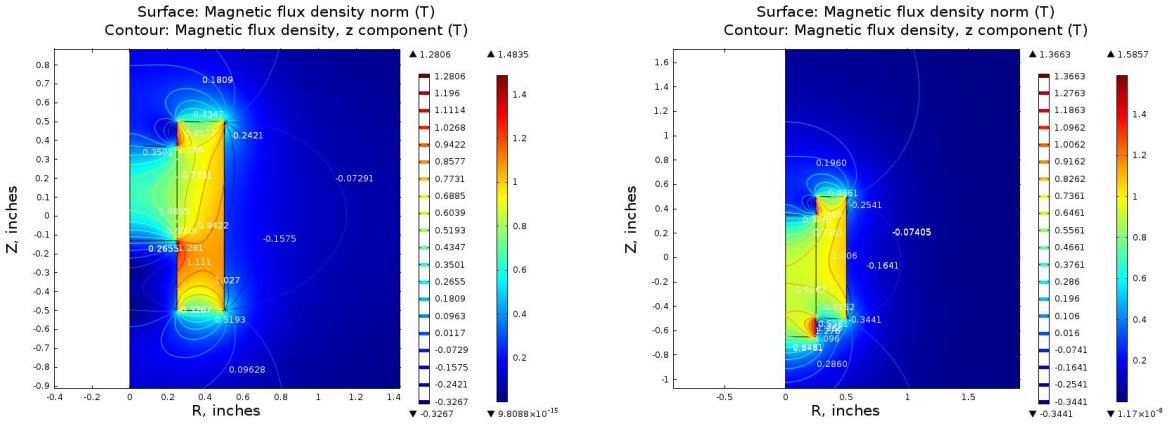

Figure 3.11: Simulations for various saddle points on addition of cylindrical inserts within ring magnets

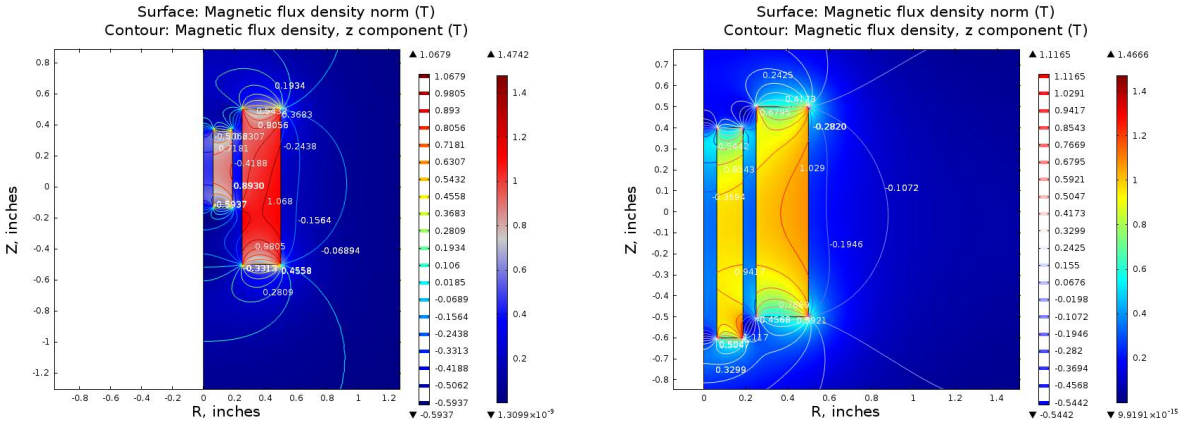

(a) Ring Half Cylinder

(b) Ring Full Cylinder

Figure 3.12: Simulations for various saddle points on addition of ring inserts within ring magnets

Table 3.3: SNR and Signal voltage for different magnet geometries for IR: 0.006 [m]

Geometry	B_0 (T)	V_{NMR} (nV)	f (MHz)	Insert Shift (m)
Ring	0.14	9	5.9	NA
Concentric Insert	0.29	14	12.3	0
Concentric Insert	0.21	19	9.12	0.004
Dual Magnet	0.28	31	11.7	NA

3.7 Effect of using dual concentric ring magnets

Another approach towards maximizing the area of saddle points is the use of two permanent magnet geometries placed symmetrically opposite to one another along the same axis. The distance between two symmetrical ring magnets was varied to identify distances at which maximal stable field regions may be obtained. Additionally, variations were controlled such that samples as large as 0.02 m may be placed between the symmetrical magnets. However, even in such cases the detection region (where field is uniform) is between 0.01 to 0.018 m. In contrast to the ring magnets, on using the dual magnet assembly the NMR signal was estimated to be three times larger, albeit obtained at twice the operational frequency, 3.14. Additionally, while the saddle point occurred at

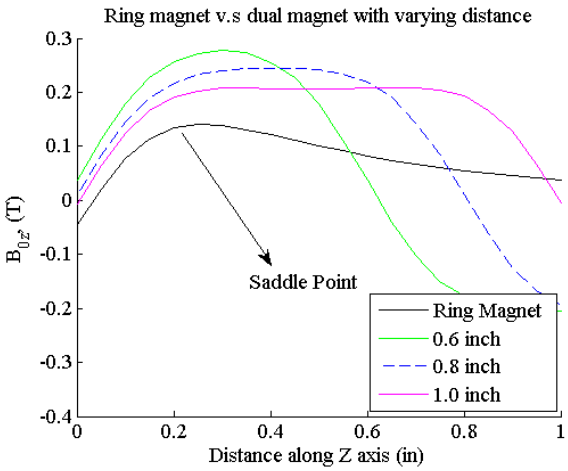

Figure 3.13: Comparison of static field strength for ring and dual magnet

distances equal to the inner radius for ring magnets, in the case of dual magnets the saddle point occurred at the center of the two magnets. The static field strength decreased with an increase in the distance between the magnets. However, the dual magnet seemed to be much more efficient than other prior magnet designs in the sense that a larger signal amplitude and detection region could be obtained.

3.8 Conclusions

Several different parameters that contribute to the existence of saddle points in non-uniform magnetic fields were investigated. For the case of ring magnets, the location of the saddle point was found to be dependent on the magnet's inner and outer radii. The magnet's height didn't affect the location or static field strength significantly once the height was larger than the magnet's outer diameter.

With addition of magnetic inserts, the static field strength increased by a factor of half. Besides the improvement in static field strength, the axial position of the saddle point was affected and secondary saddle points were observed at off-axis locations. Moreover, with the addition of the insert, the estimated NMR voltage also increased by a factor of half. The SNR also improved with improvements in static field strength and minimal spatial variations.

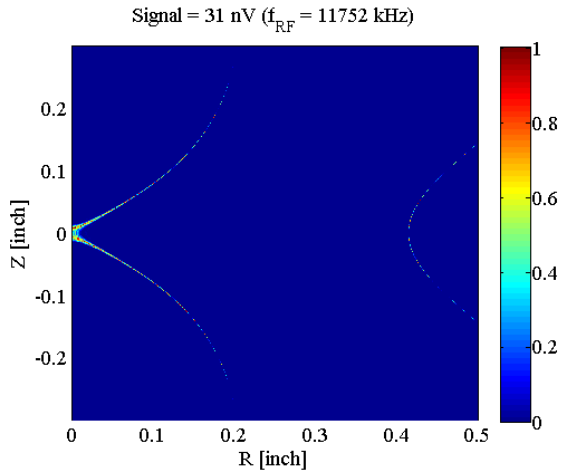

Figure 3.14: Voltage sensitivity map depicting saddle point for dual ring assembly with an inner radius of 0.006 [m]

Lastly, with the use of dual ring magnets, the magnetic flux density and detection volume increased. However, the spacing between the magnets limited the actual detection region.

From these simulation results, it is expected that measurements with the designed magnet geometry and insert would enable localized NMR detection at approximately 1-10 mm near the magnet's surface.

3.9 Future work

From this work, a systematic simulation study for the ring magnets was performed and the relation between the NMR voltage and the saddle point was understood. Incorporating the receiving coil characteristics would provide a better perspective of the received voltage. Moreover, the characteristics of the receive coil such as operational bandwidth and coil resistance would contribute to improvements in estimating the NMR voltage and SNR. Finally, measurements of signal decay time for different biological specimens would validate meaningful medical diagnostic capabilities.

CHAPTER 4. PULSED FIELD GENERATION

4.1 Pulsed Magnetic Fields

Once the static field from the permanent magnets orients the magnetic moments, a pulsed field is needed to reorient and detect the response of the magnetic moments. This is because force-based magnetic field measurements require interacting magnetic fields [98]. In such measurements, a magnetic dipole placed in a uniform external magnetic field experiences a torque. Then,

$$\tau = m \times B \tag{4.1}$$

the turning force (torque, τ) is proportional to the strength of the applied magnetic flux density (B) and the associated dipole magnetic moment (m) [98].

Magnetic resonance measurements are an extension of force-based magnetic field measurements wherein the magnetic dipoles are nuclei, electrons or protons. In nuclear magnetic resonance (NMR), the magnetic moments associated with the nuclei act as the magnetic dipoles. A static external biasing field is first applied to provide a bias magnetic field and align all magnetic moments. Then, a pulsed magnetic field is applied. The pulsed field creates a torque and causes reorientation of magnetic moments. When the frequency of the applied pulsed field is equal to the energy difference between quantized nuclear states, nuclear transitions occur between the energy states. This condition is when nuclear magnetic resonance occurs [99]. Once the pulse is removed, nuclei return to their original energy states. Minute signal produced during this process are then acquired by using detection coils which are placed transverse to the direction of the applied static field.

In conventional NMR measurements the static field is much higher than the pulsed field [18]. This means that once the pulsed field is removed, the magnetic moments revert back to their original alignment along the static field. Consequently, to detect magnetic resonance signals, the detection coils need to be placed in alignment with the pulsed field instead of the static field. Therefore,

pulsed fields are applied in a direction perpendicular to the static field, enabling detection of the minute NMR signals by alignment with direction of maximum flux change .

In unilateral NMR, the detection mechanism and principle of operation remains the same as in conventional NMR. However, the external magnetic field strength is considerably lower due to the use of permanent magnets or one-sided application of static field. In this situation, the magnitude of the applied pulsed field can become comparable to the external magnetic field. However, due to its frequency of operation, the pulsed field is capable of initiating temporary reorientation of magnetic moments. Detection of magnetic moment reorientations may be difficult in low fields; consequently, it becomes necessary to improve and control the design of the pulsed oscillating field such that the required magnetic moment reorientation and NMR detection processes can still occur under low-field conditions [100].

4.2 Need for pulsed fields

The pulsed magnetic field is used alongside the static field generated by the permanent magnets. The pulsed field causes transverse reorientation of the magnetic moments aligned along the static field. To achieve such reorientation's, the oscillation frequency of the pulsed field is tuned to be the same as the precession frequency of the test samples. As specified previously, the static field strength determines the precession frequency of the magnetic moments. Correspondingly, the pulsed field frequency needs to be tuned with respect to modifications in the static field. Additionally, the strength of the pulsed field is much lower than the static field to avoid any magnetic saturation of the magnetic moments.

The existing pulsed magnetic field generation systems use expensive equipment to generate a pulsed magnetic field and simultaneously receive signals on the same coil. In this chapter, a design for a low field, low frequency (less than or equal to 5 MHz), pulsed magnetic field generation circuit suitable for transmitting pulsed magnetic fields is described. A pulsed sinusoidal current is passed through an inductive load controlled by a high-speed switching field effect transistor (FET). In the initial design, the inductive load resonates at a frequency of approximately 2 MHz which

corresponds to the precession frequency of ^{1}H protons in an external magnetic flux density of 0.05 T. The designed circuit is further modified for improved operations and can be tuned to operate at resonant frequencies of other nuclear species as well.

4.3 System overview

The design of the pulsed magnetic field generator requires several integral units. The units should be able to achieve the following:

1. Pulsed sinusoidal signal at Larmor precession frequency
2. Rapid switching of coil at Larmor precession frequency
3. Sufficient current through coil to produce pulsed magnetic fields
4. Adequate pulse width to achieve transverse precession

A systems level schematic of the designed circuit, as shown in Fig. 4.1, highlights the different design stages.

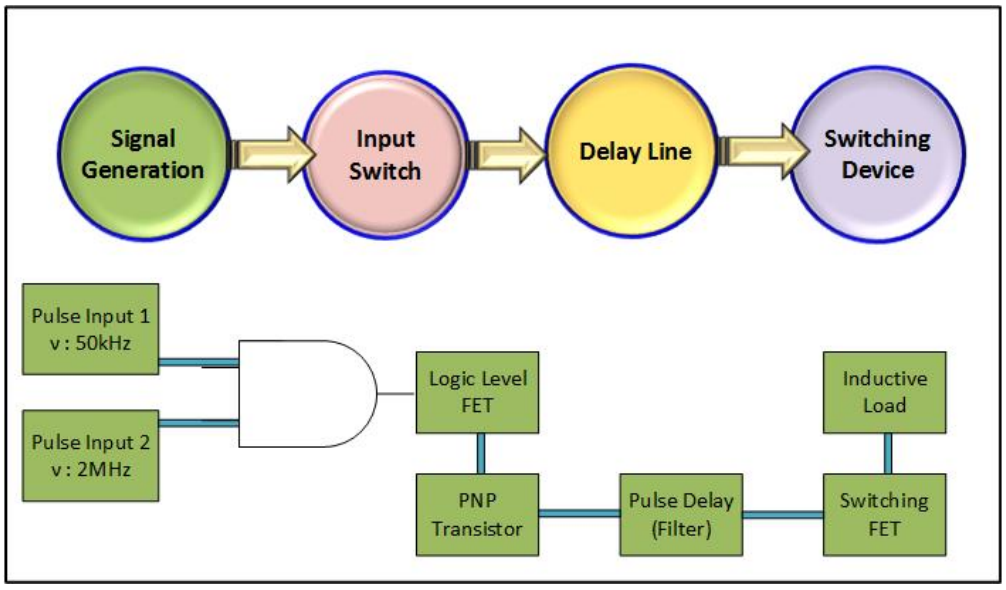

Figure 4.1: System block diagram. The four system design blocks are represented at the top.

In order to obtain a pulsed sinusoidal current, a pulsed sinusoidal voltage is used to activate the switching FET. Then, the signal generation, amplification and delay stages as seen in Fig. 4.1, are used as the pulse forming network.

Two square wave inputs, as depicted in Fig. 4.3, were combined and applied to a pulse shaping stage known as an electromagnetic delay line. The delay line generates a band limited pseudo-raised cosine pulse. This pulse drives the gate of a FET-based switch that is connected to a coil at the drain. Often, a capacitor may be connected in series or shunt with the coil to achieve sustained oscillations at the required Larmor frequency. In this design such a connection was avoided to reduce ringing or occurrence of other secondary oscillations. To obtain the desired pulse width, the input pulse parameters and delay line elements are tuned to the required operational frequency.

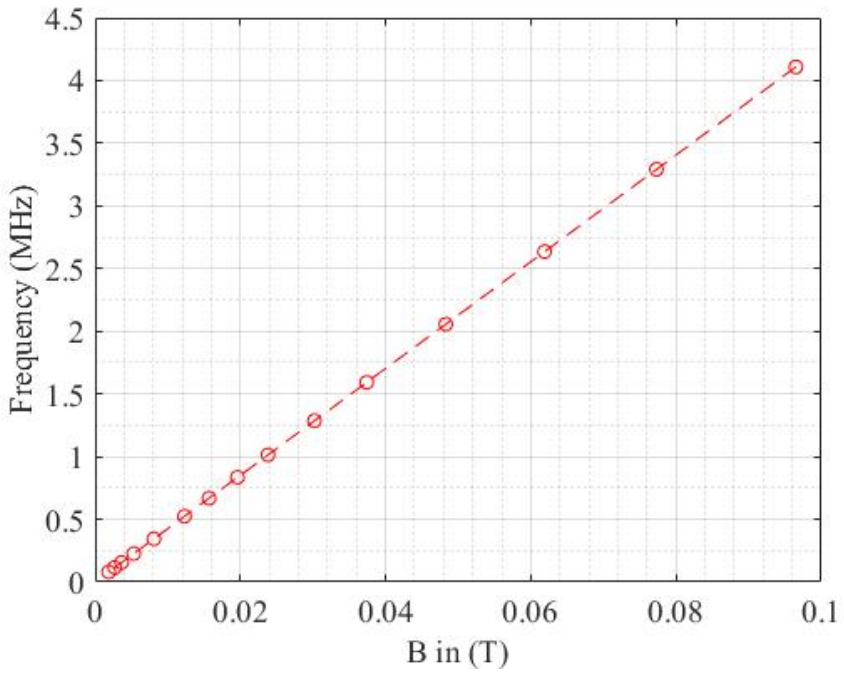

Figure 4.2: Linear dependence between magnetic flux density and frequency as described in equation 2.1

In this initial design, a lower precession frequency was selected (approximately 2 MHz) for operation with NMR systems that generally operate at low flux densities. The linear dependence

between the precession frequency and static field strength, as described in equation 2.1, and observed in Fig 4.2, highlights the limitation on the maximum operational frequency, namely the static field strength. It is important to note that ^{1}H has a gyromagnetic ratio of 42.1 MHz/T and thus for an external flux density of 500 G the precession frequency would be approximately 2.12 MHz, which is approximately equal to the design frequency of the initial circuit design. Correspondingly, forming a design perspective on the expected pulsed field, the oscillation frequency depends on the static field and the pulsed field strength depends on the coil geometry. A comparison between the calculated field and current for different coil geometries is seen from Table. 4.1.

Table 4.1: Comparison of calculated field and current for different coil geometries in free space

Coil Geometry	Dimension	Turns	**Magnetic Field**	**Current**
Current loop	R = 0.05 m	1	1.2E-4 T	10 A
Solenoid	L = 0.05 m	10	2.5E-3 T	10 A
Toroid	R = 0.05 m	10	0.4E-3 T	10 A

4.4 System design and pulse parameters

The designed circuit will be described according to the different stages listed in Fig. 4.1. In the first stage or the signal generation stage, two different pulse generators were used to generate square pulses. The frequencies were selected to be the modulation frequency (which was the same as the Larmor precession frequency) and the pulse repetition frequency (which was selected such that sufficient gap may be obtained between adjacent pulses). The pulse repetition frequency may be externally controlled to obtain specific pulse repetition patterns or sequences in operation. Additionally, the pulse width needs to be controlled to obtain magnetic moment rotation by 90^o or 180^o. For the designed system, both the pulse generators were synchronized using an external clock signal (at 10 MHz).

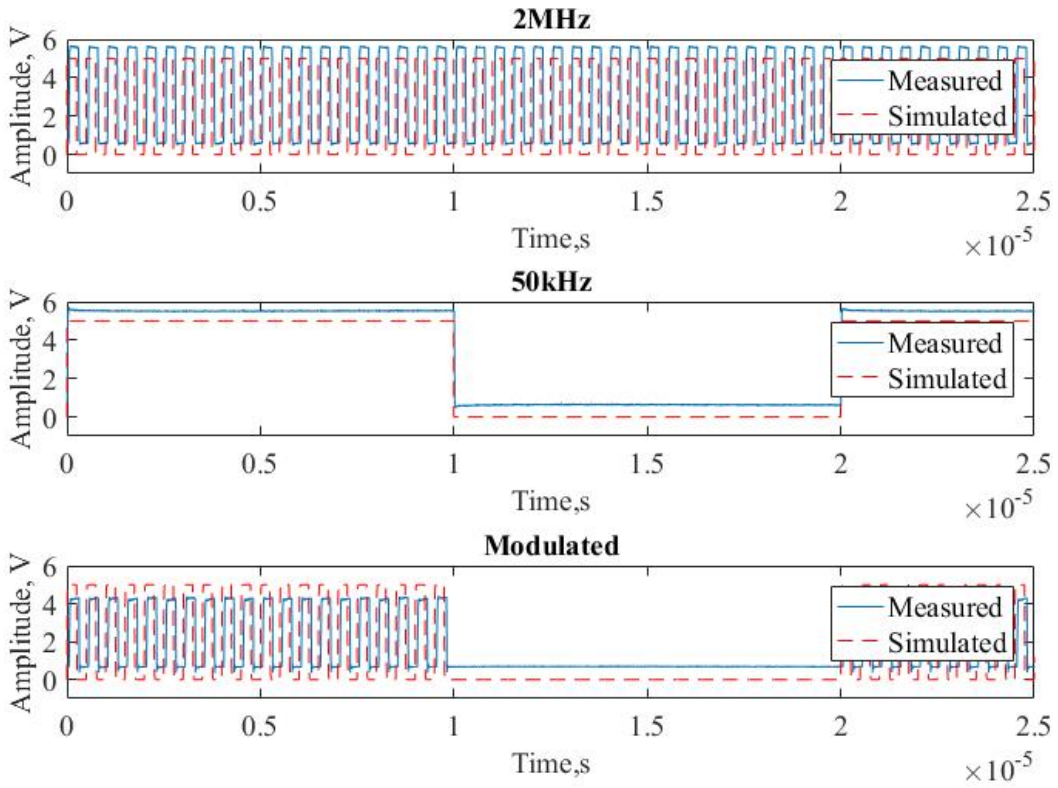

Figure 4.3: Simulated vs Measured pulsed sinusoidal generated at the output of the mixer (AND operation). Input pulse frequencies were selected to be 50 kHz and 2 MHz respectively.

The generated square pulses, as shown in Fig. 4.3, were then applied as inputs to a logic AND gate and the output were applied to the initial switching stage of the system. Due to lower operational frequency, the AND gate was adequate for combining the two signals. For higher operational frequencies (greater than 12 MHz) other methods may be used. A schematic of the implemented circuit is seen in Fig. 4.4. In the input switching stage, the generated pulsed sinusoidal is applied to the gate terminal of a logic level FET. The logic level FET acts as a buffer between the signal generation and initial switching stage. The FET has a low on resistance and gate threshold voltage and can thus respond quickly to fast switching signals. The drain terminal of the FET is

connected to a PNP transistor as seen in Fig. 4.4. The transistor can act as both an amplifier and a switch. The bias condition of the transistor may be easily varied by changing the biasing resistors. The presence of the 220 Ω feedback resistor between the base and emitter helps maintain the base-emitter junction forward biased and the base-collector junction is held reverse biased. Therefore, the PNP transistor operates in the active region. In the absence of the 220 Ω resistor, the transistor wouldn't be in the active region of operation. Additionally, the bias condition may be modified by changing the 120 Ω resistor.

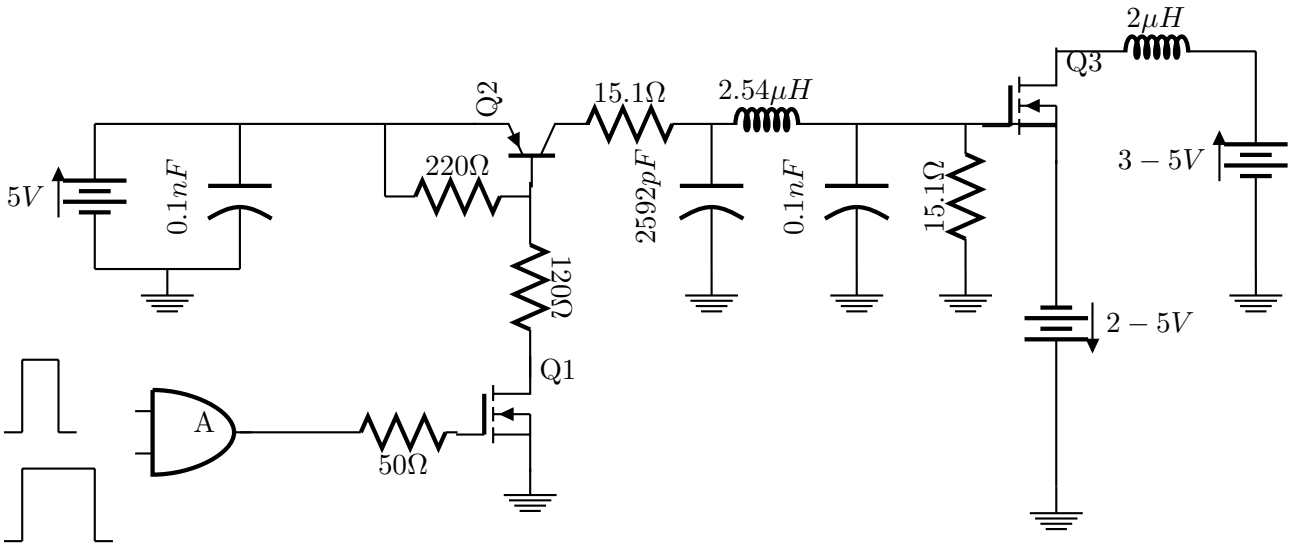

Figure 4.4: Schematic of the designed circuit.

A contrast between the experimental and simulation results can be observed in Fig. 4.5. Here, it is observed that the high frequency oscillations aren't obtained in simulations unless the input signals duty cycle is reduced from 50% to 20%. However, measurements at the base terminal, Fig. 4.5b, seem to indicate the presence of a modulated input signal. The collector voltage, Fig. 4.5c, follows the signal at the base though at higher duty cycles the pulsed oscillations aren't observed in simulation or measurement.

Meanwhile, a sufficient amount of current (300 mA) is needed for operation of the electromagnetic delay stage. The output measured at the PNP transistor, Fig. 4.5, is subsequently applied

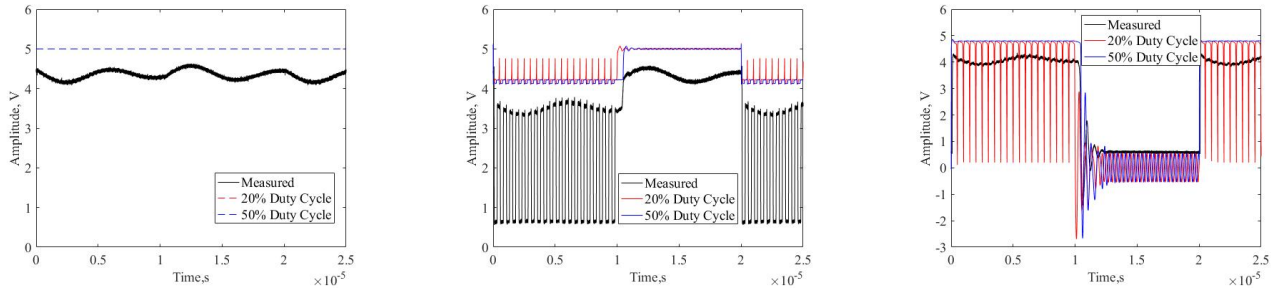

(a) Emitter voltage (b) Base voltage (c) Collector voltage

Figure 4.5: Simulation vs Experimental Measurements at the PNP transistor

to the 15 Ω resistor in the electromagnetic delay line. In this initial design, the delay line acts as the pulse forming network [101]. It is tuned to operate at a frequency of 2 MHz as that was the expected frequency for hydrogen precession for an externally applied flux density of 0.05 T. A pulse repetition rate of 20 μs was selected. Generally, a delay line comprises a set of capacitors and inductors which cause a phase delay to the applied signal. Such networks are often used to generate a raised cosine pulse. The rise and fall time of the pulses are adjusted by tuning the inductive and capacitive elements in the delay line. Moreover, the addition of multiple poles in the network gives users the flexibility to obtain different waveshapes at the output.

In this circuit implementation, in the final switching phase, the impedance of the delay line elements needs to be scaled with respect to the impedance parameters of the switching device. In this design, the input capacitance of the switching FET was used to scale the impedance of the delay line elements. The scaling factor, K, and the other pulse parameters are summarized in Table. 4.2. Initially, a low pass prototype, was obtained for a 50Ω impedance and then scaled using the scaling factor based on the gate capacitance of the switching device. The input pulse parameters were adjusted to obtain a pulse with a pulse width of 10 μs.

Table 4.2: Electromagnetic Delay Line Parameters designed for a frequency of 2 MHz

Parameter	50 Ω Model	Scaled Model
$\mathbf{K} = \frac{C_{fetinput}}{C_{50OhmModel}}$	1	3.26
$\mathbf{R} = \frac{1}{2}\sqrt{\frac{L}{C}}$	50	15.4 Ω
$\mathbf{L} = 4R^2C$	7.95 μH	2.5 μH
$\mathbf{C} = \frac{1}{2R\omega}$	795 pF	2592 pF

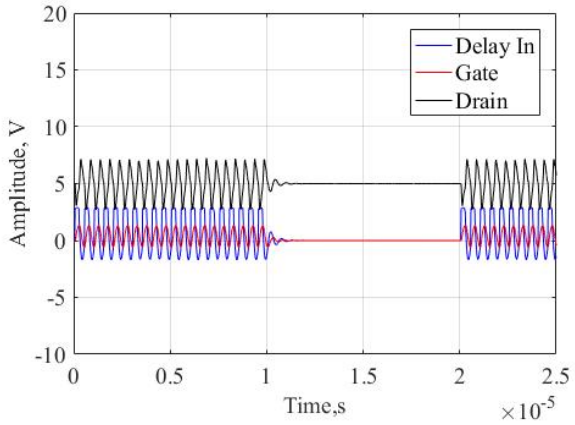

(a) IRF 510, 20% duty cycle

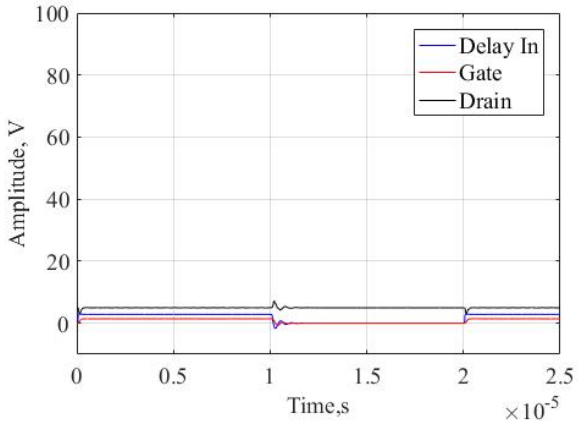

(b) IRF 510, 50% duty cycle

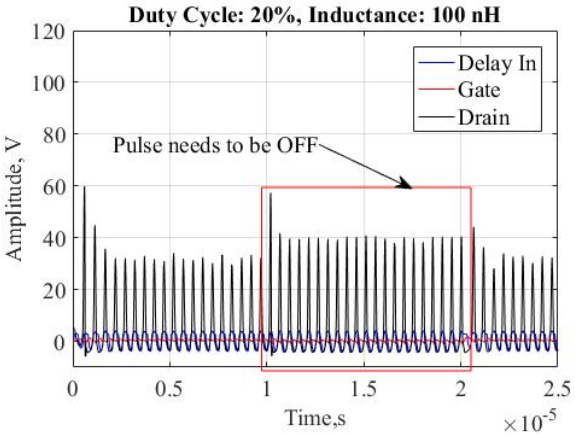

(c) IRF 540, 20% duty cycle

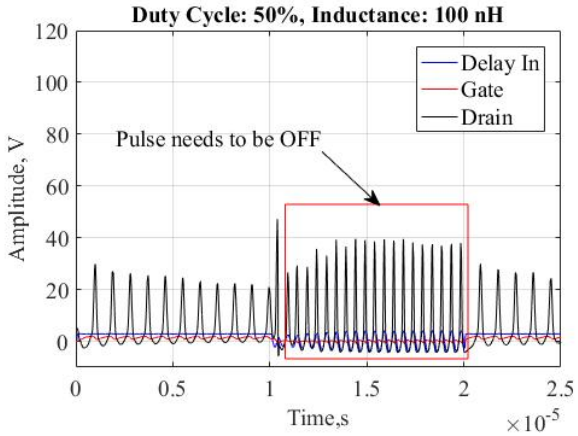

(d) IRF 540, 50% duty cycle

Figure 4.6: Comparison of signals at the delay line and switching device for an inductance of 100 nH

Simulations were performed using two different MOSFET's as switching devices. IRF 510 a fast switching but low current MOSFET and IRF 540, a fast switching and a high current MOSFET were used. The motive of using these two different devices was to understand the loading effects on the delay line based on the device characteristics.

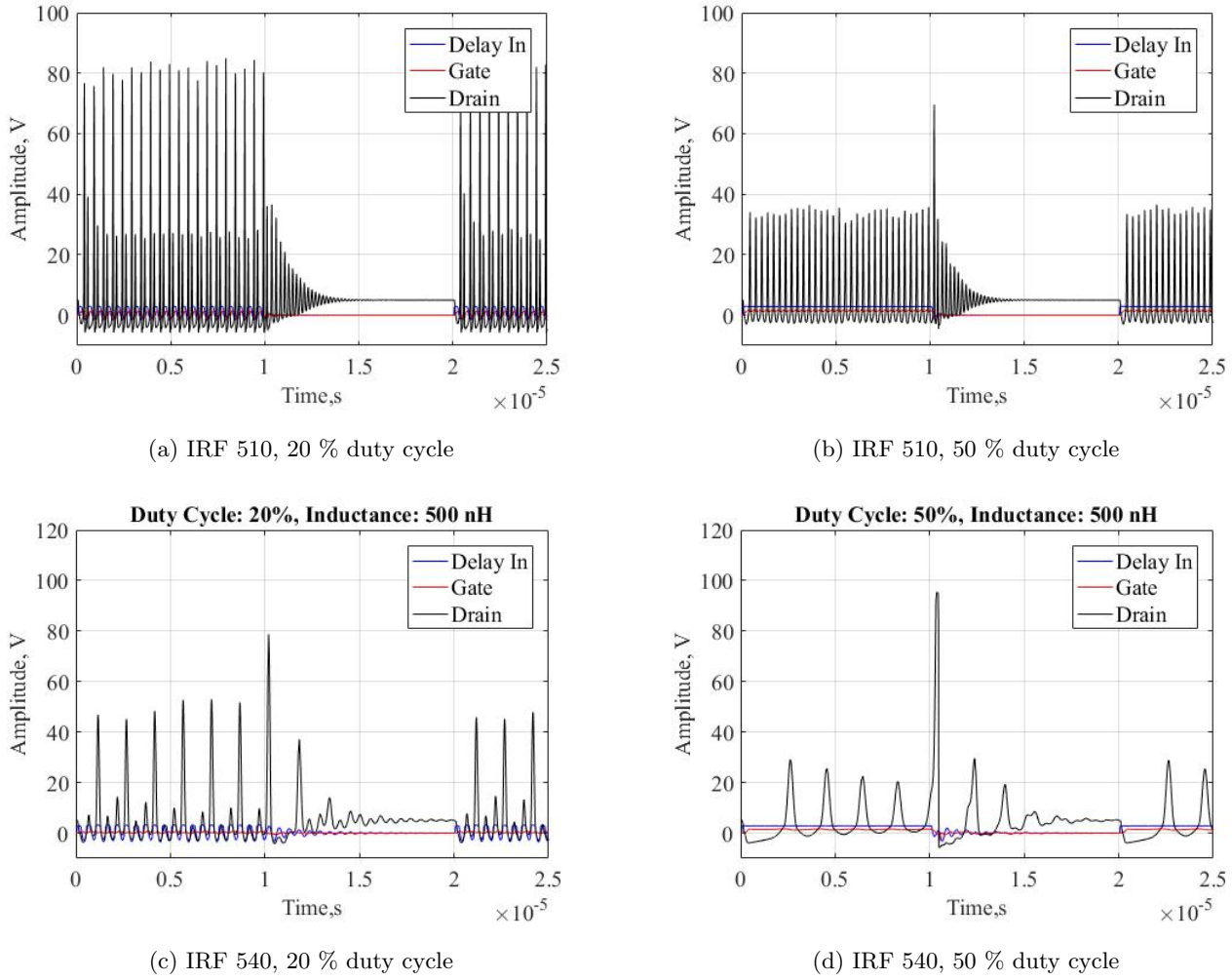

(a) IRF 510, 20 % duty cycle

(b) IRF 510, 50 % duty cycle

(c) IRF 540, 20 % duty cycle

(d) IRF 540, 50 % duty cycle

Figure 4.7: Comparison of signals at the delay line and switching device for an inductance of 500 nH

Two other parameters were found to be important in designing the final switching stage. These were (i) the load inductance and the (ii) duty cycle of the applied pulse. In Fig. 4.6, it is observed

that for IRF 510, Fig. 4.6a and 4.6b, with a load impedance of 100 nH, with an increase in the pulse duty cycle, the pulsed oscillations do not pass through the delay line and the output oscillation frequency is not accurate. However, with IRF 540, Fig. 4.6c and 4.6d, while the pulsed oscillations still appear at the drain, the coil rings and remains on during the time the pulse is switched off. This observation implies that while a higher duty cycle can be sustained with IRF 540, other mechanisms need to be implemented to contain the ringing due to the coil.

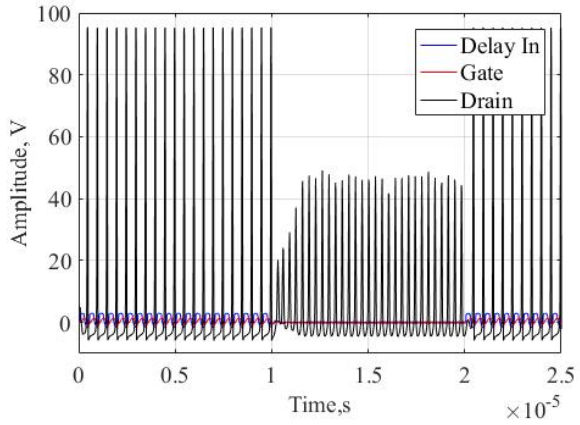

(a) IRF 510, 20 % duty cycle

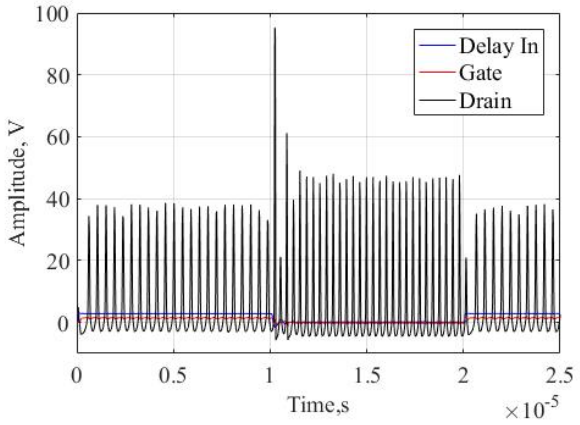

(b) IRF 510, 50 % duty cycle

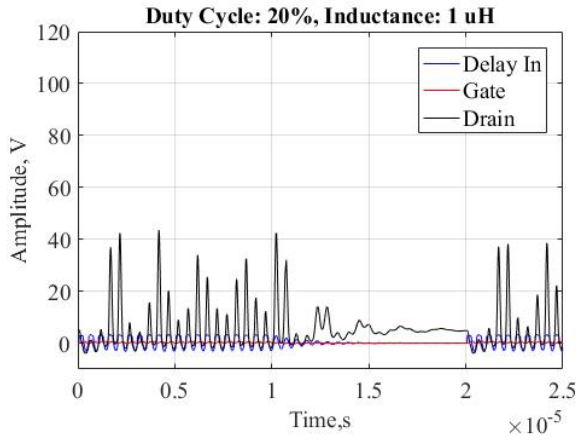

(c) IRF 540, 20 % duty cycle

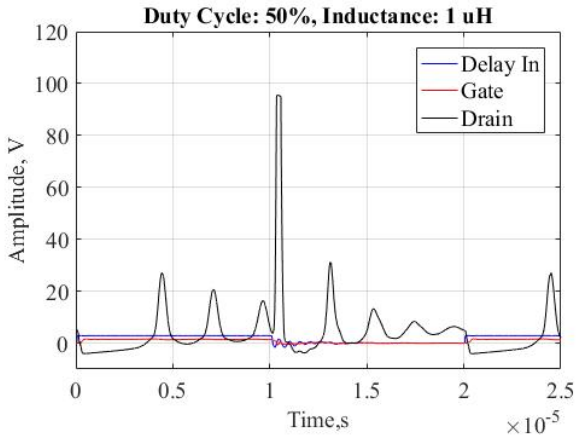

(d) IRF 540, 50 % duty cycle

Figure 4.8: Comparison of signals at the delay line and switching device for an inductance of 1 μH

To observe the effect of the coil inductance two other studies were performed with the same FET's and similar simulation parameters. These studies used a coil of 500 nH and 1 μH respectively and the observations are summarized in Fig. 4.7 and Fig. 4.8.

For an inductance of 500 nH, ringing was still observed with both FET's with the variations in duty cycle. With IRF 540, Fig. 4.7c and Fig. 4.7d, the ringing was significantly reduced. However, the pulse repetition frequency was also impacted and a minimal number of pulses were transmitted.

Based on these simulation results, it was expected that signal ringing could be minimized once the coil inductance was increased. However, on increasing the coil inductance to 1 μH, with IRF 510, Fig. 4.8a and 4.8b, it was observed that the ringing was still present during the pulse down time. With IRF 540, Fig. 4.8c and Fig. 4.8d, while the ringing was not present, the pulse oscillation frequency was impacted due to the high inductance of the coil. Therefore, from these simulation results, it is apparent that a delicate balance exists between the coil inductance and the switching device.

4.4.1 Simulated current based on the inductance

The modulated pulse as obtained at the output of the delay line is applied to the gate of the fast switching FET. The selected FET can sustain high drain currents (up to 100 A) and high switching speeds (approximately 30 ns). Initial designs had a resonant RLC at the load of the FET. This load was assumed to sustain oscillating magnetic field that would be generated by the inductive coil. A feedback loop was also provided for quick dissipation of the pulse during the off-time of the signal. After initial measurements and simulations, the resonant load was replaced by a non-resonant inductive load to minimize the high ringing introduced in the resonant configuration.

Simulations for the current through IRF 510 with different duty cycles and IRF 540 may be observed in Fig. 4.9 and Fig. 4.10 respectively. Through the simulations for IRF 510, it was observed that with a higher inductance, the pulse ringing significantly increases with an increase in the value of inductance. The ringing was not eliminated despite the use of varying duty cycles. A variation in the drain voltage, Fig. 4.10c or Fig. 4.10d, to ensure the FET's bias condition did

not affect the simulated current levels ensuring that the FET was sufficiently biased to operate in the desired region and unaffected by the range of the inductance used as the load.

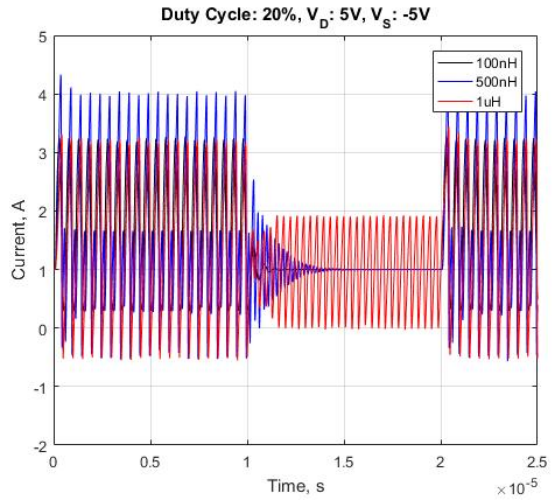

(a) 100 nH

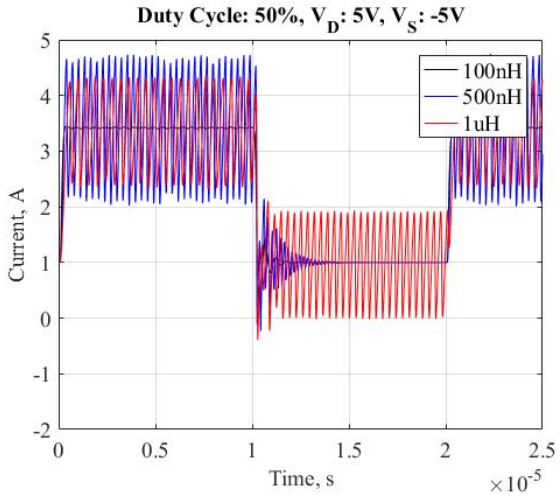

(b) 100 nH (Zoomed)

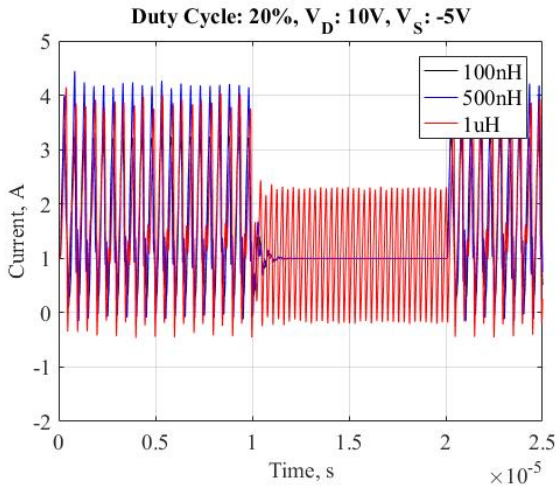

(c) 500 nH

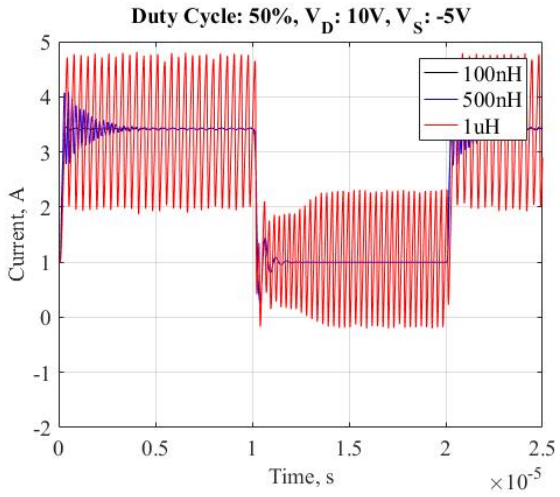

(d) 1 μH

Figure 4.9: Simulated current for IRF 510 with varying values of inductance, drain voltage and duty cycles

Lastly, simulations for the current through IRF 540, Fig. 4.10, showed that higher current levels were obtained at the cost of the pulse ringing during the signal off time. Additionally, with

an increase in inductance, the pulse oscillation frequency reduced along with a reduction in the maximum current that could be passed through the coil. Therefore, larger inductances weren't preferred for high current applications.

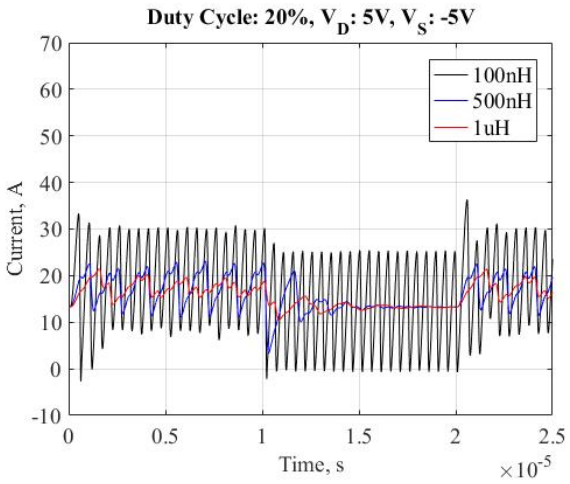

(a) 100 nH

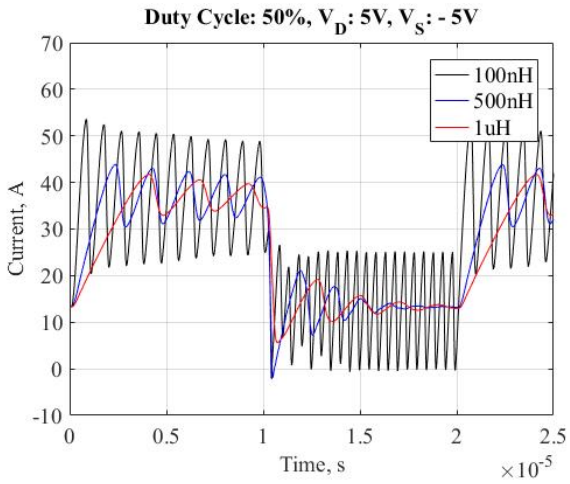

(b) 100 nH (Zoomed)

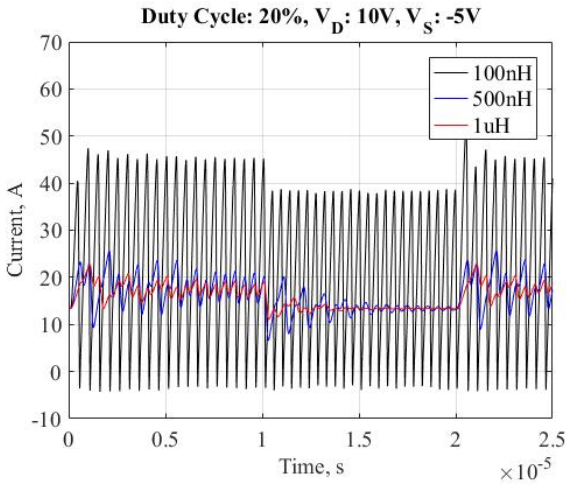

(c) 500 nH

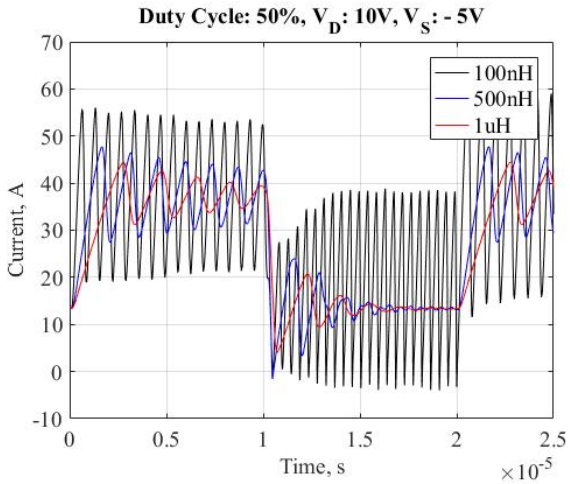

(d) 1 μH

Figure 4.10: Simulated current for IRF 540 with varying values of inductance and duty cycles

4.5 Experimental measurements

A prototype of the designed pulsed field generator is observed in Fig. 4.11. The circuit can generate variable oscillating magnetic fields at several operational frequencies based on the electromagnetic delay tuning. The signal generation stage in this prototype can also be modified to obtain continuous NMR pulses for other NMR applications.

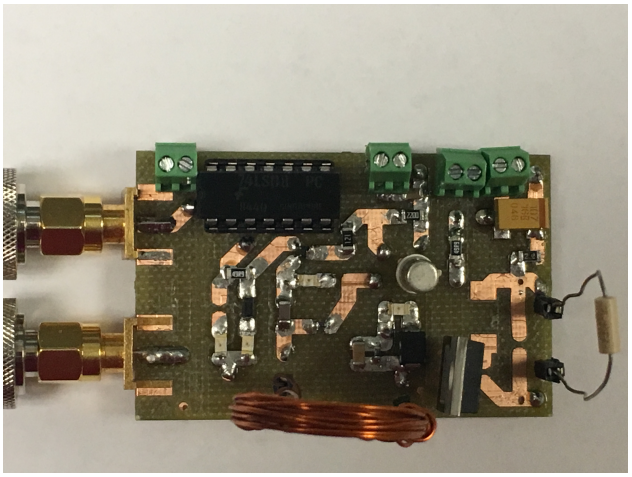

Figure 4.11: Designed pulsed field generator circuit prototype.

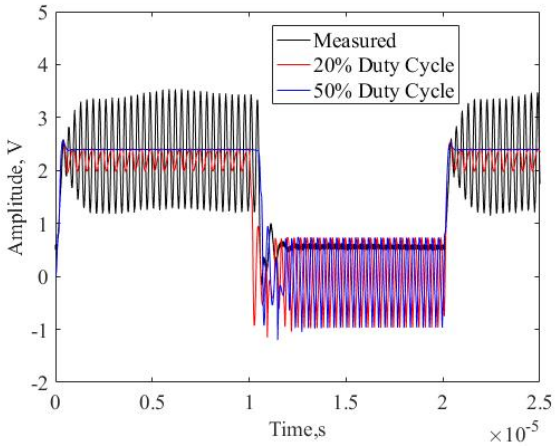

Figure 4.12: Voltage measured at the end of the pulsed delay line. This is applied to the gate of the switching FET. The slight DC offset is necessary for activation of the switching FET.

To ensure operations, the voltage at the gate terminal, Fig. 4.12, should be sufficient to activate the switching FET. A negative offset is applied at the source terminal of the switching FET such that a deep conduction channel forms between the drain and source on application of appropriate gate voltage. While the measured waveform clearly represents the pulsed sinusoidal signal, the simulated waveform, depicts oscillations only with a 20 % duty cycle. Sufficient gate voltage ensures that the FET is biased into the saturation region.

In the present configuration, a peak pulsed voltage of about 9 V, Fig. 4.13, can be obtained at the drain of the switching FET. A representation of the experimentally measured signal levels at the inductive load as a function of time, in the designed circuit is in Fig. 4.13. Experimentally, the peak voltage is 9 V and correspondingly the peak current is recorded as 4.5 A. The corresponding magnetic field may be estimated based on the selected coil geometry. In this design prototype a fixed inductor was used due to its low parasitic resistance and a pulsating magnetic field at a frequency of 2 MHz was generated.

A lower load inductance would allow for faster switching and also have minimal loading effects on the switching FET. In general, a higher inductance would cause large voltage overshoots on turn-off and limit the maximum current through the coil. Meanwhile, a wider pulse width would lead to generation of a higher magnetic field since there would be more current flowing through the inductive load. However, supporting high duty cycles, and high pulsed currents are inherently dependent on the device properties of the switching FET.

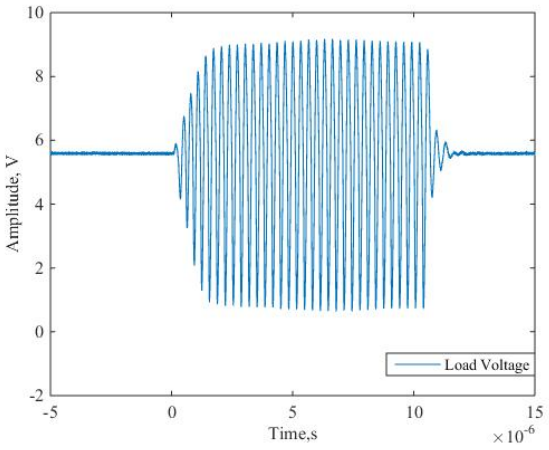

Figure 4.13: Signal measured at the load of the switching FET. A small series resistance of 2 Ω was connected to estimate the peak current, applied drain voltage was 5 V.

Experimental measurements reveal several different factors for consideration. Firstly, the two input pulses need to be synchronized. This is achieved by triggering both the sources with the same external clock pulse at a frequency of 10 MHz. Secondly, the source terminal of the switching FET needs to be sufficiently reverse biased to achieve activation of the gate terminal. Lastly, the resonant configuration of the inductive load and the inductor used within the delay line are both sources of multiple oscillations or ringing. These parameters need to be selected carefully based on the required application. In particular, the operational bandwidth, the resonant frequency of the load, fast discharge of the energy stored in the inductive load are design parameters that need to be carefully analyzed.

The designed pulsed field circuit can operate at a resonant frequency of 2 MHz such that it could be used in an external flux density of 0.05 T. However, the actual impedance parameters used in the circuit vary slightly and were tuned. These impedance variations in the pulsed delay line led to a resonant frequency of 1.8 MHz. The energy stored in the inductive load was also found to produce ringing when connected in a resonant configuration. Thus the resonant configuration was modified to a non-resonant load configuration.

In summary, a design for a pulsed magnetic field generator was simulated, implemented and experimentally verified. Simulation results have shown that a pulsed sinusoidal with a resonant frequency of up to 5 MHz can be easily achieved by tuning the characteristics of the pulsed delay line and the input pulse's duty cycle and optimally selecting the switching FET connected to the inductive load. The choice of the inductance also affects the turn-off time for the switching FET.

4.6 Possible improvements

The design of the prototype pulsed field generator revealed several avenues of improvement. In particular, the selection of the inductive load and the switching device needs to be made by considering the amount of current needed to generate appropriate pulsed magnetic fields. At the same time, the generated magnetic field should have a discharge path when the pulse is switched off and possible ringing at the load needs to be controlled. Another interesting aspect is the user's control on the input pulsed sinusoidal signal. A combination of these parameters will lead to design of a user friendly and stable multi-frequency pulsed magnetic field generator.

Finally, design updates to minimize loading effects and higher frequency operation have been implemented and the improved pulsed field generator design is discussed in the following chapter.

CHAPTER 5. IMPROVED PULSED FIELD GENERATION

From the prior chapter, we know that pulsed magnetic fields can be used to provide instantaneous localized magnetic field variations. In the presence of static fields, pulsed field variations are often used to apply torques and can also be used to measure behavior of magnetic moments in different states of orientation. In this chapter, an update to the design and evaluation of experimental performance of the designed pulsed magnetic field generator is described.

One of the primary challenges of low bias field NMR measurements is low signal to noise ratio. This is caused due to the comparable nature of the bias field and the pulsed field [18]. Therefore, the design of the pulsed field generation circuit needs updates such that it generates controlled pulsed currents and fields which can momentarily exceed the effect of the bias field on magnetic moments. The designed circuit also needs to be tuned to operate at the Larmor precession frequency of ^{1}H (protons) placed in a bias field produced by permanent magnets. Additionally, the designed circuit parameters may be tuned to operate under different bias conditions. In this chapter an improved pulsed magnetic field generation system suited for low field pulsed NMR applications will be described. Circuit simulations will be used to determine design parameters and corresponding experimental measurements are presented.

5.1 Theoretical perspective

For portable NMR applications, the magnitude of the pulsed magnetic field needs to be comparable or lower than the magnitude of the external static magnetic field to achieve temporary magnetic moment reorientation [102]. It is well known that the NMR resonant frequency, ω_o is proportional to the external field, B_o as per equation 2.1. Correspondingly, the induced NMR voltage is considered to be proportional to[94],

$$V_{NMR} \propto \omega_o m \left(\frac{B_1}{I}\right) \tag{5.1}$$

Then, from equation 5.1, it is observed that the measured NMR voltage is directly proportional to the strength of both the static and pulsed field and as per the equation 5.1, inversely proportional to the current creating the pulsed field. Through equation 5.1, it is also evident that the pulsed field and the current are competing factors. In general, a higher current would lead to a higher pulsed field. In actual application, coil parameters also contribute to the field generated and need to be tuned to achieve a higher NMR voltage signal.

There are several ways of achieving high pulsed magnetic fields [103, 104, 105, 106]. From Ampere's law, the simplest way is to increase the current. Alternatively, the coil or inductive load design and parameters may be controlled to achieve higher pulsed magnetic fields [107, 108]. Overall, to be independent of the coil design parameters, in this chapter, our focus is on demonstrating a design wherein we increase the current through the transmitting coil. Subsequent signal detection will be implemented using orthogonal inductive coils.

5.1.1 Obtaining high current

The pulsed magnetic fields need to be enabled only for short durations (between 10 - 100 μs). Due to the requirement of short pulse widths, a large amount of current should flow through the inductor in a very short time (approximately 10 μs for the present design [100]). Then, the fastest way to obtain high current through an inductive load is by allowing a capacitive discharge through the inductor [103, 104]. In order to realize this, a capacitor bank will be used to firstly support the fast rising edge through the inductor and then to provide sufficient current during the applied pulse width. It is well known that the current drawn from the capacitor will be proportional to the time rate of change of voltage across the capacitor. In our design, capacitors, which can support rapid changes in voltage should be used. Based on equation 5.2, a pulse width of 10 μs or more (typical widths vary between 1 - 50 μs) will be applied to achieve a 90° rotation of magnetic moments for detection of precession due to ^{1}H atoms. The pulse width scales inversely with the strength of the pulsed field.

Figure 5.1: System blocks for the designed pulsed field generator

$$t_{90^\circ} = \frac{\phi}{\gamma B_1} \tag{5.2}$$

Here, t_{90°, corresponds to the time required for a 90° rotation (pulse width), ϕ corresponds to the rotation angle, γ is the gyromagnetic ratio which depends on the nuclei and B_1 is the strength of the pulsed magnetic field.

5.1.2 Design approach

The design of the pulsed magnetic field generator incorporates devices which can sustain high switching rates over a specific pulse duration. Switching devices such as transistors and FETs can be easily used to achieve rapid switching [109, 110] over particular time duration. However, to achieve high current, different current amplification methods must be incorporated. While our prior work [100] demonstrated the feasibility of sustaining a pulsed sinusoidal signal through an inductive load, the required current levels at higher frequencies weren't achieved due to inefficient biasing and impedance loading of the switching device. Thus, in the present work, a circuit with an improved current amplification mechanism along with reduced impedance loading effects is demonstrated.

5.2 Circuit design and pulse parameters

The designed circuit includes several stages enlisted in Fig. 5.1: signal generation, pulse shaping, voltage amplification and current generation. The corresponding circuit design is depicted in Fig. 5.2. Below, a short description of each stage and its role in the circuit operation is discussed.

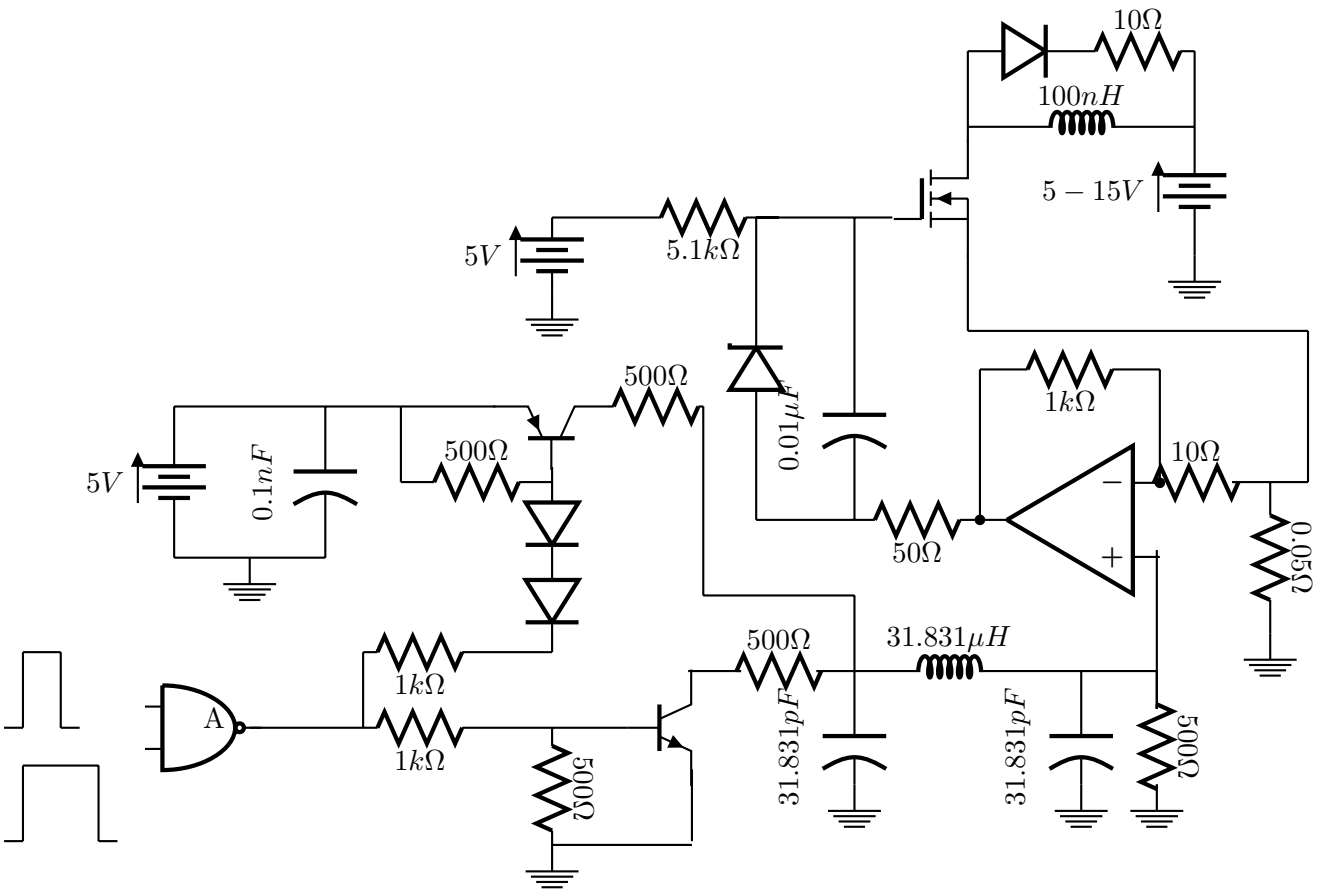

Figure 5.2: Schematic of designed circuit with different design blocks: signal generation, pulse shaping, amplification and switching

5.2.1 Signal generation

The first stage is a digital signal combiner. Two square pulses with pulse parameters 0.5 MHz, 5 V and 50 kHz, 5 V are combined using a NAND logic gate. The signal frequencies are selected such that one frequency corresponds to the Larmor precession frequency of ^{1}H and the other frequency relates to the pulse width that would be sufficient for temporary reorientation of magnetic moments. Since the bias static field may vary between 0.01 T - 0.4 T, the required pulsed field would vary correspondingly and the exact pulse width can be determined using equation 5.2. Thus, based on the equation, the pulse width of 50 kHz can be easily tuned. In general this pulse width is expected

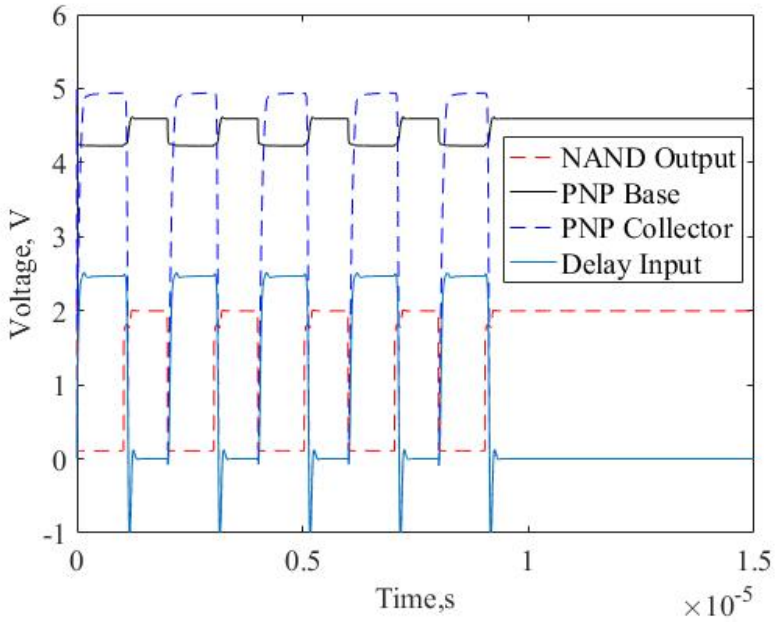

Figure 5.3: Simulated signals for the input stage at 0.5 MHz. Here a feedback resistor of 300 Ω was used between the base and emitter terminal of the PNP transistor.

to cause a temporary 90° or 180° rotation in the orientation of the magnetic moments. In contrast to the prior design's use of AND gate, a NAND gate ensures minimal signal distortion and rapid switching of the input pulses.

5.2.2 Pulse control and shaping

The modulated square pulse, as seen in Fig. 5.3, is applied to a set of transistors. Both the input transistors are biased to operate as switches. When the signal is low, the PNP transistor is active (the base-emitter junction is forward biased and the base-collector junction is reverse biased) and the signal will propagate on to the delay line. Meanwhile, the NPN transistor will be activated when the signal at the base terminal is high and any residual signal from the collector would be passed to ground. Such an arrangement is used to ensure that no signal ringing occurs during switching.

The delay line serves the function of pulse shaping the modulated signal. The signal is shaped to a sinusoidal by adequate control of the rise and fall time of the signal. In this stage the signal shape and characteristics are defined. Table 5.1 summarizes the delay line parameters for a resonant frequency, f = 0.5 MHz and correspondingly, $\omega = \frac{1}{\sqrt{LC}} = 2\pi f$ is used to estimate the values for L and C. Further scaling of delay line parameters for use at different frequencies can be done

Table 5.1: Electromagnetic Delay Line Parameters designed for a frequency of 0.5 MHz.

Parameter	50 Ω Model	Scaled Model
$\mathbf{R} = \frac{1}{2}\sqrt{\frac{L}{C}}$	50 Ω	500 Ω
$\mathbf{L} = 4R^2C$	31.8 μH	318.31 μH
$\mathbf{C} = \frac{1}{2R\omega}$	3.18 nF	0.318 nF

accordingly. A summary of the required components is in Table. 5.2.

Table 5.2: Electromagnetic Delay Line Parameters for various operational frequencies

Frequency (MHz)	R(Ω)	L(μH)	C (nF)
0.5	500	318.31	0.318
1	500	159.15	0.159
2	500	0.795	0.0795
5	500	31.8	0.0318

5.2.3 Voltage amplification

In contrast to the prior design described in chapter 4, isolation between the switching FET and delay line was incorporated using an operational amplifier (opamp). The opamp was used to minimize loading effects between the two stages. For an operational amplifier, the input impedance experienced by the opamp doesn't affect its output characteristics. Thus, the output of the opamp is stable and unaffected by the input or the attached load. Besides eliminating the loading effects, the opamp also amplifies the output voltage which is used to bias the switching FET into the saturation region. Multiple feedback paths are used to obtain stable operations from the opamp

and the details are discussed in section 5.4. In this initial iteration operational amplifier, LM 6152, was selected since its high gain bandwidth of 75 MHz would allow us to obtain pulses upto 10 MHz.

5.2.4 Current generation

The final stage of the designed circuit incorporates the output switching device, the inductive load and the capacitive bank. As soon as the gate of the switching FET is enabled, the energy stored in the input capacitor bank is immediately discharged through the inductive coil. Once the gate is disabled, the energy of the inductor dissipates through the parallel resistive load. Switching FET, part no. DMTH10H010LCT, was selected as the switching device due to its characteristic high pulsed current (92 A) and rapid rise and fall time (nanoseconds).

5.3 Experimental measurements at 0.5 MHz

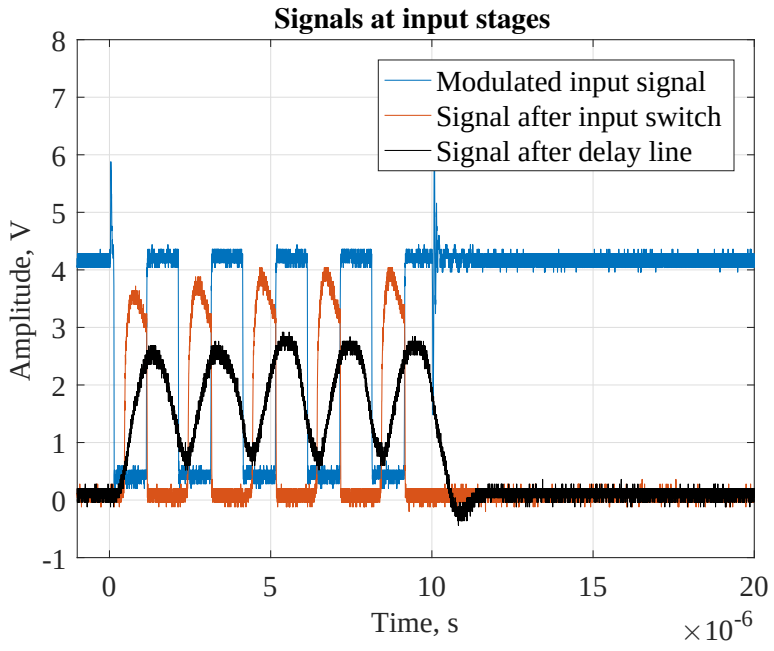

Figure 5.4: Signals measured after NAND gate and at input and output of delay line tuned to operate at 0.5 MHz. The input signal is measured at the collector of the NPN transistor

Several tests were performed on the prototype circuit. The signals measured at different stages within the circuit were recorded. Realistically, the design of the delay line may be modified to support various operational frequencies. In the first design iteration, 0.5 MHz was selected as the frequency of operation. From equation 5.1 it is well known that the NMR signal measured will be directly proportional to the precession frequency, thus, a higher precession frequency would in general correspond to a higher NMR signal and better signal to noise ratio. Once successful operations are obtained at 0.5 MHz, the circuit will be scaled for operations in a static field of 0.1 T and in a frequency range of 5 - 10 MHz.

Fig. 5.4 shows the modulated signal output at the NAND gate and the signals at the two ends of the delay line. Since the signal transmission occurs when the PNP transistor is active, there is a phase offset between the output of the NAND gate and the signal applied to the delay line. A further phase shift is introduced due to the delay line. At the same time the rise and fall time of the pulsed signal increases as it passes through the delay line.

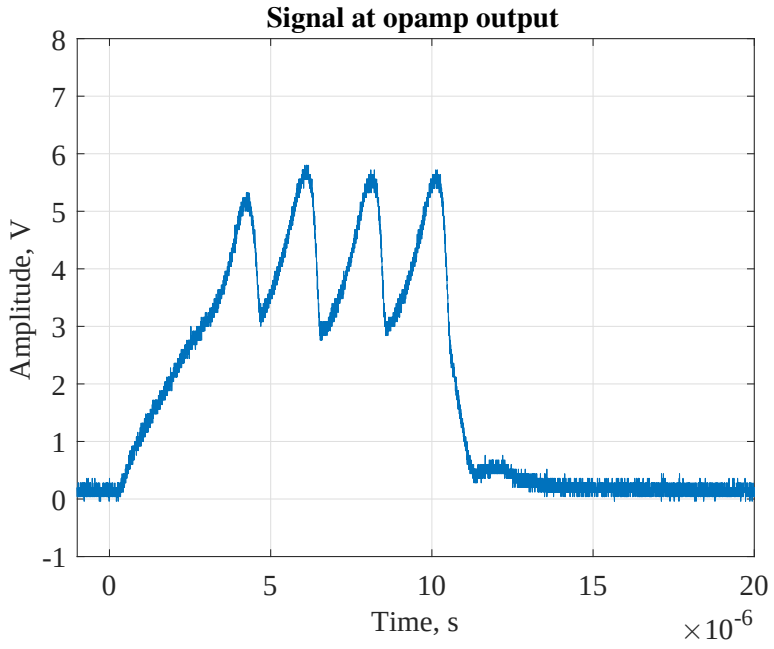

Figure 5.5: Signal variations at opamp output with variations in drain voltage

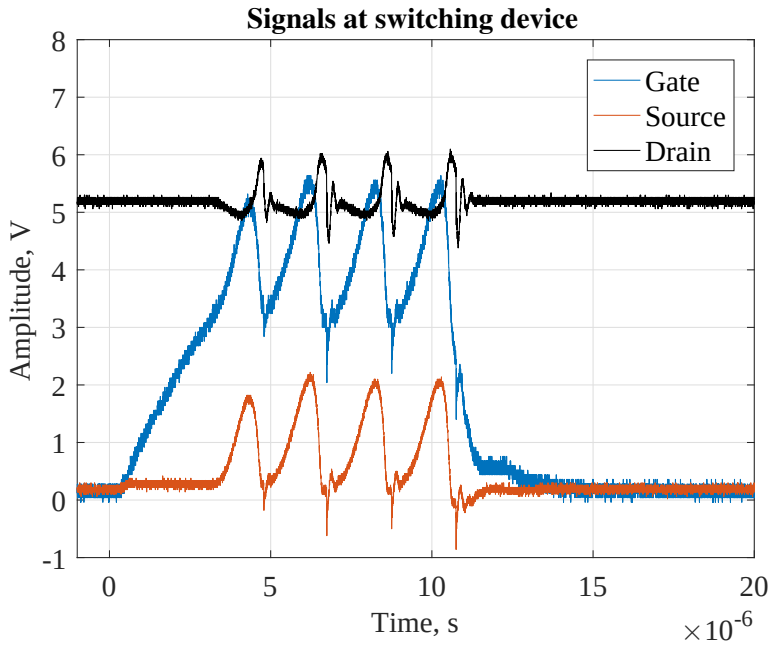

Figure 5.6: Waveform measured at the inductive load on application of a 5V signal at the drain

The next stage involves the operational amplifier (opamp). The opamp amplifies the signal at the output of the delay line and applies it to the gate terminal of the switching FET. From Fig. 5.5, there are two main findings. Firstly, the oscillation cycles at the operational amplifier's output have a slight DC offset (due to the amplification) and secondly, the number of oscillation cycles are fewer than at the input. Experimental measurements have shown that the gate capacitance of the switching FET requires about 2-3 μs to charge. Correspondingly, it was expected that the first oscillation cycle was completely used for charging the gate capacitance at the FET and then the rest of the pulsed signal appears at the load. Besides this, the gain and the design of the opamp's feedback loop are important contributing factors towards suitable biasing and stable operation of the switching FET. For improved operations, different switching FET's with lower gate capacitance or efficient gate drivers might be selected. At the same time, the bias conditions of the FET should be such that it operates as a switch and causes minimal loading at the opamp's output. In this design, a 2.7 V zener diode was connected at the opamp output to provide certain amount of pre-

biasing voltage to the switching FET's gate and thus ensure rapid turn on time for the switching FET.

For the FET to operate as a switch, we require sufficient gate and drain voltage ensuring that it is biased into the saturation region. Consequently, the use of the opamp at the input of the switching device is vital to ensure that the impedance of the delay line doesn't affect the bias state of the switching FET. From Fig. 5.5, it was observed that a major consideration for FET operation would be the stable operation of the opamp. Incorrect biasing of the switching FET could lead to severe loading effects and unstable oscillations at the output of the opamp. This implied that a careful design of the feedback loop was required to ensure that pulsed sinusoidals may be obtained at the output.

An inductive load of approximately 0.1 μH was connected to the drain terminal. The output corresponding to a 5 V bias signal can be observed in Fig. 5.6. Here it is observed that the pulsed variations appear with a DC offset equivalent to the voltage applied at the drain terminal. However, the rate of change of voltage with time or repetition frequency is too fast to obtain a voltage swing from 5 V to 0 V. This observation implies that further modifications to the bias condition of the FET are needed to improve its operations as a switch. The drain and source voltage follow the modulation at the gate. A resistor and diode are connected in parallel across the inductive load for a discharge path once the switching FET is turned off. This combination also curbs spurious ringing. A current sense resistor of 10 Ω was connected at the source terminal to estimate the current through the inductor.

5.4 Modifications to the operational amplifier

The selection of the opamp plays an important role in the stability of the switching FET. The opamp also determines the maximum frequency and switching rate for the signal applied to the gate. This is because the gain bandwidth product of the opamp limits the maximum operational frequency while the slew rate determines the rate of switching.

5.4.1 Simulations with various opamps

In the first iteration, an opamp with a gain bandwidth product of 75 MHz and a slew rate of 5 - 45 V/μs was selected. This selection limited the operational frequency of the device to a maximum of 0.7 MHz for an opamp output voltage of 10 V. Non-linear distortions would occur if the opamp was operated beyond its designated operational range due to slew-rate limiting. This is observed via simulations in Fig. 5.7.

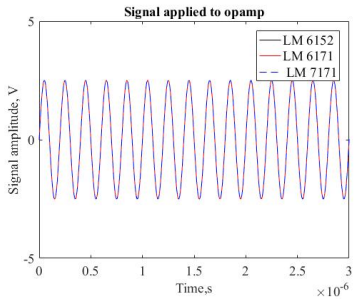

(a) Opamp Input

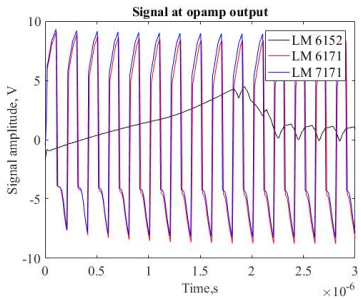

(b) Opamp Output

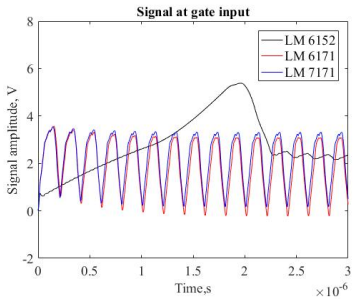

(c) Gate Input

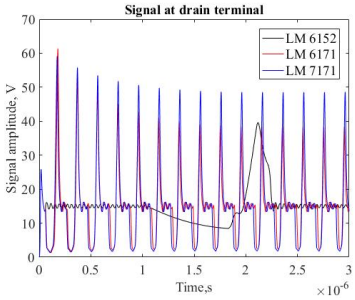

(d) Drain Terminal

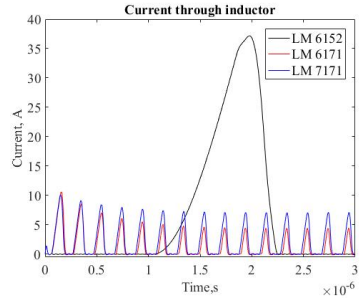

(e) Inductor current

Figure 5.7: Simulated signals for opamps with different slew rates

A 5 MHz, 2.5 V sinusoidal signal, as observed in Fig. 5.7a, was applied to the non-inverting terminal of the operational amplifier. The applied signal was amplified and further applied to the gate terminal of the switching FET. As observed in Fig. 5.7b, LM 6152 is unable to respond at a frequency of 5 MHz. While the response of the other two opamps (LM 6171 and LM 7171) displays sharp rise and fall times, neither of them are affected as drastically as the opamp, LM 6152. Since

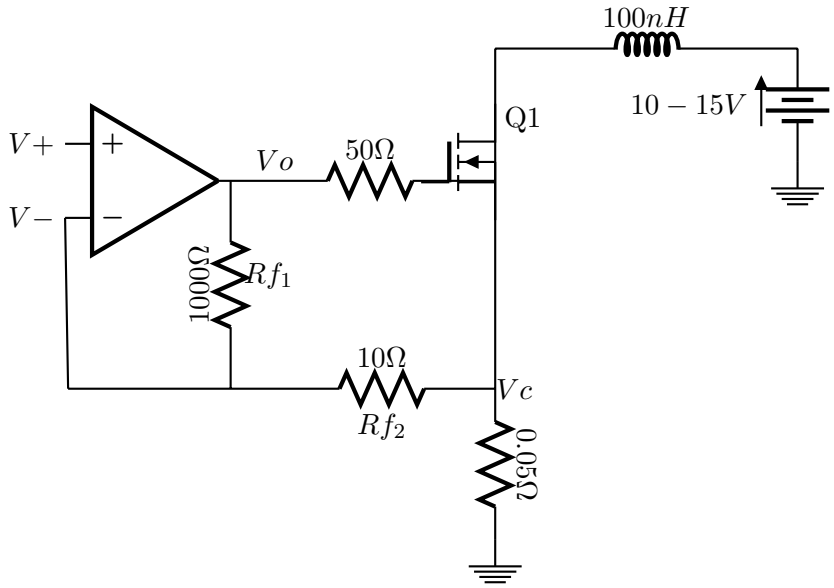

Figure 5.8: Schematic of opamp loop

the gate voltage, Fig. 5.7c, is higher than the threshold voltage for the switching FET, the FET is in saturation and current flows through the inductor. While high currents can be obtained using LM6152, Fig. 5.7e, repetitive and continuous current can be obtained using LM6171 and LM 7171 respectively. It must be noted that simulations were performed with a continuous sinusoidal waveform instead of a pulsed sinusoidal input at the opamp's input due to software limitations. Based on these simulation results, experiments were performed using LM 7171 and the results are reported in section 5.5.

5.4.2 Stability of opamp

Since the opamp is responsible for appropriate bias of the FET and maintaining the overall stability of the output signal, it is necessary to understand its operation. As seen in Fig. 5.8, the voltage at the opamp output should be sufficient to overcome the gate threshold voltage and drive the FET into saturation.

Here, V_- is the voltage at the inverting terminal, V_+ is the voltage at the non-inverting terminal, V_0 is the voltage at the opamp output, V_c is the voltage drop across the current sense resistor, V_{gs} is the gate to source voltage, R_{f1}, R_{f2} are the feedback resistors. Using node voltage at node V_-,

$$\frac{V_0 - V_-}{R_{f1}} = \frac{V_- - V_c}{R_{f2}} \tag{5.3}$$

$$V_0 = V_- + \frac{R_{f1}}{R_{f2}}(V_- - V_c) \tag{5.4}$$

$$V_0 = V_-\left(1 + \frac{R_{f1}}{R_{f2}}\right) - V_c\left(\frac{R_{f1}}{R_{f2}}\right) \tag{5.5}$$

Assuming that the FET is biased into saturation, the drain current would be equal to the source current. Then, assuming that almost all the source current flows into the current sense resistor, R_c, and hardly any current flows into R_{f2}, at node V_c, thus,

$$V_c = I_{ds}R_c \tag{5.6}$$

The drain current can be approximated to be

$$I_D = g_m(V_{gs} - V_t) \tag{5.7}$$

where, g_m, is the transconductance parameter, V_{gs} is the gate to source voltage and V_t is the threshold voltage. From the datasheet, g_m was estimated to be equal to 30 and the threshold voltage was 3 V. Therefore,

$$V_c = 30(V_{gs} - 3)R_c \tag{5.8}$$

Assuming the voltage drop across the 50 Ω resistor to be negligible, equation 5.8, can be written as

$$V_c = 30(V_0 - V_c - 3)R_c \tag{5.9}$$

After simplification,

$$V_0 = 3 + \frac{V_c(1 + 30R_c)}{30R_c} \tag{5.10}$$

Substituting equation 5.10 into equation 5.5, we obtain,

$$V_-\left(1 + \frac{R_{f1}}{R_{f2}}\right) = 3 + V_c\left(\frac{1 + 30R_c}{30R_c} + \frac{R_{f2}}{R_{f1}}\right) \tag{5.11}$$

Substituting values in equation 5.11 and after further simplifications,

$$V_0 = 1.65V_- + 2.95 \tag{5.12}$$

While the opamp tries to minimize the voltage difference between the non-inverting and inverting terminal, equation 5.12 is written as

$$V_0 = 1.65V_+ + 2.95 \tag{5.13}$$

In summary, the presence of multiple feedback paths controls the maximum output voltage at the opamp and prevents the opamp from being an unstable oscillator. For experimental measurements, the phase of V_+ or the input signal, needs to be set to -90° to ensure the opamp's stability of operation.

5.4.3 Measurements for opamp loop

To ensure stability of the opamp loop, measurements were performed for the opamp and the switching device. An input pulsed sinusoidal signal, with an amplitude of 2.5 V was applied to the non-inverting terminal of the operational amplifier. The output stage of the opamp was connected to a 50 Ω resistor which was further connected to a 2.7 V zener diode ensuring approximately 2.7 V pre-bias voltage at the gate of the switching FET for rapid start of the switching FET. A 100 nH planar inductor was connected to the drain terminal which was held at a bias voltage of 10 V. A 1 Ω current sense resistor was used instead of the 0.05 Ω resistor shown in Fig. 5.2.

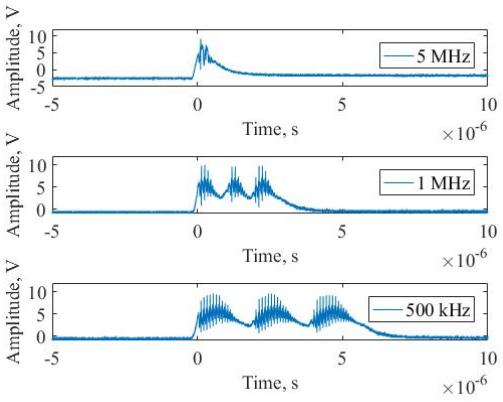

(a) Gate

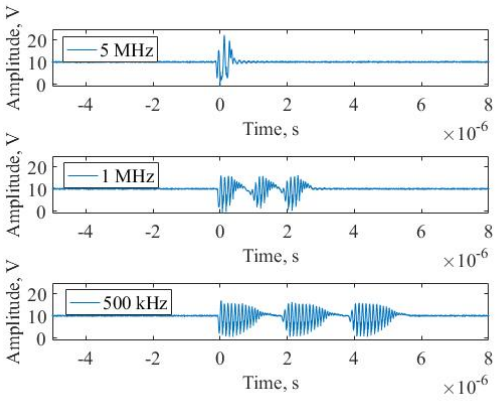

(b) Drain

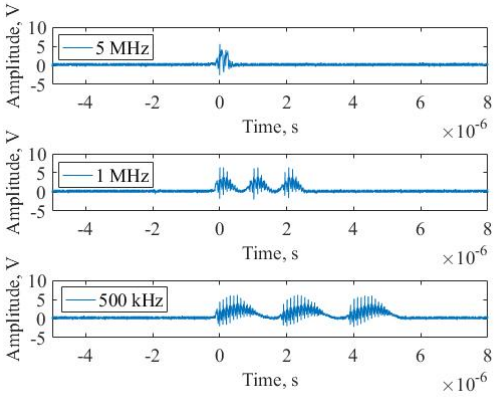

(c) Source

Figure 5.9: Voltage measured at different terminals of the switching FET for different operational frequencies

Fig. 5.9 includes representations of the voltage at the gate, drain and source at frequencies of 500 kHz, 1 MHz and 5 MHz respectively. While a certain amount of signal ringing exists at each of these frequencies, it is observed that at lower frequencies, ringing persists. Based on these observations, a 33 V zener diode was added to the inductor's feedback path to obtain rapid ringing decay.

5.5 Experimental results at an operational frequency of 5 MHz

The designed circuit as seen in Fig. 5.10, was tested in different stages. The response of the input circuit was tested at various operational frequencies similar to the opamp loop described in section 5.8. The current through the inductor obtained on combining all the design stages can be observed in Fig. 5.11. It is observed that the ringing in the current is much lower than the voltage ringing observed for the switching FET as seen in Fig. 5.9. Once the gate terminal of the switching device is active, based on the selected current sense resistor and the applied drain voltage, the current through the inductor can be tuned further. Therefore, in Fig. 5.11, the units for current are arbitrary. In summary, assuming the inductor as a solenoid with 10 turns, length of 0.01 m and a current of 10 A, B_1 of 0.01 T can be obtained.

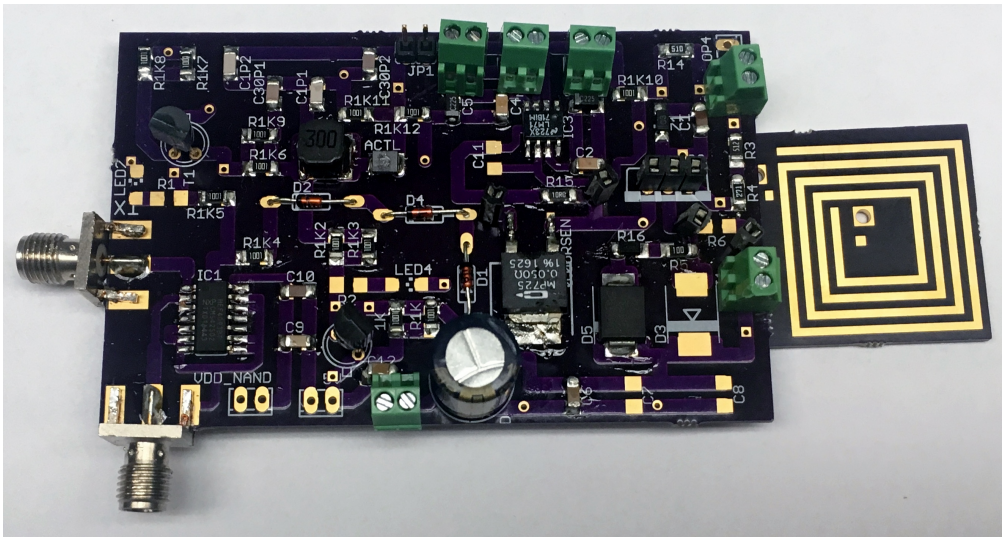

Figure 5.10: Designed prototype circuit board

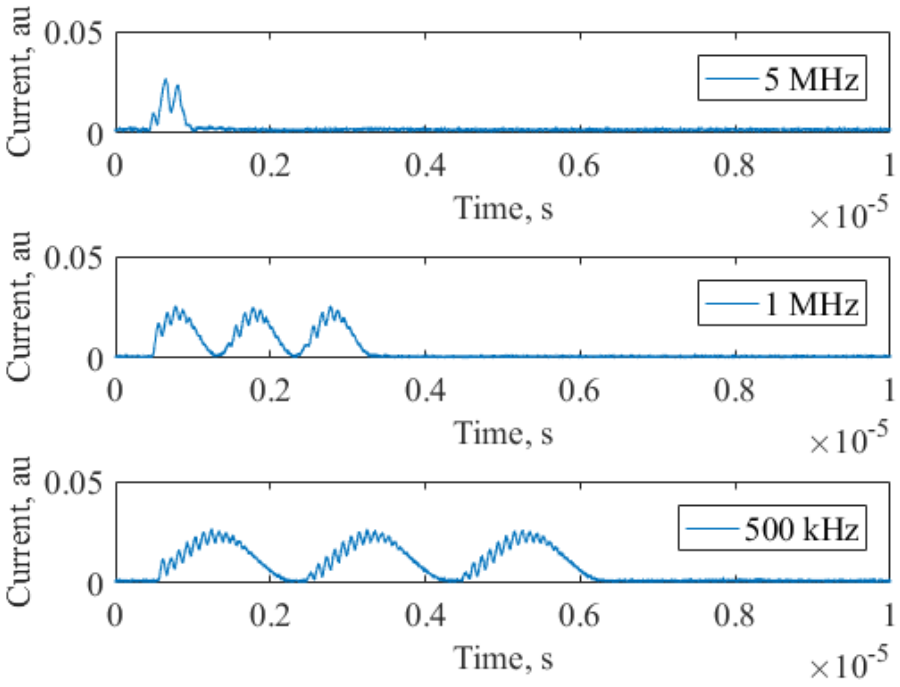

Figure 5.11: Current measured through the load, reported in arbitrary units

5.6 Conclusions

Through this work the design, development and operation of a pulsed magnetic field generator using a fast switching FET were observed. The design process reveals that the feedback loop of the opamp needs to be tuned to ensure required pulsed currents. At present, the opamp loop is tuned to a small gain and a small capacitive bank (100 μF) is used at the drain. Approximately 0.5A of current is flowing through the 10 Ω current sense resistor at an operational frequency of 0.5 MHz. At 5 MHz, approximately 10A of current can flow through a 100 nH inductor with appropriate tuning of drain voltage and current sense resistor. However, higher currents might be achieved by reducing the value of the current sense resistor and applying a higher drain voltage. By using the designed circuit and careful control of the feedback system a stable pulsed field can be generated in contrast to the prior FET based field generator [100]. Potential non-linearity may be introduced

due to the slew rate, gain bandwidth and loading of the operational amplifier. These non-linearities can affect the operation of the pulsed sinusoidal and thus the bias-conditions of the switching FET and impedance loading effects of the opamp need to be closely examined in future magnetic field generators.

5.7 Avenues for improvement

The improved pulsed field generator successfully eliminates the loading effect between the switching stage and the delay line. However, other attributes such as gate capacitance of the switching FET, higher switching frequency, opamp stability and obtaining biphasic pulsed fields need to be considered. Modifications to the existing monophasic field generator and an alternative design for biphasic operations is discussed in the following section.

In summary, the designed pulsed field generator can be used to create pulsed currents and correspondingly pulsed magnetic fields. While these parameters are sufficient for the application of low-field unilateral NMR, further investigations on the effect of the inductive load on the pulsed signal shape and recovery would lead to improvements in the design of the inductive load. In turn, these would make the circuit design applicable to a wider number of pulsed systems. In particular, the coil design could be improved to incorporate transmission to larger distances and simultaneous transmit/receive capabilities. In addition, better mechanisms need to be developed to ensure proper bias conditions for the switching FET and to minimize the loading effects at the output of the operational amplifier.

5.8 Towards a biphasic field generator

Biphasic field generators surpass monophasic field generators in terms of maximum achievable magnetic resonance signals. This is because biphasic field's can initiate NMR spin transitions for magnetic moments which are aligned or unaligned with the applied magnetic field, thereby leading to twice the amount of NMR signal expected using a monophasic field generator. The design of the proposed biphasic field generator is comparable to the monophasic field generator described in this

chapter. An additional switching device is included to obtain operations during the negative half of the pulsed sinusoidal. The two switches can be connected to a set of intertwined inductors with only one inductor activated at a particular point of time. Biphasic operations may also be obtained by using two identical switching devices with coils wound in opposite directions. However, this design presented several challenges in early tests and iterations and wasn't pursued further. The biphasic generator described in this work is simulated to obtain a maximum of +/- 50 A through the inductor at operational frequencies upto 3 MHz.

5.8.1 Proposed designs

As described in the previous section, the design of a biphasic field generator involved inclusion of an additional switching device which could respond to the negative half of the sinusoidal signal. A pulsed sinusoidal input, as described in prior work [111], was used at the input of an operational amplifier. Two different switching configurations were simulated. In configuration A (Biphasic A) , Fig. 5.12, a common pulse forming network was used to apply a sinusoidal signal at the gate of a n-type (Q1) and a p-type (Q2) switching device. In configuration B (Biphasic B), Fig. 5.13, two different pulse forming networks with phase offsets were utilized alongside the switching devices. A pre-bias voltage was applied at the gate terminal of each switching device to pre-charge the input gate capacitance for each switching device. In each configuration, the inductors were intertwined and a shunt diode and resistor were used to dampen ringing once the gate signal was turned off.

5.9 Simulation results and discussion

Fig. 5.14 and Fig. 5.15a represent the current through the inductor for configurations A and B respectively. The two configurations produce comparable currents. An initial overshoot occurs in the current produced by the n-type device due to the pre-biasing circuit used at the switching device. The exact opposite effect is observed at the p-type device with minimal current during the first cycle. After the initial overshoot, the positive current stabilizes at approximately 40 A while the

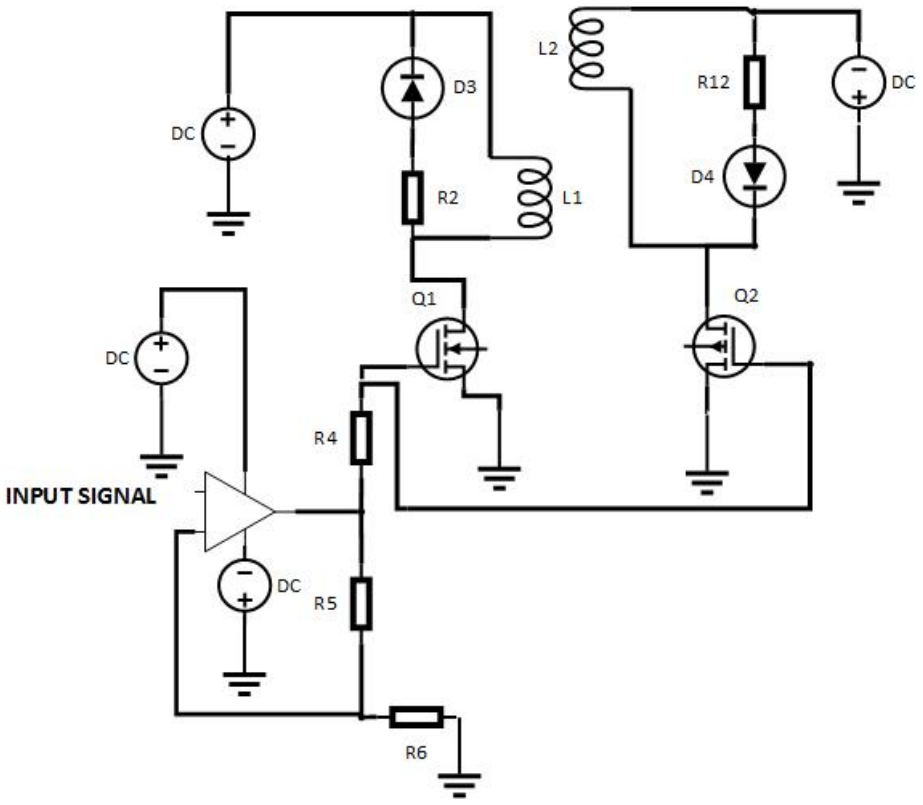

Figure 5.12: Biphasic field generator: Configuration A

negative current stabilizes at approximately 52 A. Between the two configurations, in configuration B, the peak current for the positive and negative half cycle are comparable (approximately 40 A).

The rise and fall time of the switching device also impact the operations in both the configurations. The effect of rise and fall time is apparent for configuration B once the operational frequency is increased to 2 MHz as seen in Fig. 5.15b. Here, it is observed that with an increase in operational frequency the maximum pulsed current obtained reduces. Moreover, due to the variable rise and fall times for two switching devices, there is a period of overlap when both the waveforms overlap. With a further increase in operational frequency, the overlap becomes more prominent. Thus, the phase offset needs to be controlled diligently in configuration B. Additionally, the initial oscillation cycle isn't obtained for the p-type device due to delayed activation of the gate terminal. Meanwhile, for configuration A with an increase in operational frequency, once the two signals overlap, both

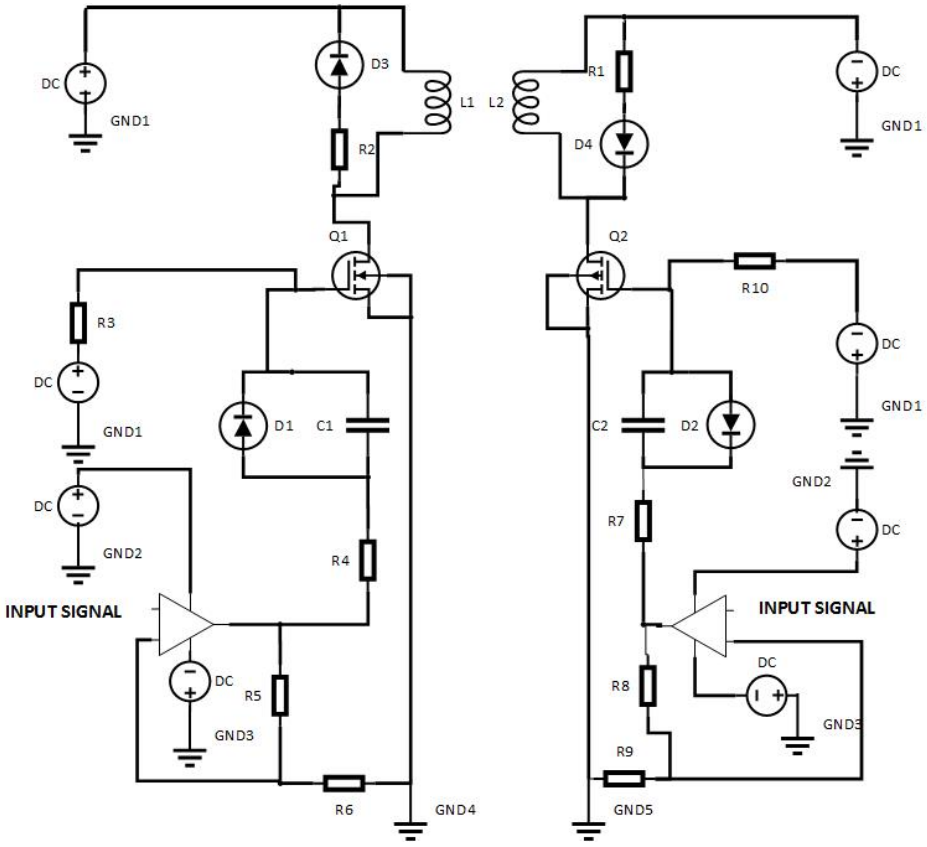

Figure 5.13: Biphasic field generator: Configuration B

the inductive coils would be activated and the net magnetic field would be reduced. Therefore, configuration B with suitable phase control is preferred for operations at higher frequencies.

Lastly, in both monophasic and biphasic configurations it is observed that with an increase in operational frequency, the peak current decreases. In order to obtain high current at high frequencies, switching devices with faster rise and fall times need to be selected. Alternatively, the duty cycle of each pulse needs to be reduced to obtain higher currents for shorter intervals.

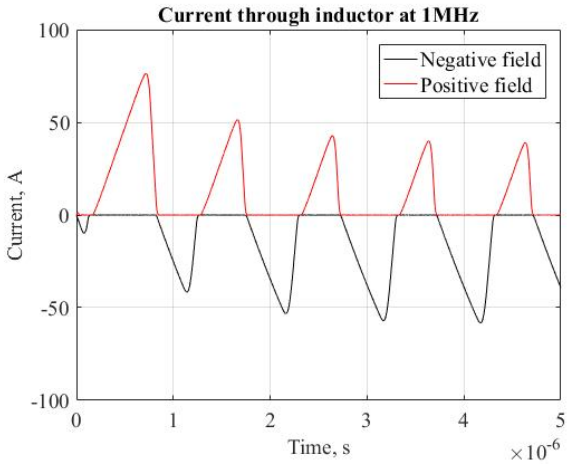

Figure 5.14: Current through inductors in configuration A at a frequency of 1 MHz

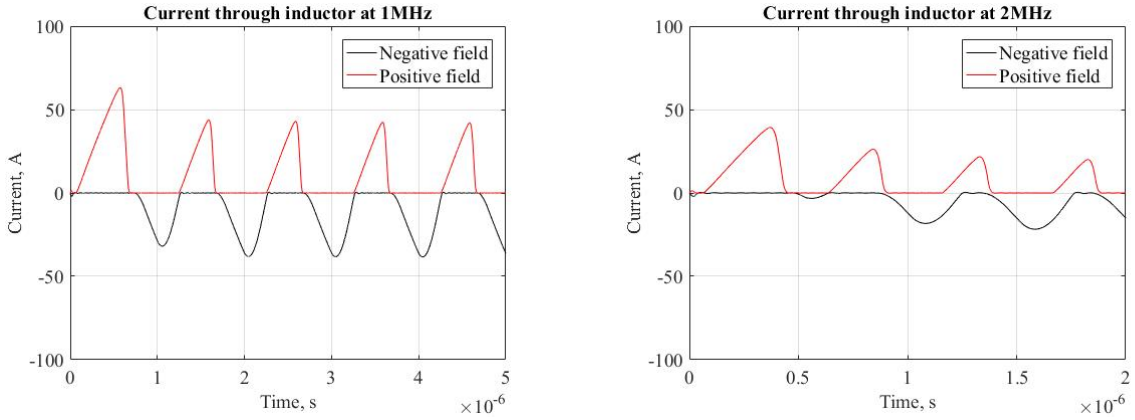

(a) 1 MHz

(b) 2 MHz

Figure 5.15: Current through inductors in configuration B at a frequency of 1 MHz and 2 MHz respectively

5.10 Comparisons between different field generators

The main parameters that are considered in the design of both the monophasic and biphasic pulsed field generators are summarized in Table. 5.3. The extension of the design from monphasic to biphasic involved modifications to the switching device, load and pulse forming network. As seen

in Table. 5.3, the monophasic field generator has the highest operational frequency and current. In the biphasic configurations, carefully intertwined coils, selection of fast switching devices and coordination of operational amplifiers used within the pulse forming network is required. Additionally to obtain higher currents at higher frequencies, the duty cycle of the applied input pulse needs to be controlled.

Table 5.3: Comparison of parameters significant for design of monophasic and biphasic field generators

Parameter	Monophasic	Biphasic A	Biphasic B
Frequency	Upto 8 MHz	Upto 3 MHz	Upto 1 MHz
Current	Upto 50 A	20 - 50 A	Upto 40 A
Coil Arrangement	Single	Intertwined	Intertwined
Feedback Loop	Present	Present	Absent
Drain voltage	15V	15V	15V
Input Sinusoidal	2.5V	2.5V	2.5V
Phase Offset	Not Applicable	Necessary	Not Applicable

5.11 Summary

The development from a monophasic to biphasic field generator requires several design modifications to the pulse forming network, switching device and load. Modifications at each stage were examined and changes were implemented for the switching device to extend the monophasic operations for biphasic field generators. The present design iteration revealed that while monophasic field generators could operate at higher frequencies (upto 8 MHz), biphasic field generators which shared the pulse forming network were unable to operate at frequencies above 2 MHz. Moreover, the rise and fall time of the switching devices would significantly affect the biphasic system performance at higher frequencies. In summary, different aspects of the switching device, load and operational frequency need to be considered to obtain stable biphasic pulsed magnetic fields.

5.12 Future work

Monophasic and biphasic field generators both find their place and utility in different magnetic resonance applications. A significant challenge identified through this work is the difference in the rise and fall-time characteristic of the different switching devices. While this is expected, in the case utilizing two different pulse amplification stages, coordinating the triggering between the two switching devices is a challenge. A few possible ways of overcoming this challenge may be use of similar switching devices with different load configurations or isolated pulse switching stages triggered on or after the signals have completely decayed. Operations at higher frequencies also remains a challenge that requires further work in design of the pulse generation and switching mechanism.

CHAPTER 6. STUDIES AND MEASUREMENTS ON FERROMAGNETIC MATERIALS

Materials placed in a combination of a static and a pulsed magnetic field can produce various signals. As described in chapter 3, when static fields pass through ferromagnetic materials the spatial distribution of magnetic flux is concentrated within the material. This observation suggests that when pulsed fields are applied to ferromagnets placed in static fields, the response from the material's state of magnetization will be captured in the recorded signals.

In this chapter, signals obtained from ferromagnetic materials placed in the presence of a cuboidal permanent magnet and pulsed with a Magritek Kea system are studied. Measurement results show that the variation in bulk magnetization of the ferromagnetic materials, affects the state of magnetization and the corresponding signal response. Here, signals from inductive sensors comprising of ferromagnetic cores, used for oil well logging are examined. These signals are often described as ringing since they interfere with the intended measurements. Since ferromagnetic cores are typically used to enhance signals received from external media in unilateral NMR applications, a study of the signal response from such magnetic cores is vital.

Through this study, the interaction between the ferromagnetic material and pulsed magnetic field is studied. The effects of varying magnetization are highlighted. Based on the magnetic core's geometry and dimensions, effects due to non-linear magnetization may be mitigated. This chapter also demonstrates and discusses ways of controlling ringing by considering interrelationships between different factors such as inductance, magnetic permeability and quality factor.

6.1 Introduction

The phenomenon of nuclear magnetic resonance (NMR) is widely used to study different materials through NMR spectroscopy. Magnetic inductive sensors are being used for generation and/or

detection of magnetic fields in varied applications inclusive of magnetic resonance imaging, nondestructive evaluation, proximity detection etc. Inductive sensors used in oil well logging instruments can detect the presence of oil/water in earth formations using NMR. NMR measurements are thus an important part of oil well logging and are used to identify and quantify oil and gas reservoirs. For these measurements an 'inside-out' approach is employed [67]. NMR well logging uses the NMR response of an earth formation to determine its porosity and permeability. A continuous record is obtained along the length of a borehole in operation. The inductive sensor used for this application, acts as both a signal transmitter and receiver and at the same time contributes its own intrinsic signal to each measurement. Often, this contribution can mask the actual measured signal. For such applications it is thus vital to determine the signals contributed from the inductive sensor.

The NMR equipment used for oil well logging comprises of a large static magnetic fields, generally produced by permanent magnets, and a high frequency oscillatory magnetic field projecting outwards from the core of the test apparatus. The two magnetic fields, interact with the surrounding media and the received signal is then studied to determine the porosity and hydraulic permeability of the media. Unlike conventional NMR systems, inside-out NMR measurements are conducted at resonant frequencies below 2 MHz [112]. The weak nature of the static magnetic fields employed [67] makes it difficult to observe the chemical shifts and hence most of the signal information is obtained from the relaxation data or the free induction decay (FID) signal. Oil well NMR tools are also used to conduct NMR measurements within the ground and the received signals can be analyzed in-situ or once the tool is brought to the surface. Thus, these tools require the lowest FID time to maximize the number of measurements and attain a higher signal to noise ratio (SNR).

6.1.1 Relevance to oil well logging applications

In particular, the focus of this chapter is on inductive sensors utilized for 'inside-out'[113] nuclear magnetic resonance (NMR) applications such as oil well logging. The inductive sensor used for this application is a combination of a magnetic core and an inductive coil placed in an external static

magnetic field. In particular the magnetic core enables generation of a higher magnetic flux within and in the surrounding media thereby allowing for improvements in measured signal to noise ratio (SNR).

In oil well logging applications as discussed before, the inductive sensor plays a dual role, acting as a transmitter for the excitation signal and also as a receiver for the response from the surroundings. The transmitter frequency is selected as the precession frequency of the material under test such that all the magnetic moments in the area surrounding the sensor oscillate at the applied frequency. Once the signal is switched off, the magnetic moments revert back to their original direction of magnetization. It is essential that the signal (termed as free inductive decay (FID)) generated when the magnetic moments are returning to their original magnetized state is accurately captured by the inductive sensor. This is because unlike conventional NMR systems, "inside-out" NMR measurements are conducted at resonant frequencies below 2 MHz, under low static magnetic fields [112, 113]. Instead, inside-out NMR systems acquire multiple samples and the measured signals are ensemble averaged to obtain a good estimate of the FID. Multiple acquisitions also facilitate improvements in SNR.

6.1.2 Limitations to oil well logging measurements

It is well understood that besides the surrounding media, the magnetic core material used within the inductive sensor is also magnetized and reverts to its original state of magnetization once the magnetization pulse is removed. It is observed that under most circumstances the signal generated by the magnetic core overlaps with the signal received from the surrounding media and this is detrimental in conducting rapid/multiple measurements [114]. It is thus required to minimize the interference (ringing) [70, 115, 116] generated due to the magnetic core in order to significantly reduce the dead time of the receiver [117, 118] in typical oil well logging applications.

Previous work [119, 120, 121, 122, 123, 124, 125, 126, 127] like using a Q switch, transformer-coupled matching networks, snubber circuits highlights several techniques that have been employed to mask the inductive sensor signal. However, masking the signal still doesn't allow the user to

conduct rapid/multiple measurements and thus several considerations need to be made to achieve minimization of the FID signal. Firstly, the magnetic energy within the magnetic core material must be quickly dissipated or absorbed in order to minimize the contribution of the core to the response signal. At the same time, the inductive sensor should have a high sensitivity to the signals received from the surrounding media and the response of the sensing coil must be selective. A combination of these two factors can lead to improved NMR measurements in oil well logging applications.

6.1.3 Ringing effects and FID

RF pulses are repeatedly applied to the test sample and the signal received during this time is know as the Free-Induction Decay (FID). It is found that the magnetization doesn't precess indefinitely and the spins return back to their original state after removal of the RF pulse. This phenomenon is known as relaxation. Two time constants, T_1 and T_2 are used to describe this behavior. T_1 corresponds to the gain and loss of magnetization along the direction of external magnetic field. T_2 or the damping time constant corresponds to loss of phase coherence among the nuclei or the loss of magnetization along the direction of the orthogonal RF field. Mathematically, T_2 is related to the linewidth ($\Delta\nu_{1/2}$) of the signal through the relation

$$\Delta\nu_{1/2} = \frac{1}{\pi T_2} \tag{6.1}$$

Loss of magnetization energy in the direction of the static field or along the RF field would be equivalent i.e. reduction of T_1 (or T_2) would lead to faster signal magnetization and faster signal acquisition [126].

In this study, the FID signal is characterized as ringing since the test specimen is considered to be the magnetic core within the coil. This ringing effect caused by the core and coil combination may lead to erroneous measurements due to emergence of false resonant peaks. The ringing in pulsed NMR systems can be attributed to several sources such as acoustic ringing [128], eddy current damping effects [129], magnetostriction effects [128], material related effects, and circuit

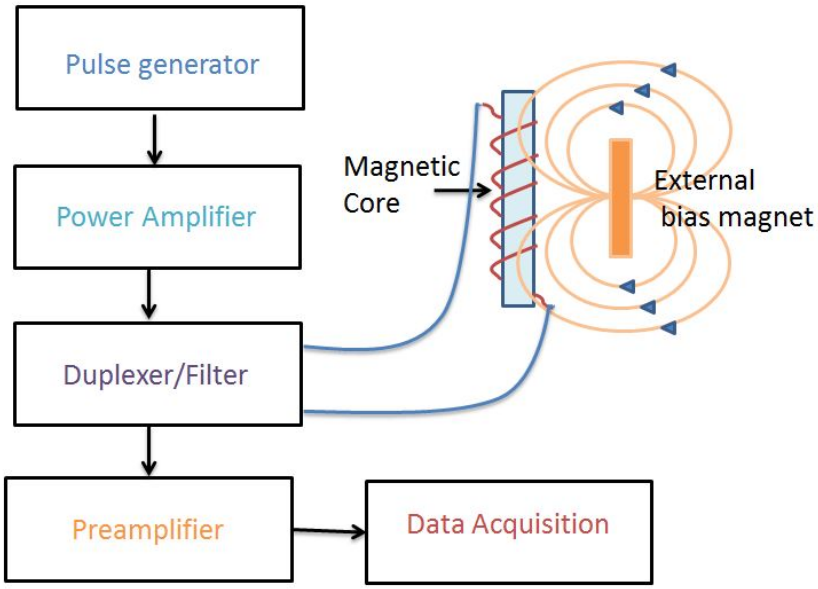

Figure 6.1: Schematic representation of measurement system. The pulsed sinusoidal is generated by the pulse generator, amplified by the power amplifier, filtered and applied to the inductive load. Signals are received at the duplexer after a 100 μs delay, amplified and processed at the data acquisition unit. The shielding box encloses the magnetic core and the external bias magnet.

and sensing system designs [126]. Isolating the contributions of the different causes is necessary to understand and systematically decrease or eliminate the detrimental effect of ringing.

6.2 Experimental Details

Measurements were conducted using commercially available magnetic core materials. Different materials with relative permeability: Mu 55, Mu 100, Mu 125, Mu 1200 were selected. The NMR measurement set-up comprises of several units: a Magritek Kea system, high-power RF amplifier, signal duplexer and an inductive antenna/coil. A system level representation can be found in Fig. 6.1.

The user enters several parameters through a menu-driven program and activates the Kea system which generates an RF pulse with a maximum output power level of 1 mW. The amplitude and phase of this signal are controlled by the inbuilt digital signal processor. The generated signal

is then sent to the high-power RF amplifier and is amplified upto a maximum power level of 4000 W and passed on to the duplexer. The duplexer serves a dual function. It allows the high-power signal to reach the antenna and blocks it from reaching the Kea system thus preserving it from any damage. A TTL signal ensures coherence between the signals from the spectrometer, amplifier and duplexer. The RF pulse is then applied to the antenna. Initially a short pulse of duration 20 μs is selected in order to obtain a larger frequency bandwidth. Once the peak signals are identified, selective pulses of approximately 200 μs are applied at those frequencies. The pulses from the receiver are acquired with a delay of 400 μs to allow the amplifier signal to switch off. The received signal is once again re-routed to the Kea system via the duplexer and a pre-amplifier. The free inductive decay signal can then be analyzed. The system-level timing is illustrated in Fig. 6.2. A permanent magnet with a field strength of 400 G is used to generate the static magnetic field.

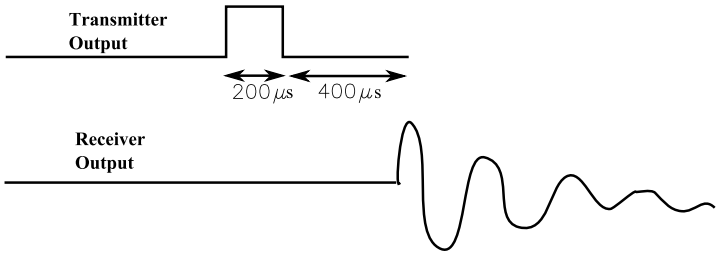

Figure 6.2: System Timing diagram. A sinusoidal pulse train is transmitted for a duration of 200 μs and the signal at the receiver is recorded 400 μs after the pulse is turned off. The received signal is described as the FID.

Since the acquired signal is weak, measurements were repeated every 500 ms in order to improve on the signal to noise ratio (SNR), and the signal was averaged over 64/128 measurements. The amplitude and position of the signal repeat while the stochastic nature of noise makes it unrepeatable at the same location after each iteration.

6.3 Responses from the magnetic core materials

The inductive core material dominates the signal response. As seen in Fig. 6.3, with an increase in the material permeability, the inductance increases. Initial measurements indicated that that higher permeability materials also resulted in higher ringing and multiple resonant frequencies.

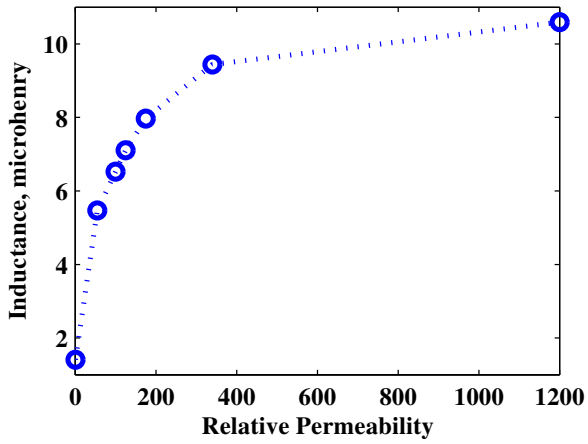

Figure 6.3: Inductance vs Permeability. Inductance was measured using an LRC meter in the 10kHz frequency range. Relative permeability was estimated from the manufacturer specifications.

6.3.1 Quantification of Ringing

The damped nature of the signal allows us to propose a figure of merit (FOM) that could be utilized to quantify the ringing. As illustrated in Fig. 6.4, the FOM can be mathematically defined as

$$FOM = \frac{V_1 - V_2}{V_0(t_1 - t_2)} \tag{6.2}$$

where V_1 is the original signal amplitude at time t_1 once the RF pulse is suspended, V_2 is the amplitude of the FID after time t_2 and V_0 is equivalent to the initial ringing amplitude. The difference between t_1 and t_2 was selected to be equal to 1 time constant though a decay by 5 time constants is a better approximation since it accounts better for complete signal decay. For this study, the proposed FOM may be used to compare the ringing from different magnetic materials.

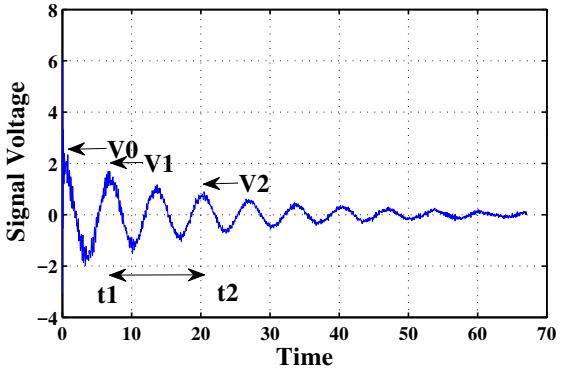

Figure 6.4: Figure of Merit. V_1 was considered to be the same as V_0. $\Delta t = t_1$ - t_2 was considered to be one time constant.

6.3.2 Effect of material on signal decay time

The pulse frequency is swept over a frequency range of 0.1 to 1.4 MHz and the corresponding resonant frequencies are recorded for each ferromagnetic material. The FID for each of these frequencies was estimated using an exponential fit. In order to observe the effect of material on the signal damping, the FID signals are compared at a frequency (f_o) of 152 kHz for all materials except Mu1200 which indicated resonance at a frequency of 140.5 kHz. This frequency may be considered an indication of the circuit resonance. A comparison of the signal decay time can be found in Fig. 6.5. The ringing signals were fitted using varied exponential functions. The decay time was computed in each case and the line width was approximated from the Fourier spectrum of the signal. The results are summarized in Table. 6.1.

Table 6.1: Comparison of magnetic materials at single frequency

Material	Initial Ringing Amplitude (| μV|)	Approx Decay Time (ms)	Approx Line Width (Hz)
Coil Only	0.57	-	346.19
Mu55	2.518	9.034	307.3
Mu100	3.95	16.9	277.6
Mu125	27.03	0.2	403
Mu1200	5048	3.278	293

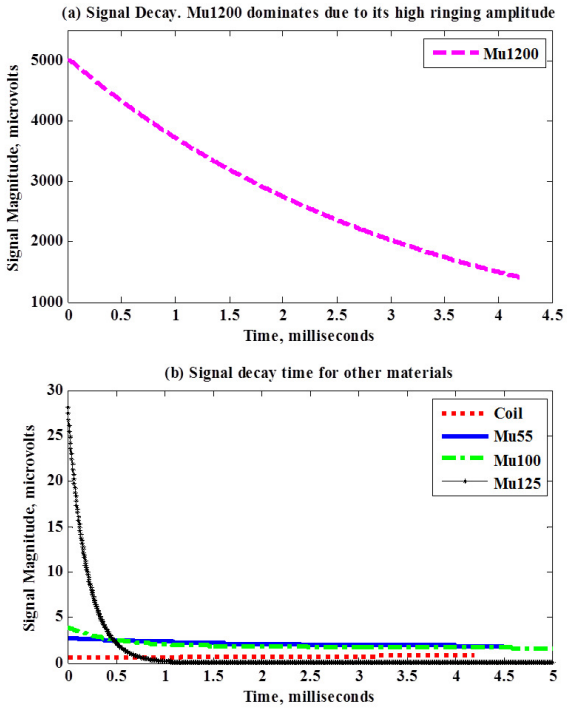

Figure 6.5: Signal decay profiles. Decay times were estimated from the exponential fits. The decay time was approximated when the signal had decayed by one time constant or 0.37 of its original value

For a typical FID signal, the initial signal amplitude may relate to the permeability of the material as seen in Fig. 6.5. This signal will completely mask the NMR signal due to high ringing amplitude. Thus, high permeability materials or impregnated materials may not be good candidates for the magnetic core in the inductive antenna. This leads to a trade-off since it is necessary to use a high permeability core material in the NMR tool to allow maximum flux penetration in the surrounding earth.

For a typical FID signal, the signal decay time also provides information about the texture and the type of fluid in an NMR application. It is observed that with a decrease in the porosity of the core material, as in the case of Mu125 (impregnated material), the ringing amplitude decreased and there was a significant reduction in the signal decay time.

6.3.3 Effect of material on Q-factor

With an increase in inductance, the quality (Q) factor directly increases. A Q factor above 0.5 corresponds to an under damped circuit oscillation. The single-sided frequency spectrum of the time-domain signals is observed in Fig. 6.6. The frequency spectrum is shifted such that the center frequency at the origin corresponds to the resonant frequency of 152 kHz and 140.5 kHz for Mu1200. The center frequency for Mu1200 is offset by approximately 0.2kHz. Materials with a greater line width indicate correspondingly wider peaks in the frequency spectrum and lower Q factors. From Table. 6.1 it was found that Mu125 has the highest line width and correspondingly lowest decay time. The FOM was found to decrease with an increase in signal decay time as observed in Table. 6.2.

Table 6.2: Comparison of magnetic materials at single frequency

Material	Inductance (μH)	Quality factor	FOM (Hz)10^{-3}
Coil Only	1.41	13.85	-
Mu55	5.47	45.84	0.0697
Mu100	6.525	50.71	0.0372
Mu125	6.798	52.36	3.15
Mu1200	10.59	52.28	2.1141

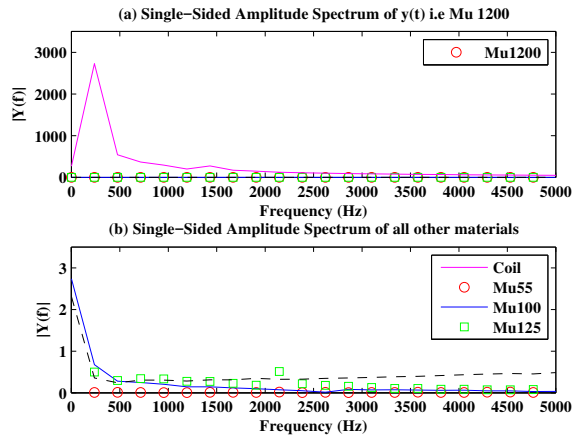

Figure 6.6: Shifted frequency spectrum. The center frequency corresponds to the resonant frequency of each material

The magnetostrictive effects were also investigated for the soft magnetic materials used as the cores. It was found that around 400 G field, the materials under test had already saturated and there was no change in the strain of the sample. Thus, at the operating DC magnetic field strengths of NMR the materials will not show any changes in strain.

6.4 Conclusions

This study shows that application of pulsed magnetic fields to pre-magnetized ferromagnetic materials leads to specific material dependent responses. In particular it is observed that certain soft magnetic materials greatly affect the free inductive decay observed in pulsed NMR systems. This signal interference due to the material's state of magnetization leads to an increase in signal decay time and in turn increases dead time in the receiver. Among the materials tested, it was found that despite their high permeability, Mu125 and Mu1200 had significantly shorter decay times compared to Mu55 or Mu100. Mu125 displayed the lowest signal decay time. However, the sample may also mask the actual NMR signal due to its high initial ringing amplitude. The observations made in this study indicate that further work on design and selection of appropriate magnetic core materials, including properties of custom designed materials, would facilitate development of a mechanism for controlling the ringing effects in NMR systems.

CHAPTER 7. FREQUENCY AND TEMPERATURE DEPENDENT MEASUREMENTS ON FERROMAGNETIC MATERIALS

As seen in chapter 6, ferromagnetic materials respond to pulsed magnetic fields at particular frequencies. Therefore, the focus of this chapter was to systematically identify and locate signal responses/ringing over a frequency span of 0.1 - 1.4 MHz and identify the sources of signal ringing. Resonant peaks that originate due to multiple factors such as NMR, electrical, magneto-acoustic, core material response, eddy currents and other factors were observed and the frequency dependent signal was analyzed in order to identify a suitable magnetic core. From the frequency dependent signal measurements, Mu 125 was identified as a suitable magnetic core for inductive sensors due to its lower signal amplitude and shorter decay time at each resonant frequency. Since the magnetic cores used for well-logging contribute to improvements in SNR, it is beneficial to have a core with high initial permeability, lower eddy current losses i.e. lower coercivity and higher saturation magnetization.

7.1 Experimental setup

As described in chapter 6, the experimental setup includes a pulse generator (Magritek Kea system), a high power amplifier, a duplexer and a software processing unit. A pulse train with a maximum signal power level of 1mW (-10 dBm) is generated using the Kea spectrometer. A simplified schematic of the measurement process is depicted in Fig. 7.1.

The generated pulse is sent to a high power amplifier where the input signal may be amplified to a maximum power level of 4kW (66 dBm). The amplified signal is routed on to the duplexer that acts like a band pass filter and then to an inductive coil where the sample/magnetic core is placed. The sample coil is a solenoid with inner diameter of 25.4 mm, length of 100 mm, consisting of 30 turns of magnet wire wound around a plastic case. The self-inductance of the coil is approximately

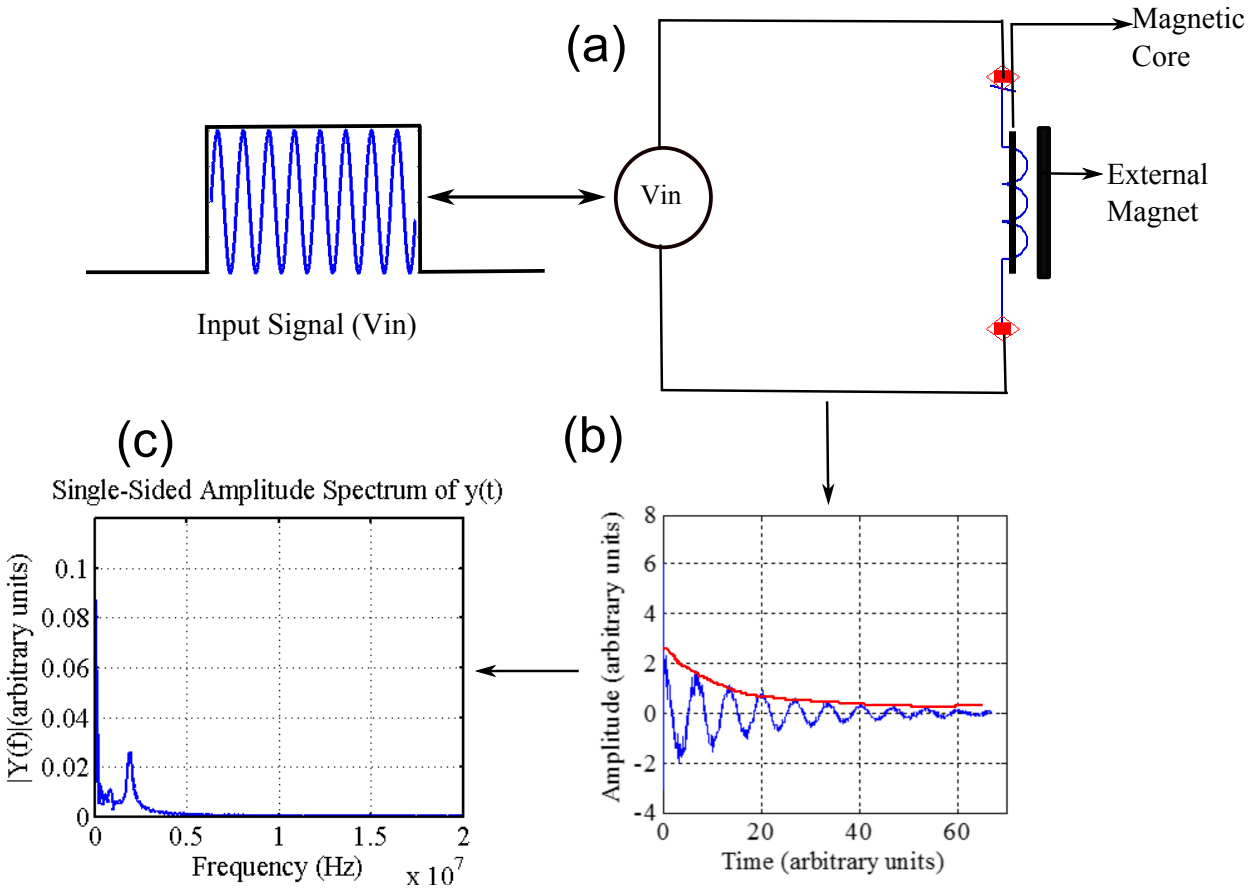

Figure 7.1: Simplified measurement process. (a) A pulsed sinusoidal is applied to the inductive coil. The magnetic core is placed within this coil and an external magnetic field (400 Gauss) is applied using a permanent magnet. (b) At resonances a decaying exponential signal ((c) corresponding peak in frequency domain) is observed.

5-10 μH. The sample's size is approximately 100mm $\times$ 10 mm $\times$ 10 mm. Multiple excitation pulses are applied to eliminate the presence of noise in the recorded signal and obtain a high SNR. After each excitation pulse, the signal from the sample is rerouted via the duplexer to the receiver unit. The received time domain signal is then transformed to the frequency domain and a broad pulse is applied at each resonant peak to determine if the resonant peak oscillations (ringing) occurs due to the magnetic material or the circuit [130]. An initial assumption made for this study is that the inductive coil doesn't receive any extraneous signals from the surroundings and only receives signals from the material inside the magnetic core.

7.1.1 Signal amplitude

The peak signal amplitude is used to determine the maximum amplitude of the resonance from the magnetic core at a particular resonant frequency. A lower amplitude is preferred for minimal overlap between actual NMR signals and signals induced due to the magnetic core.

7.1.2 Linewidth

The peak resonant linewidth is a key measure of the signal decay time. It is desirable that signals from the magnetic core decay quickly, thus limiting the interference with NMR signals from samples under test. If the linewidth, defined as in equation 6.1, or the 3dB bandwidth, is wider, the signal decay would be faster. Correspondingly, the signal quality factor at each resonance would be lower. Also, a higher coercivity leads to a narrow linewidth and is not desired.

7.2 Frequency dependent measurements

The response of the inductive sensor is affected due to the variable magnetization of the magnetic core material [131]. Based on our observations, it was expected that the measured signal response included contributions due to variable magnetization of the core and the measurement system. In general, it was expected that the signals introduced due to the system will occur at the input signal frequency and harmonics of the input signal frequency. Besides these signals, other signals appeared due to the presence of the magnetic material used as the magnetic core. These signals are assumed to originate due to the non-uniform magnetization and different relaxation times of the magnetic moments within the magnetic core material. In some cases the presence of pinning sites and imperfections within the material may also contribute to occurrence of such signals.

To evaluate the effect of magnetic material on the sensor response, several measurements with different magnetic core materials were performed. The measurements were conducted over a frequency range of 0.1 to 1.4 MHz due to the broadband capabilities of the NMR tools. The signal response for each material were identified by first applying a short pulse of 20 μs and then applying

a broad pulse of 200 μs. The short pulse was applied to scan a broad frequency range and then once the signal frequencies were identified a broader pulse was applied at those specific frequencies.

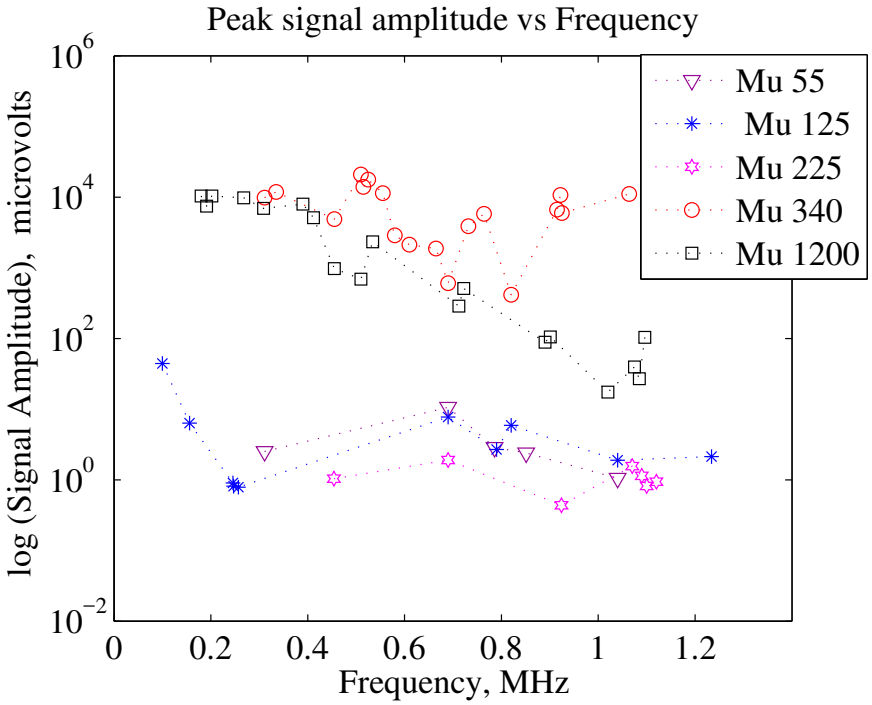

Figure 7.2: Comparison of signal amplitude for different magnetic materials. A log scale is used for improved readability. The materials are labeled according to their relative magnetic permeability.

The signals measured from the core and coil assembly may be quantified using two parameters. The first parameter is the peak signal amplitude at each peak frequency. A lower peak signal amplitude is desired since this would imply lower response from the magnetization state of the magnetic core material. The second parameter of interest is the linewidth (full-width half maximum) at each resonant peak. A higher linewidth would imply a faster signal decay at each resonance and is preferred. Fig. 7.2 is a comparison of the peak signal amplitudes for each material, acquired after the 200 μs pulse at corresponding resonant frequencies. The peak amplitude is recorded from the frequency spectrum profile for each material.

As a direct follow through of Faraday's law, equation 7.1, it was expected that the peak signal amplitude at each resonance would be directly proportional to μ_r of the material.

$$V_{emf} = -N\frac{d(B.A)}{dt} - N\mu_0\mu_r\frac{d(H.A)}{dt} \tag{7.1}$$

(here N is the number of turns in the pick-up coil, B is the magnetic flux density, A is the area of one turn of the coil and dt corresponds to increment in time, μ_0 is the permeability of free space, H is the magnetic field strength applied to the coil). However, on closer examination of the peak signal amplitudes, Fig. 7.2, it was found that the relationship between the signal amplitude and permeability wasn't linear. In fact Fig. 7.2 indicated that Mu 340 which has a relative permeability much lesser than Mu 1200 has a higher peak signal amplitude. At the same time, Mu 225's peak signal amplitude is lower than Mu 55. These observations clearly imply that besides the relative amplitude the signal amplitude is dependent on some other factors. Next, taking into account the magnetization of the magnetic core due to the excitation signal the total magnetic flux described by equation 7.2:

$$B = \mu_0(M + H) \tag{7.2}$$

can be incorporated into equation 7.1. Thus, the induced emf may be written as in equation 7.3, [98]:

$$V_{emf} = -\mu_0 N\left(A\frac{dM}{dt} + M\frac{dA}{dt} + A\frac{dH}{dt} + H\frac{dA}{dt}\right) \tag{7.3}$$

Then from equation 7.3, one may infer that the induced emf would be dependent on the rate of change of magnetization, applied field and the rate of change of area of the coil. The change in magnetic field would be steady (since the pulsed signal is sinusoidally varying) over the pulse duration and discontinuous at the start and stop of the pulse. At the same time, on application of magnetic field, the dimensions of the magnetic core material may slightly vary due to magnetostrictive effects . However, the changes in area would be in the range of 10^{-10} and the induced emf is measured to be in the range of 10 - 10000 μV. Thus, the contributions of magnetostriction to V_{emf} are negligible.

On further evaluation, comparing the variations in signal amplitude of the low permeability materials, Fig. 7.3a, it is found that they have relatively lower number of resonances in contrast

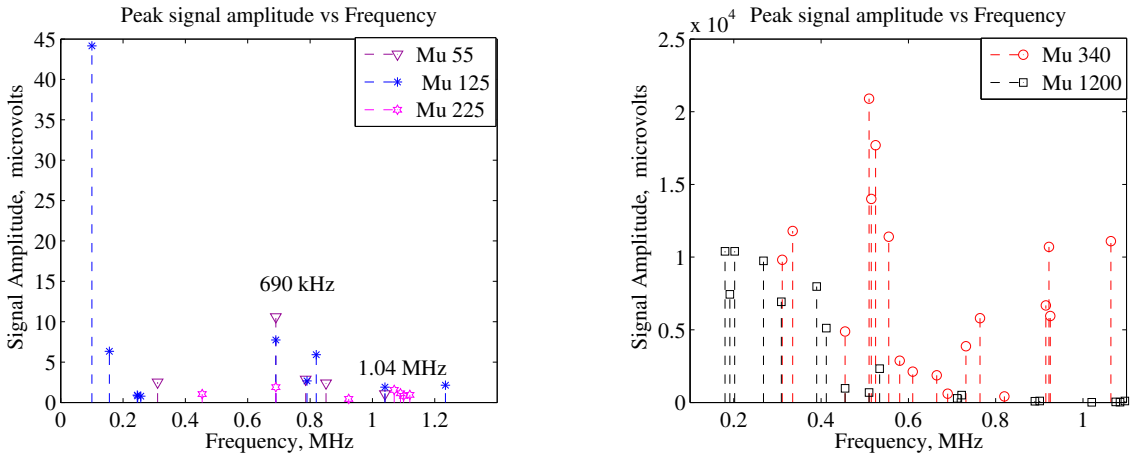

Figure 7.3: (a) Comparison of low μ_r materials, (b) Comparison of high μ_r materials

to the higher permeability materials, Fig. 7.3b. At the same time Fig. 7.3a shows that besides having low peak amplitudes (approximately 45 μV) certain resonant frequencies repeat irrespective of the material permeability (In particular, 690k, 1.04M Hz). However from Fig. 7.3b it is observed through experiments that these peaks don't repeat for the high permeability materials. While the ability to observe the resonant peaks does depend on the core material properties and the strength of the external biasing magnetic field it is also possible that these repetitive peaks originate due to structural/geometrical variations of the magnetic core material and require further investigations.

Besides controlling the peak signal amplitude and minimizing the number of resonances due to the material, the second parameter of interest is the linewidth at each resonant frequency. To minimize ringing it is important to obtain shorter FID such that the oscillations at a particular frequency decay quickly. Fig. 7.4 is a comparison of the linewidth for the different materials. It is found that in the lower frequency regime, Mu 125 has the highest linewidth and correspondingly shorter decay time.

A better estimation of the signal decay rate at each resonant frequency may also be understood by estimating the quality factor (Q factor). The Q factor is a representation of the net energy

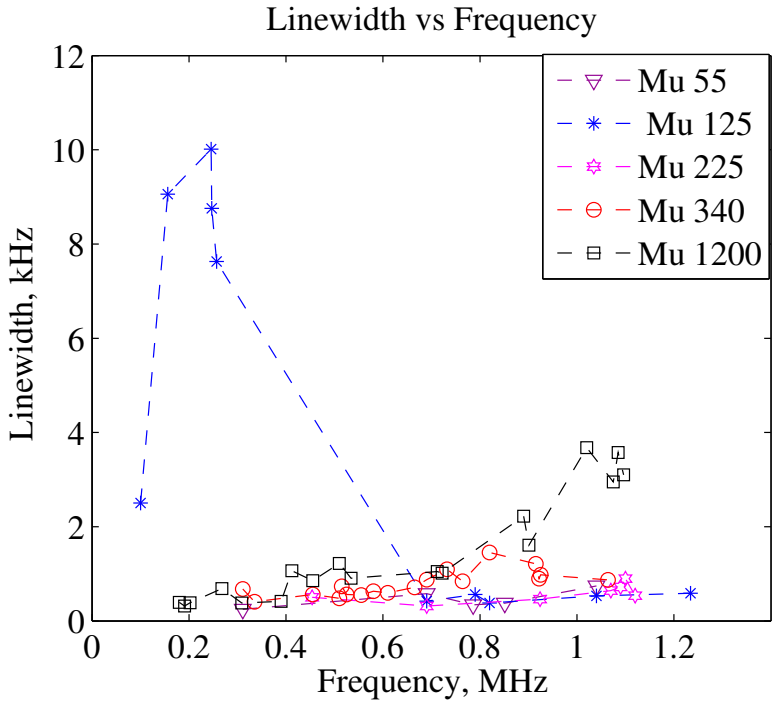

Figure 7.4: Comparison of linewidth at each resonant frequency measured over the operating frequency range.

stored at resonance. It may also be used to determine the damping rate at each resonant frequency. Generally, high Q factor systems have lower damping and ring for longer duration of time. Thus, it is desired to have a system with lower Q factor such that the oscillations/ringing may die out quickly. Mathematically, the Q factor may be estimated as a ratio of the resonant frequency to the half-power signal bandwidth (FWHM). Fig. 7.5 is a comparison of the Q factor calculated for the different materials. It is found that in the low frequency regime (below 400 kHz) Mu 125 has a lower Q factor compared to the other materials. For all the other materials, the Q factor increased with an increase in the signal frequency. In particular, in the higher frequency regime (above 400 kHz) the Q factor for Mu 1200 is the lowest. However, Mu 1200 has multiple resonant frequencies and it is desirable to eliminate the resonances caused due to the material. For this reason the properties of the magnetic material need to be altered.

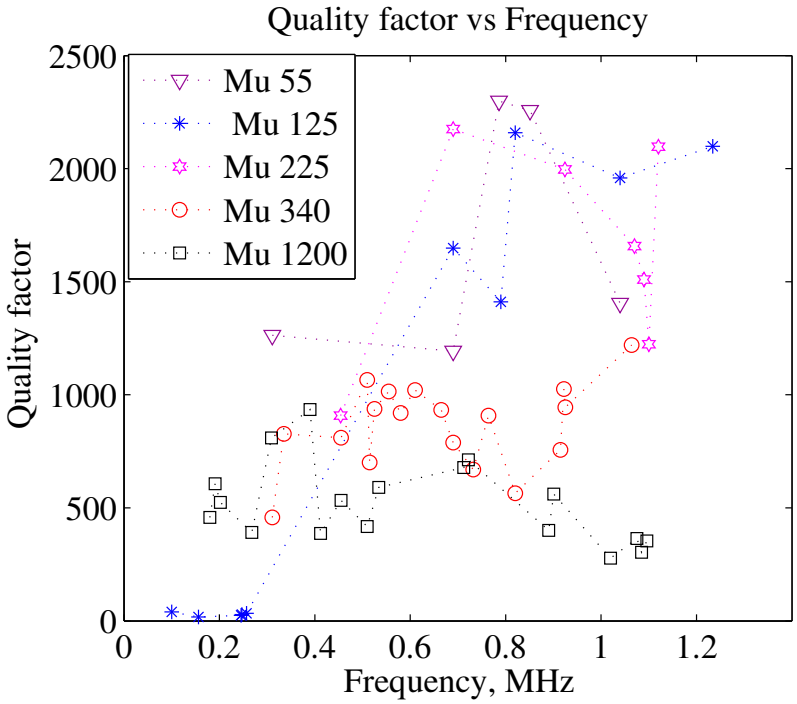

Figure 7.5: Comparison of Q factor over the entire frequency range.

7.3 Analysis on sources of resonant peaks

Prior results show that with frequency variations the response of the magnetic materials varies non-linearly. This implies that besides the material's magnetization, other factors for resonances such as the measurement system and induced magnet vibrations need to be distinguished and further analyzed. Since the resonances appear in every measurement, they are considered as interference to signals received from the magnetic core. Forming a distinction between different resonances is essential in identifying the primary contribution to the detected resonant signal. The frequency dependent measurements for the magnetic core indicate that the magnetization induced resonant peaks of the core have relatively higher amplitudes and shorter decay times at low frequencies. However, it is apparent that signals can be misinterpreted if the origin of the signal is not identified. Thus, to obtain a better understanding of the measurement it is necessary to distinguish between signals originating from the magnetic core and signals arising due to variations in external

magnetic field strength [23], induced eddy currents in sample/magnet [132], magnetization induced vibrations [133, 134] in the magnetic core or some other factors.

7.3.1 Presence of magnetic vibrations

Prior works [134, 135] describe that variations in magnetization can lead to mechanical vibrations in structures. These vibrations, often termed magneto-acoustic noise are dependent on the magnetizing frequency [134] and the geometry of the sample. As per the experimental setup described in section 7.1, it is expected that the magnetic core will experience vibrations in free space and at the same time the magnet will also be influenced by the pulsed magnetic field. Mathematically, the resonant modes will occur when the length of the sample is a quarter wavelength for a constrained sample and a half wavelength for an unconstrained sample. Higher modes can be observed at integral multiples of quarter or half wavelengths respectively [134]. Thus, the n_{th} harmonic of resonant frequency for an unconstrained sample or the magnetic core in this experiment, f_s, is defined as [134]:

$$f_s = \frac{n}{2l}\sqrt{\frac{E}{\rho}} \tag{7.4}$$

Similarly, the nth harmonic of resonant frequency for the constrained magnet, f_m, can be defined as [134]

$$f_m = \frac{n}{4l}\sqrt{\frac{E}{\rho}} \tag{7.5}$$

Here l is the length of the sample, E is the Young's modulus and ρ is the density of the material. Equations 7.4 and 7.5, provide an estimation of the vibrational modes due to the magnetic core and the magnet respectively. Since these resonant modes relate to the sample geometry and the magnetizing frequency they may require longer time to decay and therefore they are detrimental in on-site operations of such magnetic sensors.

7.3.2 Preliminary observations

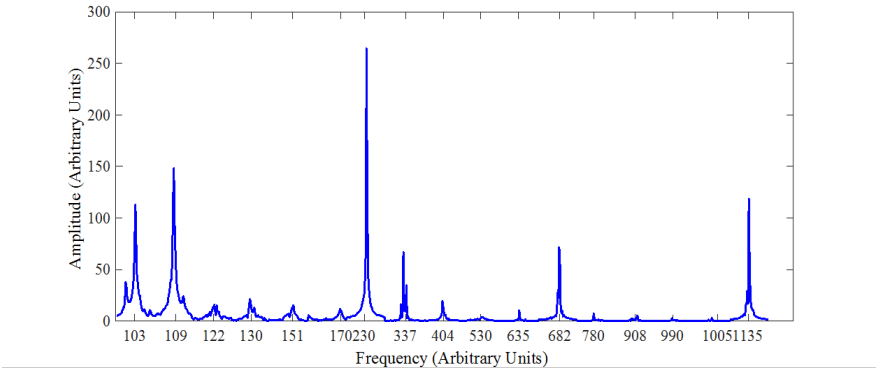

Figure 7.6: Representation of all resonant peaks measured for the powdered iron sample

To highlight the signal contributions from varied sources, a coil, inductance of 4.95 μH, 30 turns, 25 mm diameter and 100 mm length is placed next to a NdFeB $N42$ magnet. The magnetic core is placed within the coil. The entire assembly, the coil, permanent magnet and magnetic core is placed within a shielded aluminium box to minimize interference from external sources. A powdered iron sample was used as the magnetic core for this experiment. A simple representation of all the resonant peaks measured with this sample can be seen in Fig. 7.6.

Fig.7.7a, 7.7b clearly highlight the overlap between signals from the coil, magnet, magnetic core and external noise. These may all be assumed to be resonances due to the magnetic core and since Fig.7.7a, 7.7b show that there is an overlap of signals due to variations in the core's magnetization it is necessary to determine the contributing factor for each resonance.

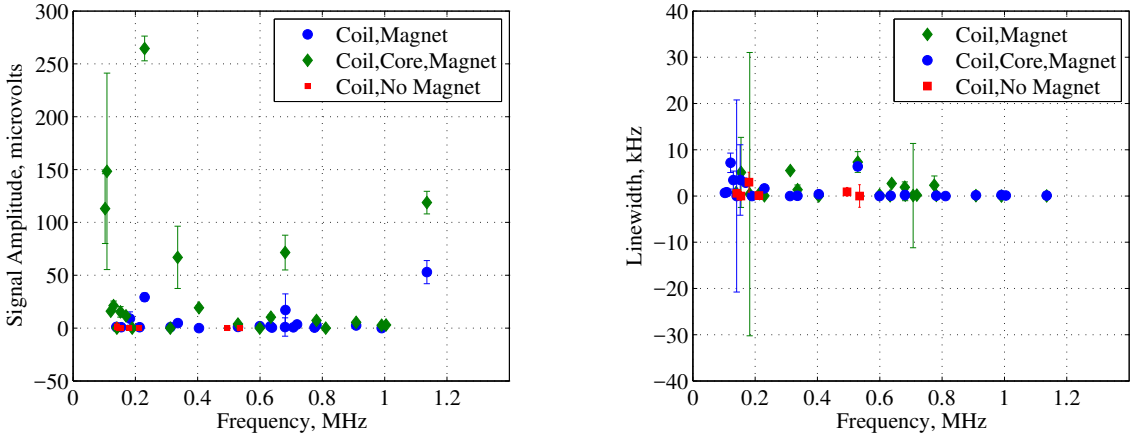

(a) Peak Signal Amplitudes

(b) Linewidths at each resonant peak

Figure 7.7: Signal amplitudes and linewidths for the inductive coil, biasing magnet and magnetic core. The signal amplitudes and linewidths were estimated from the Fourier spectrum at each resonance. Error bars are generated by averaging over 3 different repetitions.

7.3.3 Contributions from the measurement system

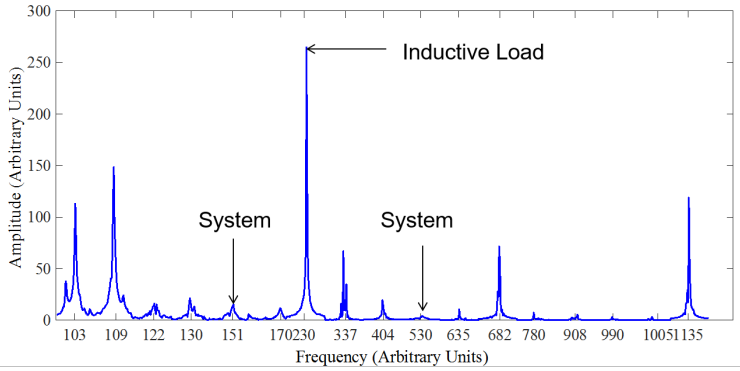

Figure 7.9: Representation of all resonant peaks highlighting peaks from measurement system

To determine the source of the signals from the measurement system, input signal and loading effects, pulsed resonance measurements were conducted with a matched 50 Ω load and an inductive load of inductance 4.95 μH, over the entire measurement frequency range. The pulse duration

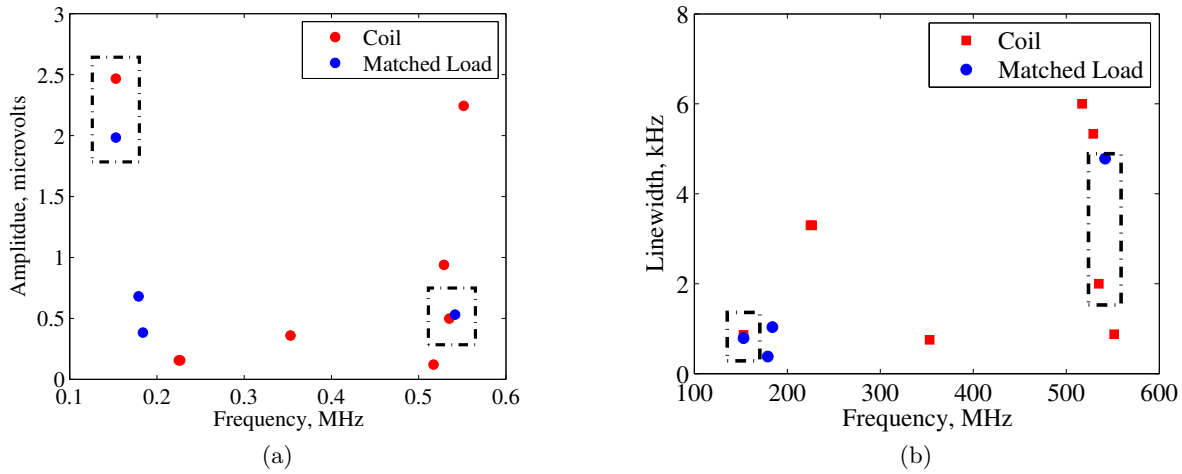

Figure 7.8: (a) Signal Amplitude Comparisons, Comparison of signal amplitudes due to a matched resistive load and an inductive load, (b) Linewidth Comparisons, Comparisons of ringing parameters for a matched resistive load and an inductive load (coil). The signal amplitudes and linewidths are estimated from the Fourier spectrum of the measured signal.

and repetition rate were set to 200 μs and 500 ms respectively. Since these correspond to low frequencies lesser than 0.1 MHz, it is understood that they cannot appear as resonant peaks in the measurement. The self resonance of the coil was also measured using a network analyzer and was found to be at frequencies (greater than 25 MHz) beyond the frequency range of interest. This implies that self resonance of the coil cannot be observed in Fig. 7.7a. As in Fig.7.8a, 7.8b, certain resonant frequencies with low signal amplitudes are identified when a matched resistive load is connected to the system. Fig. 7.8a, 7.8b show that some of these resonant peaks also repeat when the inductive load is connected to the system. This implies that these resonances are occurring due to the measurement system itself. From Fig.7.8a, 7.8b, while the signal amplitudes are comparable at the overlapping resonant peaks, the linewidth of one of the resonant peaks (530 kHz) decreased with inductive loading as observed in Fig.7.8b. This implies that signals originating from the system will take a longer time to decay at a frequency of 530 kHz, which is undesirable. It is important to note that other resonant peaks have low amplitudes and linewidths, as seen in Fig.7.8a, and can be considered in further measurements as noise. Fig. 7.9, summarizes the presence of the peaks due to

the measurement system and the peak due to the interaction of the inductor with the measurement system. These are considered as undesirable effects in our measurements.

7.3.4 Contributions from the external permanent magnet

A NdFeB N42 magnet was used to create a single-sided external biasing field. All the pulsed field measurements were repeated in the presence of this magnet. New resonant peaks, besides the resonant frequencies of the system as observed in Fig. 7.7a are observed in Fig. 7.10a. These resonant peaks are considered to originate due to surface currents induced in the magnet and changes in the effective magnetic field around the coil. The surface currents occur when the pulsed field is applied to the conductive surface of the magnet. The surface (eddy) currents are also considered to be a source of mechanical vibrations for the magnet. Then the modes induced in the magnet can be calculated using equation 7.4. Due to the nature of our experiment, the vibrations due to the magnet are also recorded by the pick-up coil. Measurement results show that multiple modes and harmonics are induced in the magnet itself. A comparison of the calculated and measured harmonic modes for the magnet may be found in Table 7.1. It was observed that only higher order modes can be observed since the frequency of operation is from 0.1 to 1.4 MHz. The peaks caused due to the magnet's vibrations are also present when the magnetic core is placed within the coil. From Fig. 7.10a as expected, it is observed that the resonant peak signal amplitudes increase in the presence of the magnet. Meanwhile the linewidths depict minimal variations in presence or absence of the magnet as in Fig. 7.10b. A summary of the calculated and measured resonances due to the vibrational modes for the magnet and the peaks due to the measurement system are observed in Fig. 7.11.

Table 7.1: Vibrational modes induced in the magnetic core and magnet

Material	E GPa	ρ kg/m^3	l m	$f_{calculated}$ kHz	Harmonic number n
Core	140	7000	0.094	24	6,7,8,13,14,17
Magnet	160	7500	0.1016	11	9,10,15,17,20

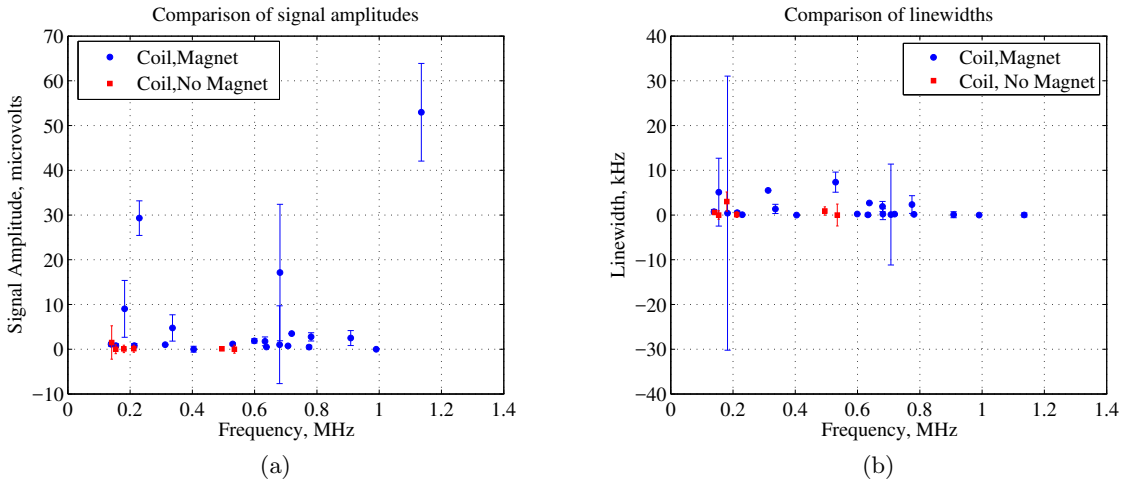

Figure 7.10: (a) Peak Signal Amplitudes,Comparison of signal amplitudes due to coil and magnet (b) Linewidths, Comparison of signal amplitudes and linewidths due to both the coil and magnet.

7.3.5 Magneto-mechanical and core material contributions

Besides vibration modes in the magnet, mechanical vibrations are also induced in the magnetic core material as observed in Table 7.1. In our experiment, there were peaks at specific resonant frequencies that could not be accounted for by either mechanical or system contributions. These peaks are considered to arise due to magneto-mechanical effects induced in the magnetic core. Fig.7.12a and 7.12b depict these resonant peaks after eliminating peaks caused due to the magnet and the system. In our experiment, these peaks are considered to originate due to intrinsic material properties of the magnetic cores. In some cases, due to the variability of the static magnetic field, some of the peaks may also appear to have shifted from expected frequencies. At the same time, addition of the magnetic core to the inductive coil changes the inductance to 18.67 μH. It is expected that the electrical resonant frequency for the inductive load would shift to a lower frequency with an increase in inductance. A summary of the peaks due to the mechanical oscillations for the magnetic core may be observed in Fig. 7.13.

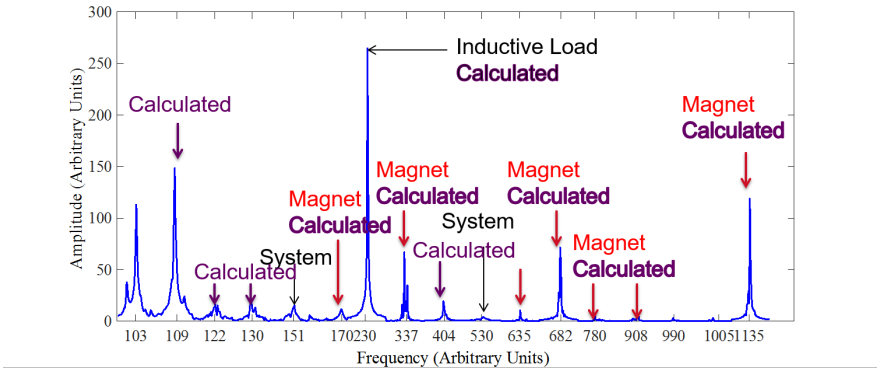

Figure 7.11: Representation of all resonant peaks highlighting peaks from magnet

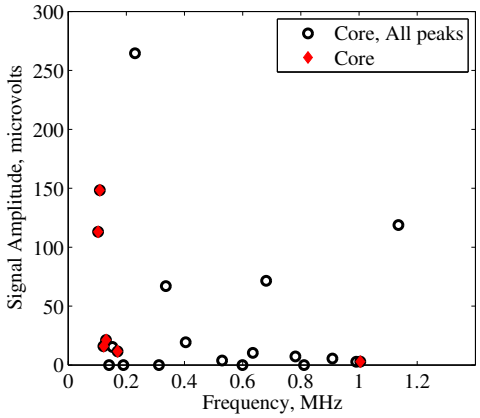

(a) Peak Signal Amplitudes

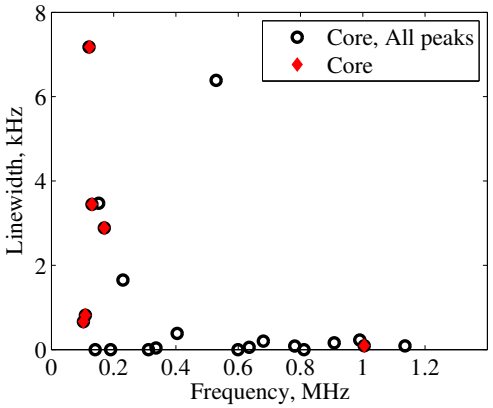

(b) Linewidths at each resonant peak

Figure 7.12: (a) Peak Signal Amplitudes, Comparison of linewidths due to coil, magnet and magnetic core (b) Linewidths, Comparison of signal parameters due to coil, magnet and magnetic core. The peaks from the measurement system and due to the magnet are eliminated in the core measurements in these graphs.

Based on the pulsed resonance measurements, it can be confirmed that different resonant peaks originate from different sources. While the peaks from the measurement system and the magnet may be easily decoupled, identifying peaks due to the magnetic core requires further analysis. In particular, if some peaks due to the magnetic core overlap with the peaks due to the system/magnet

they are not easily identifiable as separate peaks. At the same time, due to the variability in external magnetic field, all the vibrational modes may not be energized equally thus leading to various resonant peaks across the spectrum.

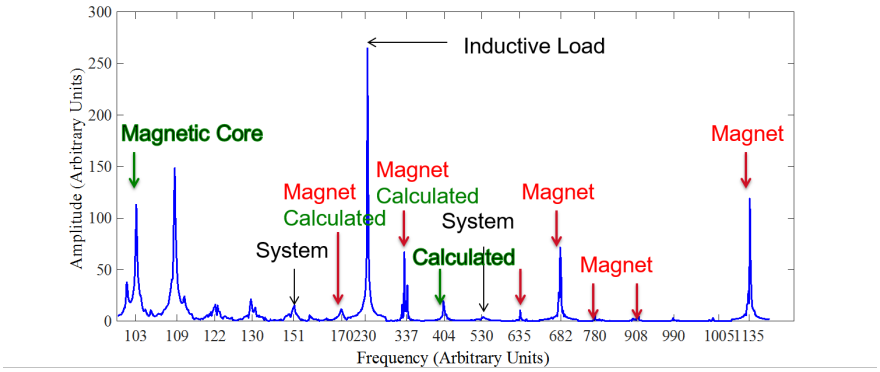

Figure 7.13: Representation of all resonant peaks highlighting peaks from magnetic core

7.4 Temperature dependent measurements

The magnetic sensors used in oil well logging applications also operate under conditions of high temperature and pressure. The sensors are placed within drilling tools and operated under continuous mechanical vibrations, low-biasing fields and elevated temperatures of upto 473 K [136]. In such harsh environments, acquiring reliable data requires improvements in signal to noise ratio (SNR) and this necessitates the use of high permeability magnetic cores within the sensors. The response of the magnetic cores used within these sensors is also dependent on their operating temperature. Magnetic materials can become paramagnetic above Curie temperature, and can also exhibit non-linearities at elevated temperatures [137, 138].

In this work, the effect of temperature on signals acquired from an inductive sensor with different magnetic cores was studied [139]. While the Curie transition temperature for the magnetic cores used in this study is higher than 473 K, high temperatures cause changes in magnetization [98] and thus variations in the measured signals. Measurements were taken over a frequency range of 0.1 - 1.4 MHz with different temperatures. The signals were acquired in the time domain and the

frequency spectrum is calculated. Resonant signal amplitudes as well as resonant peak linewidths were recorded across the indicated frequency range.

7.4.1 Experimental Setup

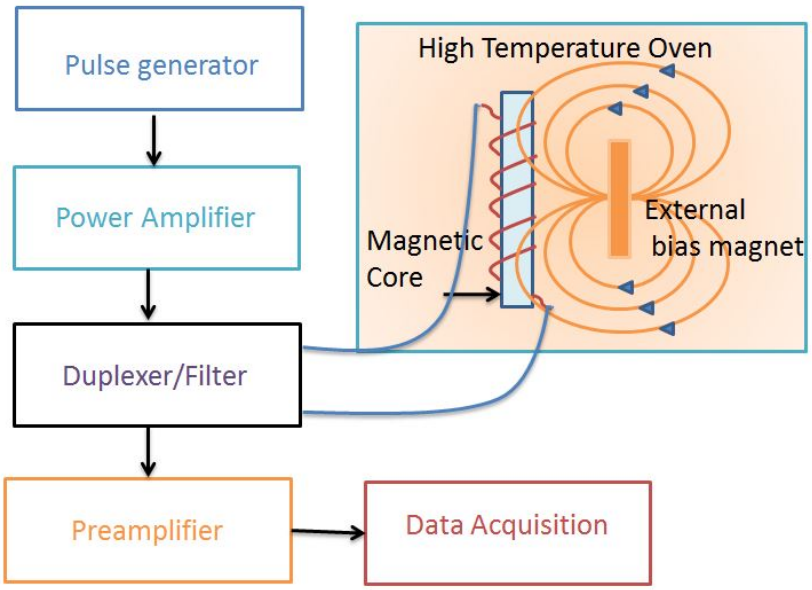

Figure 7.14: Schematic of measurement system. Pulsed sinusoid is generated by the pulse generator, amplified and applied to the inductive coil. The pulse response is then rerouted via the duplexer and the preamplifier.

A schematic representation of the experimental setup is shown in Fig. 7.14. A Kea system that can generate a pulsed sinusoidal at a maximum power of 1 mW was used as the pulse generator. The power amplifier increased the input signal to a maximum level of 4 kW. A 30 turn inductive coil, with 25 mm diameter and 100 mm length was placed 20 mm away from a biasing magnetic field from a SmCo magnet. The SmCo magnet was selected instead of NdFeB due to its capability to withstand higher operational temperatures. The magnetic core was placed within an inductive coil that was mounted onto a glass tube. The entire assembly (the inductive coil and the magnet)

was placed within a shielded aluminum box and then placed within the oven chamber where the sample could be heated up to a maximum of 473 K. For this study, the ringing properties were measured with temperature variations from 300 - 400 K.

7.4.2 Ringing Measurements

7.4.2.1 Signal Amplitude Variations

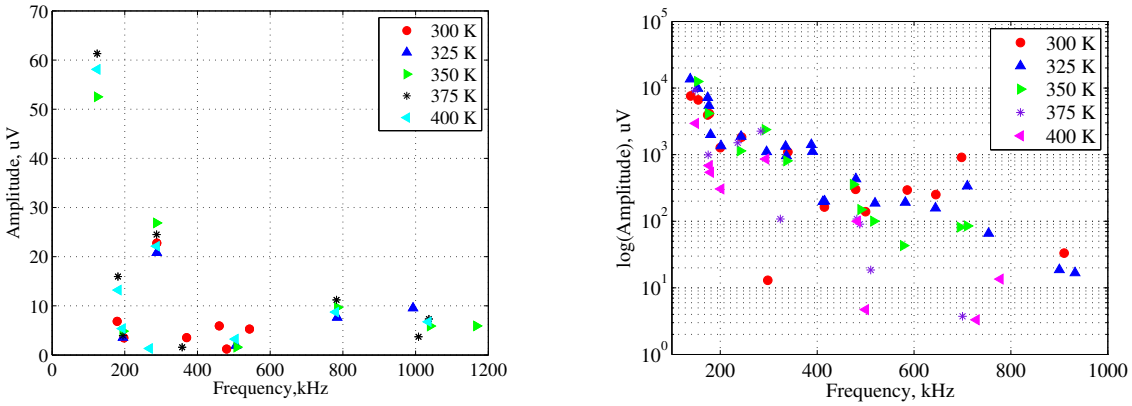

(a) Signal Amplitudes for Mu55

(b) Signal Amplitudes for Mu1200

Figure 7.15: (a) Variations in peak signal amplitude for MU55. Temperature is varied from 300 - 400 K (b) Variations in peak signal amplitude for MU1200. Temperature is varied from 300 - 400 K. A log scale was used for improved readability.

Two samples, a low permeability powdered alloy (Mu55) and a high permeability ferrite (Mu1200) sample were tested with variations in external temperature. From Fig.7.15a and 7.15b, it was observed that with increasing thermal activity, there was a reduction in the number of resonant peaks for both samples. For Mu55, there is no significant variability in the measured signal amplitudes. This implies that Mu55 was stable under thermal variations. Meanwhile, Fig. 7.15b depicts the signal amplitude variations for Mu1200. Here, similar to Mu55, it was observed that with an increase in temperature, the number of resonant peaks decreased and at the same time the signal amplitudes were also lower at higher frequencies. This contrasting characteristic of the low and

high permeability material implies that with thermal activation, the low permeability powdered alloy allows for higher interaction between the magnetic domains [98] and insignificant variations to the signal amplitude. At the same time, Mu1200, is affected by temperature variations and depicts a decrease in the number of resonant peaks and peak amplitudes.

7.4.2.2 Linewidth Variations

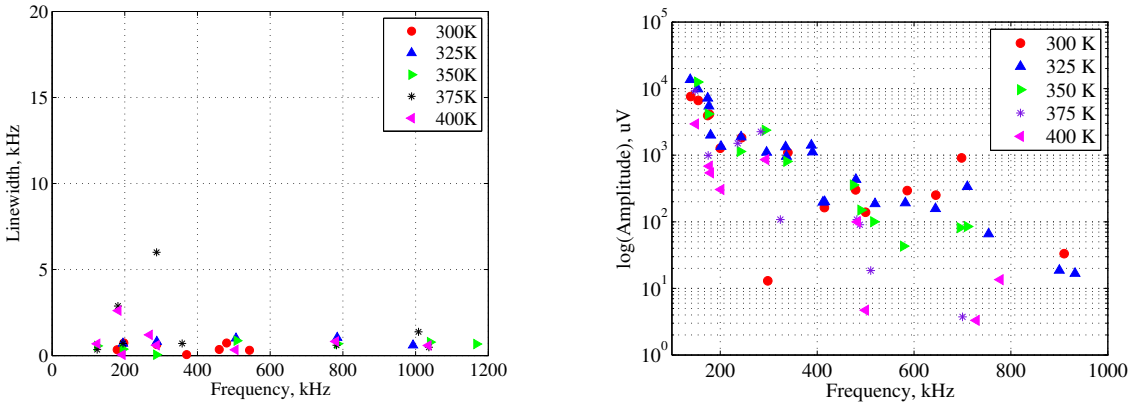

(a) Linewidths for Mu55

(b) Linewidths for Mu1200

Figure 7.16: Comparison of linewidths for (a) Mu 55 and (b) Mu 1200 with variations in temperature

To minimize the contributions of ringing, it was also expected that the resonant peaks introduced due to the magnetic core decay faster. This implies that the linewidth at each resonant peak should be wide. From Fig. 7.16a, it is observed that for Mu55, the signal linewidth is uniformly narrow over all signal frequencies indicating that the signals take longer to decay. At the same time Fig. 7.16b shows that Mu1200 has a wider linewidth at higher frequencies. The linewidth remains uniform across all measurement temperatures.

Overall, ringing measurements indicate that at elevated temperatures, a large number of resonant peaks disappear for both Mu55 and Mu1200. For Mu55, besides the decrease in the number of resonances, there is hardly any variation in the signal decay rate and peak amplitudes remain consistent for lower temperature measurements. For the ferrite material, Mu1200, the observed

number of resonant peaks also decreased with an increase in temperature and the signal decay is high only at higher frequencies. Ultimately, for the application of oil well-logging, it is necessary to obtain a magnetic core material which has the lowest number of resonances, lowest peak signal amplitude variation with temperature changes and larger linewidth (shorter signal decay time) at high temperatures. In summary, variations in material characteristics are equally important in determining the number and nature of resonances. Mu55 which is a powdered alloy had low signal amplitude, large decay time and fewer resonant peaks with increase in temperature. Mu1200 which is a spinel ferrite had a high signal amplitude at low frequencies, high decay time at low frequencies and a lower number of resonant peaks with increase in the external temperature.

7.4.3 Magnetic Measurements

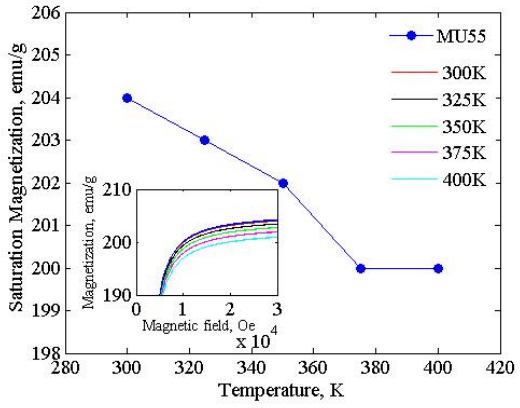

(a) Mu55 Saturation Magnetization

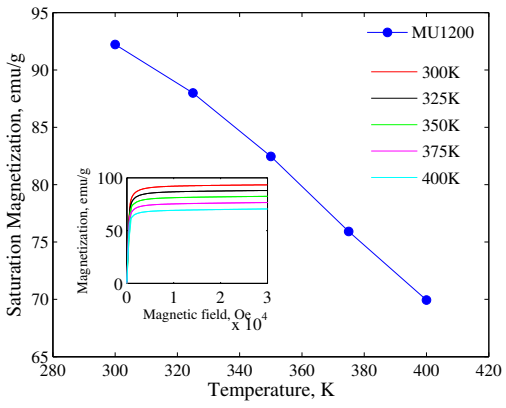

(b) Mu1200 Saturation Magnetization

Figure 7.17: Variations in saturation magnetization with increase in temperature for (a) Mu 55 and (b) Mu 1200

Magnetic hysteresis measurements allow us to determine the variations in magnetization characteristics with temperature. Fig. 7.17a depicts the change in magnetization at 2.4 kA/m for Mu 55 with temperature elevation. It is observed that the magnetization slightly decreases with increase in temperature and plateaus after about 375 K. As seen in Fig. 7.17b, the magnetization

for Mu 1200 behaves similar to Mu 55. The saturation decreases rapidly with increase in temperature. This indicates that the ferrite has not saturated completely at 400 K at a maximum field of 2.4 kA/m. In summary, the magnetic hysteresis measurements show that with an increase in temperature, magnetic materials can be magnetized with ease and this relates to a decrease in the number of resonant peaks and correspondingly lower signal amplitudes.

7.5 Conclusions

A new method to identify and quantify the response of the magnetic core material for a magnetic resonance sensor over multiple frequencies has been established. On the basis of the parameters of interest i.e. signal amplitude and linewidth at each resonant frequency Mu 125 is identified as the most suitable magnetic core for oil-field well logging tools investigated. Even though Mu 225 has a lower signal amplitude in contrast to Mu 125 it has a higher linewidth over the measured frequency regime, especially in the lower frequency range. Meanwhile, Mu 1200 has a higher linewidth in the high frequency range and may be considered if the signal amplitude, linewidth and number of resonances are controlled by variations in material properties.

Additionally, the peaks introduced due to the mechanical oscillations in the magnet, due to the measurement system and due to the magnetic core can be distinguished. It is understood that with variations in the magnet, magnetic field strength and magnetic core, the resonant peaks will shift in frequency but will still be present and will respond in the same way. It is also necessary to highlight that multiple resonant peaks were not originating only due to the magnetic core. Thus, creating a distinction is vital to determine the signals which are directly received from the magnetic core material.

The interrelationship between ringing, magnetic properties of the sensor core and operating temperature of the sensor has been presented. Based on measurements and observations made, it was found that for the low permeability material the variations in signal amplitude and linewidth are low and the magnetization reduces with an increase in temperature. For the high permeability

material, the signal amplitudes decreased, the linewidths increased and the saturation magnetization decreased with rise in temperature.

In summary, low permeability materials can be used for sensors that require minimal variations in the magnetic core's response with changes in temperature. The high permeability materials with greater linewidth are preferred in higher frequency applications where the resonant peaks must decay quickly and should not interfere with actual magnetic resonance measurements. At the same time, the material composition can be used to determine if the ringing parameters would vary with increase in temperature for different core compositions. Future work should include a study of the ringing parameters with variations in the material composition.

7.6 Avenues for improvements

The measurement results indicate that the relationship between the number of resonances, magnetic permeability and material composition need to be investigated further. Improvements in material performance, i.e. lower signal amplitude and greater linewidth may be obtained by controlling the particle sizes and in turn controlling the long-range domain level interactions of the magnetic core material. Besides material properties the circuit, material and acoustic resonances need to be decoupled from the responses due to the material. Further investigations are also needed in determining the effects if any of magnetostriction on ringing in the frequency range under consideration.

On the basis of this work, a method to identify peaks from multiple contributing sources is established. While these peaks also depend on the measurement parameters, the contributions due to the magnetic core need further investigation and analysis. Especially the effect of external field variability on the frequency, signal amplitude and linewidth needs to be analyzed. Ability to distinguish between different resonant peaks will be a vital resource for unilateral NMR sensors users such as oil well logging engineers for better interpretation of the observations during NMR examinations.

CHAPTER 8. CONCLUSIONS

The ability to perform non-invasive studies on varied materials via portable mechanisms has been an ongoing effort in the last few decades [57, 67, 102]. The nondestructive testing industry has been manufacturing and using such devices for on-site and in-situ measurements [73]. However, magnetic sensing with the purview of portable diagnostics for medical applications remains to be an area with tremendous opportunities. The major challenges on this front remain the design and development of low cost measurement systems which can detect signals in varying conditions. New techniques and measurement mechanisms are thus required to facilitate developments for portable data acquisition and processing. With this perspective, in this work, an approach towards designing a portable magnetic resonance sensor was established. Different versions of portable magnetic resonance sensors were tested. Sensor design elements were individually tested and sensor performance was successfully evaluated for the application of oil well logging and portable diagnostics. An overview of the design stages for prototyping a portable NMR sensor and measurement results from a proof of concept prototype is presented in Appendix 10. At each design stage, the intent of maximizing SNR, detection volume and detection distance were considered.

A major focus of this work was conceptualizing and developing a portable magnetic resonance sensor, while identifying the associated challenges for realization of such designs. The design process included selection and modeling of appropriate magnet geometries to produce static magnetic fields, controlling pulse currents through inductors at the required switching rate and verifying system operations on assembling the different units. The first challenge which was introduced in making the system portable was operation at low field strengths. This caused a reduction in the maximum operational frequency and thus led to a limited capability in distinguishing signals from noise. Besides the low SNR, the non-uniformity of the static field also posed a limitation on the measurement. Only smaller regions near the magnet surface could be detected. To overcome such

effects of spatially varying static fields, ring magnet geometries were used to identify localized regions with magnetic field stability in the magnet's exterior. Various modifications to the magnet geometries were successfully implemented and the design constraints for permanent magnets were identified.

Additionally, the design and challenges of a portable pulsed magnetic field generator were discussed. Obtaining high-frequency pulsed sinusoidal fields (both monophasic and biphasic) is a challenge for most portable systems due to the slow current switching in inductors and limited frequency tunability due to narrow bandwidths of tuned loads [140]. Moreover, in our portable design, obtaining high currents with 50 % duty cycle limited the maximum operational frequency of the designed circuit. Nonetheless, various pulsed field generator designs were simulated and implemented, and successful operations, with both monophasic and biphasic pulses were executed at frequencies upto 10 MHz.

Prior to this work, similar portable magnetic resonance sensors were limited to well logging applications, nondestructive testing and portable imaging applications [86, 102, 141]. However, the possibility of incorporating such sensors to medical diagnostics is affirmed via the measurements made with the "proof of concept" device measurements presented, Appendix 10. Measurements for ferromagnetic materials show that the non-uniform magnetization of the ferromagnetic materials causes spurious signals to appear. However, measurements with organic media show that the prototype system can be used for estimating concentrations of various species and even absorption rates of magnetic species. Thus, such devices hold the promise for future diagnostic applications.

In conclusion, the design, testing and measurements performed within this research set a benchmark for explorations of unconventional methods for portable medical diagnostics. In general, this work successfully demonstrates the operations of a portable magnetic resonance sensor and is a significant contribution towards producing such devices for various applications.

CHAPTER 9. MESSAGE TO FUTURE RESEARCHERS

As I reflect on the wide and interdisciplinary nature of this research work, my first message to any researcher in this field is to not be overwhelmed with the immense diversity, but to enjoy the beauty of the interconnections, this is how most future research is bound to be. The field of magnetics and in general any applied research in the present day interweaves through several diverse aspects. I believe and hope that researchers in different areas will select avenues of their interest, embrace and push forward the research boundaries in their interest areas. To begin wondering about the possible directions, I would first urge researchers to think ten years ahead of time, and also envision the pace of technological development at that stage. While many researchers have interesting ideas worth exploring, often the funds or technological development isn't at the same pace and some researchers face challenges in connecting abstract work to the realities of everyday existence. I would encourage students and researchers alike to find the right fit, a match between their aspirations, technology and the right people who can facilitate the transformation of dreams to reality. In every aspect, a PhD work is a life-changing experience, a definition of one's learning and thought process and students embarking on this journey, should be ready to be deeply bothered by questions only to forget solutions while forming new questions the following day.

Simplistically, it would be easy to inform the future researchers that everything that I was unable to achieve would be a good direction to start with. However, a long-term vision would define the path for future researchers much more meaningfully. When I was pursuing this research, I was excited by wearable technology, sensors and wanted to see how medical diagnostics could become more accessible for a common man. Ten years from now, this will be common place with most technological advancements and other new questions on high-speed measurements will arise. In the context of this work, the ability to predictably model the interactions between DC and pulsed fields and estimate the effect on objects in the near and far-field would impact several

fields of research in future years. While the quasi-static nature of the pulsed fields would pose a challenge in predicting the momentary responses from varied materials, both linear and non-linear, a steady-state solution could be used to obtain approximate estimates about spatial variations. Further studies on impact of field non-uniformity would also affect the scalability and range of measurements. 2D or 3D images in exterior of portable sensors may be obtained via meticulous data acquisition and processing. A detailed evaluation of the non-uniformity of static fields can be easily pursued via use of existing software packages.

In the scope of this research, the following areas would be of interest to researchers focusing on devices or high-speed system interactions with magnetic phenomena. In order to make some or most of these efforts meaningful, access to adequate simulation, testing and measurement capabilities would be needed via collaborative ventures.

1. **Design of magnet geometries to support multi-point measurements**

   While this work demonstrates that to obtain higher SNR and spatial resolution it is beneficial to obtain NMR signals from a particular measurement location , multi-point measurements would make the portable NMR system viable to various applications. As an initial effort, researchers might consider detection along layers concentric to the magnet or for thin objects. However, another approach might be to identify a modification of magnet geometries such as previously used Halbach arrays or other assemblies. Moreover, magnetic shielding techniques may be employed to focus the flux to specific regions of investigation.

2. **Design of transmit and receive geometries to improve spatial data acquisition**

   Besides shaping the static field location and strength, the pulsed field also plays an important role. Conventionally, many designs have used the same coil for transmit and receive due to the excellent isolation between the two signals. However, use of multiple transmit and receive coils provides the flexibility of spatial placement and sequential excitement as in phased arrays. The main trade-off with use of multiple transmit coils would be higher power consumption though a timing sequence could be used as a controlling mechanism. It would also be advantageous

to focus the pulsed fields to specific detection regions of interest. Due to prior knowledge on the spatial distribution of static field, the locations where the pulsed fields can be focused are known.

3. **Studies on near-field effects such as mutual coupling between transmit, receive and sample**

   With the improvements in the coil-design, a major challenge lies in decoupling the transmitted signal from the received signal. One way to do this might be to use a lock-in amplifier which would operate at a particular reference frequency. Besides this, signal processing in the frequency domain would give users an opportunity to locate signal obtained from varied locations. While most of the signals are obtained at the transmitted frequency, signals from other locations give users a hint about spatially locating other regions of interest. Lastly, due to the proximity of the sample and measurement unit, there would be significant amount of noise due to reflections, absorption and other lossy effects.

4. **Design of a tunable wideband pulsed field generator with varied operational frequencies**

   Since design of pulsed magnetic fields is considered a fundamental contribution of this work, it would be beneficial to obtain frequency tunability over specific frequency ranges. This would extend the detection region and potentially contribute to obtaining higher SNR. Due to the availability of rapid prototyping facilities, design of varied pulsed field generators would be an achievable task and would greatly enhance the foray of portable electronic systems for magnetic resonance applications. Additionally, flexible control on the regions where the maximum impact of the pulsed field needs to be achieved may occur with modifications and improvements in coil design.

5. **Design of noise cancellation or absorption mechanisms**

   A major challenge observed throughout this endeavor was separation of noise from the signals of interest. For the NMR measurements, signal averaging, single frequency detection and

repetitive measurements were used to eliminate different sources of noise. However, due to the low static fields, higher operational frequencies can't be used. Therefore, efforts need to be made to either increase the signals from the samples or to eliminate noise to easily distinguish signals from noise.

6. **Design of pulse sequences with variations in sensor assembly**

   As with all NMR measurements, pulse sequencing methods will be created as per the demand and requirement of the applications as well as the improvements in the hardware and software capabilities. These modifications are subject to the materials under consideration.

The extent of the endeavor in this work is beyond the development of portable sensor systems for varied applications. This endeavor shows that with a team of researchers focused on the development of electronics and magnetic sensors, the landscape of portable diagnostics can completely change in the next decade. The basic roadblocks and ways to overcome some of them are discussed in the chapters of this document and hopefully assist future researchers in making meaningful discoveries and inventions on their path to learning about magnetism, sensors and high-speed electronics.

CHAPTER 10. CONTRIBUTIONS

This chapter summarizes aspects of this dissertation which will contribute to developments in the areas of magnetism and magnetic resonance sensors. Besides demonstrating methods of acquiring magnetic resonance signals in non-uniform magnetic fields this work further highlights the design considerations for each sub-unit which can be assembled to develop different magnetic resonance detection systems as per the application requirements. Each contribution has resulted in a publication in either the IEEE Transactions on Magnetics, Journal of Applied Physics or AIP Advances. Key highlights from each chapter are described below.

Chapter 3, shows how permanent magnet geometries, specifically ring magnets, can be used to measure signals a couple mm away from the sensor surface. Furthermore, the chapter shows how larger stable field regions can be obtained by use of symmetrical dual ring magnet geometries.

Chapter 4, discusses the design of a portable pulsed field generator using an inductor connected to a fast switching FET. The chapter discusses possible effects of variable duty cycle and switching device on the generated pulsed magnetic fields or currents.

Chapter 5, describes an improved pulsed field generator design, eliminating the loading effects between the switching and signal generation stage by introduction of an operational amplifier. Additionally, the circuit described in this chapter can operate at a frequency of 5 MHz (or upto 10 MHz) and handle high pulsed currents.

Chapter 6 and 7, describe the experimental measurements for ferromagnetic materials in presence of non-uniform magnetic fields produced by permanent magnets. Such materials are used to enhance captured signals in oil well logging tools and the chapters describe how signals obtained due to non-uniform magnetization of the ferromagnetic material affect the operations of the described tool.

Appendix 10 summarizes the measurements performed using a commercial magnetic resonance sensor on various organic media thus confirming the feasibility of magnetic resonance measurements in non-uniform fields.

In summary, this work has succeeded in delivering the following aspects to the field of portable sensor technologies.

1. Method to identify regions of localized field in the exterior of permanent magnet geometries (Chapter 3) and methods to enhance the field strength at such locations

2. Design, implementation and testing of four different pulsed sinusoidal magnetic field generators (Chapters 4 and 5)

    a. Pulsed field generator operable at a frequency of 2 MHz and allowing 0.5 A of current through an inductor with different switches

    b. Pulsed field generator operable at a frequency of 0.5 MHz with controlled current based on the drain voltage

    c. Monophasic pulsed field generator operable at a frequency of 5 MHz with upto 10 A of current through an inductor

    d. Design of a biphasic pulsed field generator operable at a frequency of 1 - 3 MHz with upto 50 A of current through inductor

3. Design of various coil geometries that can be utilized for transmission and reception with both the monophasic and biphasic field generators

4. Characterization measurements for both ferromagnetic and organic materials (Chapters 6, 7 and Appendix 10)

5. Characterization of system operations using (Chapter 4, 5, 6, 7, 10)

    a. Commercially developed prototype sensor operable at a frequency of 6.7 MHz

    b. Commercially developed system operable in a frequency range of 0.1 - 1.4 MHz

c. Locally developed sub-systems comprising of permanent magnet assembly, pulsed field generator, transmit and receive coils

BIBLIOGRAPHY

[1] W. J. Fleming, "New automotive sensors: A review," *IEEE Sensors Journal*, vol. 8, no. 11, pp. 1900–1921, 2008.

[2] K. Mohri, T. Uchiyama, L. Shen, C. Cai, and L. Panina, "Sensitive micro magnetic sensor family utilizing magneto-impedance (mi) and stress-impedance (si) effects for intelligent measurements and controls," *Sensors and Actuators A: Physical*, vol. 91, no. 1-2, pp. 85–90, 2001.

[3] S. Chakrabarti, "Modeling of 3d magnetostrictive systems with application to galfenol and terfenol-d transducers," Ph.D. dissertation, The Ohio State University, 2011.

[4] C. P. Gooneratne, B. Li, and T. E. Moellendick, "Downhole applications of magnetic sensors," *Sensors*, vol. 17, no. 10, p. 2384, 2017.

[5] R. Freedman, V. Anand, B. Grant, K. Ganesan, P. Tabrizi, R. Torres, D. Catina, D. Ryan, C. Borman, and C. Krueckl, "A compact high-performance low-field nmr apparatus for measurements on fluids at very high pressures and temperatures," *Review of Scientific Instruments*, vol. 85, no. 2, p. 025102, 2014.

[6] J. Jankowski, S. El-Ahmar, and M. Oszwaldowski, "Hall sensors for extreme temperatures," *Sensors*, vol. 11, no. 1, pp. 876–885, 2011.

[7] M. Jaafar, J. Gómez-Herrero, A. Gil, P. Ares, M. Vázquez, and A. Asenjo, "Variable-field magnetic force microscopy," *Ultramicroscopy*, vol. 109, no. 6, pp. 693–699, 2009.

[8] J. Selvaraj, G. Y. Dayanikli, N. P. Gaunkar, D. Ware, R. M. Gerdes, and M. Mina, "Electromagnetic induction attacks against embedded systems," in *Proceedings of the 2018 on Asia Conference on Computer and Communications Security*, ser. ASIACCS '18. New York, NY, USA: ACM, 2018, pp. 499–510.

[9] E. Ramsden, *Hall-effect sensors: theory and application*. Elsevier, 2011.

[10] J. Lenz and S. Edelstein, "Magnetic sensors and their applications," *IEEE Sensors journal*, vol. 6, no. 3, pp. 631–649, 2006.

[11] M. J. Caruso, T. Bratland, C. H. Smith, and R. Schneider, "A new perspective on magnetic field sensing," *Sensors-Peterborough*, vol. 15, pp. 34–47, 1998.

[12] V. Varma, A. Ray, Z. Wang, Z. Wang, and R. Ramanujan, "Droplet merging on a lab-on-a-chip platform by uniform magnetic fields," *Scientific reports*, vol. 6, p. 37671, 2016.

[13] G. Lin, D. Makarov, and O. G. Schmidt, "Magnetic sensing platform technologies for biomedical applications," *Lab on a Chip*, vol. 17, no. 11, pp. 1884–1912, 2017.

[14] Y. Wang, J. Li, and D. Viehland, "Magnetoelectrics for magnetic sensor applications: status, challenges and perspectives," *Materials Today*, vol. 17, no. 6, pp. 269–275, 2014.

[15] P. Ripka, *Magnetic sensors and magnetometers*. Artech House, 2001.

[16] Q. Wang, R. Gao, and S. Liu, "Topology optimization based design of unilateral nmr for generating a remote homogeneous field," *Journal of Magnetic Resonance*, vol. 279, pp. 51–59, 2017.

[17] C. M. Collins, *Electromagnetics in Magnetic Resonance Imaging*, ser. 2053-2571. Morgan & Claypool Publishers, 2016.

[18] E. Fukushima, *Experimental pulse NMR: a nuts and bolts approach*. CRC Press, 2018.

[19] A. Petrovic, E. Scheurer, and R. Stollberger, "Closed-form solution for t2 mapping with non-ideal refocusing of slice selective cpmg sequences," *Magnetic resonance in medicine*, vol. 73, no. 2, pp. 818–827, 2015.

[20] N. N. Yadav, A. M. Torres, and W. S. Price, "An improved approach to calibrating high magnetic field gradients for pulsed field gradient experiments," *Journal of Magnetic Resonance*, vol. 194, no. 1, pp. 25 – 28, 2008.

[21] Y. Zhang, L. Xiao, G. Liao, and B. Blmich, "Direct correlation of internal gradients and pore size distributions with low field nmr," *Journal of Magnetic Resonance*, vol. 267, pp. 37 – 42, 2016.

[22] P. Judeinstein, F. Ferdeghini, R. Oliveira-Silva, J.-M. Zanotti, and D. Sakellariou, "Low-field single-sided nmr for one-shot 1d-mapping: Application to membranes," *Journal of Magnetic Resonance*, vol. 277, pp. 25 – 29, 2017.

[23] F. Casanova, J. Perlo, and B. Blümich, "Single-sided nmr," in *Single-Sided NMR*. Springer, 2011, pp. 1–10.

[24] H. Watanabe, N. Takaya, and F. Mitsumori, "Non-uniformity correction of human brain imaging at high field by rf field mapping of b1+ and b1-," *Journal of Magnetic Resonance*, vol. 212, no. 2, pp. 426 – 430, 2011.

[25] S. Rodts and D. Bytchenkoff, "Extrapolation and phase correction of non-uniformly broadened signals," *Journal of Magnetic Resonance*, vol. 233, pp. 64 – 73, 2013.

[26] J. C. Garca-Naranjo, I. V. Mastikhin, B. G. Colpitts, and B. J. Balcom, "A unilateral magnet with an extended constant magnetic field gradient," *Journal of Magnetic Resonance*, vol. 207, no. 2, pp. 337 – 344, 2010.

[27] R. L. Kleinberg and J. A. Jackson, "An introduction to the history of NMR well logging," *Concepts in Magnetic Resonance*, vol. 13, no. 6, pp. 340–342, 2001.

[28] P. T. While, L. K. Forbes, and S. Crozier, "3d gradient coil design for open mri systems," *Journal of Magnetic Resonance*, vol. 207, no. 1, pp. 124 – 133, 2010. [Online]. Available: http://www.sciencedirect.com/science/article/pii/S1090780710002739

[29] K. Matsuzawa, M. Abe, K. Kose, and Y. Terada, "Oval gradient coils for an open magnetic resonance imaging system with a vertical magnetic field," *Journal of Magnetic Resonance*, vol. 278, pp. 51 – 59, 2017.

[30] R. H. Morris and M. I. Newton, "Magnetic resonance sensors," pp. 21 722–21 725, 2014.

[31] R. Gassert, D. Chapuis, H. Bleuler, and E. Burdet, "Sensors for applications in magnetic resonance environments," *IEEE/ASME Transactions On Mechatronics*, vol. 13, no. 3, pp. 335–344, 2008.

[32] D. Rugar, H. Mamin, M. Sherwood, M. Kim, C. Rettner, K. Ohno, and D. Awschalom, "Proton magnetic resonance imaging using a nitrogen–vacancy spin sensor," *Nature nanotechnology*, vol. 10, no. 2, p. 120, 2015.

[33] J. S. Waugh, *Advances in magnetic resonance*. Academic Press, 2016, vol. 12.

[34] S. H. Koenig, "Ii rabi, f. bloch, em purcell, and the history of nmr and relaxometry," *Encyclopedia of Nuclear Magnetic Resonance, Historical Perspectives*, vol. 1, p. 437, 1996.

[35] R. M. Silverstein and G. C. Bassler, "Spectrometric identification of organic compounds," *Journal of Chemical Education*, vol. 39, no. 11, p. 546, 1962.

[36] H. Y. Carr and E. M. Purcell, "Effects of diffusion on free precession in nuclear magnetic resonance experiments," *Physical review*, vol. 94, no. 3, p. 630, 1954.

[37] R. Damadian, "Tumor detection by nuclear magnetic resonance," *Science*, vol. 171, no. 3976, pp. 1151–1153, 1971.

[38] P. Lauterbur, "Progress in nmr zeugmatographic imaging," *Phil. Trans. R. Soc. Lond. B*, vol. 289, no. 1037, pp. 483–487, 1980.

[39] P. G. Lauterbur and C.-M. Lai, "Zeugmatography by reconstruction from projections," *IEEE Transactions on Nuclear Science*, vol. 27, no. 3, pp. 1227–1231, 1980.

[40] W. Shuman, D. Haynor, A. Guy, G. Wesbey, D. Schaefer, and A. Moss, "Superficial-and deep-tissue temperature increases in anesthetized dogs during exposure to high specific absorption rates in a 1.5-t mr imager." *Radiology*, vol. 167, no. 2, pp. 551–554, 1988.

[41] J. W. Belliveau, B. R. Rosen, H. L. Kantor, R. R. Rzedzian, D. N. Kennedy, R. C. McKinstry, J. M. Vevea, M. S. Cohen, I. L. Pykett, and T. J. Brady, "Functional cerebral imaging by susceptibility-contrast nmr," *Magnetic resonance in medicine*, vol. 14, no. 3, pp. 538–546, 1990.

[42] P. A. Bottomley and C. J. Hardy, "Proton overhauser enhancements in human cardiac phosphorus nmr spectroscopy at 1.5 t," *Magnetic resonance in medicine*, vol. 24, no. 2, pp. 384–390, 1992.

[43] Z. Gan, I. Hung, X. Wang, J. Paulino, G. Wu, I. M. Litvak, P. L. Gor'kov, W. W. Brey, P. Lendi, J. L. Schiano, M. D. Bird, I. R. Dixon, J. Toth, G. S. Boebinger, and T. A. Cross, "Nmr spectroscopy up to 35.2t using a series-connected hybrid magnet," *Journal of Magnetic Resonance*, vol. 284, pp. 125 – 136, 2017.

[44] P. C. Zhi-Pei Liang, Lauterbur, *Principles of magnetic resonance imaging: a signal processing perspective*. The Institute of Electrical and Electronics Engineers Press, 2000.

[45] J. l Mispelter, M. Lupu, and A. Briguet, *NMR Probeheads for Biophysical and Biomedical Experiments: Theoretical Principles and Practical Guidelines*. World Scientific Publishing Co Inc, 2015.

[46] D. Koh and A. Padhani, "Diffusion-weighted mri: a new functional clinical technique for tumour imaging," *The British Journal of Radiology*, 2014.

[47] S. Gitelis, "Bone and soft tissue tumors: Clinical features, imaging, pathology and treatment," 2001.

[48] G. E. Gold, E. Han, J. Stainsby, G. Wright, J. Brittain, and C. Beaulieu, "Musculoskeletal mri at 3.0 t: relaxation times and image contrast," *American Journal of Roentgenology*, vol. 183, no. 2, pp. 343–351, 2004.

[49] S. G. Nekolla, A. Martinez-Moeller, and A. Saraste, "Pet and mri in cardiac imaging: from validation studies to integrated applications," *European journal of nuclear medicine and molecular imaging*, vol. 36, no. 1, pp. 121–130, 2009.

[50] K. N. Kay, T. Naselaris, R. J. Prenger, and J. L. Gallant, "Identifying natural images from human brain activity," *Nature*, vol. 452, no. 7185, p. 352, 2008.

[51] M. A. Fullana, A. Albajes-Eizagirre, C. Soriano-Mas, B. Vervliet, N. Cardoner, O. Benet, J. Radua, and B. J. Harrison, "Fear extinction in the human brain: a meta-analysis of fmri studies in healthy participants," *Neuroscience & Biobehavioral Reviews*, 2018.

[52] K. Sinha and G. R. Sinha, "Efficient segmentation methods for tumor detection in mri images," in *2014 IEEE Students' Conference on Electrical, Electronics and Computer Science (SCEECS)*, March 2014, pp. 1–6.

[53] S. Harjes, G. B. Jameson, V. V. Filichev, P. J. Edwards, and E. Harjes, "Nmr-based method of small changes reveals how dna mutator apobec3a interacts with its single-stranded dna substrate," *Nucleic acids research*, vol. 45, no. 9, pp. 5602–5613, 2017.

[54] Y. Su, L. Andreas, and R. G. Griffin, "Magic angle spinning nmr of proteins: high-frequency dynamic nuclear polarization and 1h detection," *Annual review of biochemistry*, vol. 84, pp. 465–497, 2015.

[55] R. Kausik, K. Fellah, E. Rylander, P. M. Singer, R. E. Lewis, S. M. Sinclair *et al.*, "Nmr relaxometry in shale and implications for logging," *Petrophysics*, vol. 57, no. 04, pp. 339–350, 2016.

[56] W. Yan, J. Sun, Y. Sun, and N. Golsanami, "A robust nmr method to measure porosity of low porosity rocks," *Microporous and Mesoporous Materials*, 2018.

[57] B. Blümich, J. Perlo, and F. Casanova, "Mobile single-sided nmr," *Progress in Nuclear Magnetic Resonance Spectroscopy*, vol. 52, no. 4, pp. 197–269, 2008.

[58] H. B. Caytak, "Signal optimization for unilateral nmr magnet design," Master's thesis, Carleton University, 2011.

[59] E. O. Fridjonsson, S. A. Creber, J. S. Vrouwenvelder, and M. L. Johns, "Magnetic resonance signal moment determination using the earths magnetic field," *Journal of Magnetic Resonance*, vol. 252, pp. 145–150, 2015.

[60] L. B. Casabianca, Y. Sarda, E. Bergman, U. Nevo, and L. Frydman, "Single-sided stray-field nmr profiling using chirped radiofrequency pulses," *Applied Magnetic Resonance*, vol. 46, no. 8, pp. 909–919, 2015.

[61] G. Eidmann, R. Savelsberg, P. Blümler, and B. Blümich, "The nmr mouse, a mobile universal surface explorer," *Journal of Magnetic Resonance*, vol. 122, pp. 104–109, 1996.

[62] Y.-Q. Song, "Magnetic resonance of porous media (mrpm): A perspective," *Journal of Magnetic Resonance*, vol. 229, pp. 12–24, 2013.

[63] D. E. Woessner, "Nmr spin-echo self-diffusion measurements on fluids undergoing restricted diffusion," *The Journal of Physical Chemistry*, vol. 67, no. 6, pp. 1365–1367, 1963.

[64] R. L. Kleinberg, "Nmr well logging at schlumberger," *Concepts in Magnetic Resonance Part A*, vol. 13, no. 6, pp. 396–403, 2001.

[65] J. Loren and J. Robinson, "Relations between pore size fluid and matrix properties, and nml measurements," *Society of Petroleum Engineers Journal*, vol. 10, no. 03, pp. 268–278, 1970.

[66] A. Timur, "Effective porosity and permeability of sandstones investigated through nuclear magnetic resonance principles," in *SPWLA 9th Annual Logging Symposium*. Society of Petrophysicists and Well-Log Analysts, 1968.

[67] R. L. Kleinberg, A. Sezginer, D. Griffin, and M. Fukuhara, "Novel nmr apparatus for investigating an external sample," *Journal of Magnetic Resonance (1969)*, vol. 97, no. 3, pp. 466–485, 1992.

[68] R. Brown and B. Gamson, "Nuclear magnetism logging," *Journal of Petroleum Technology*, vol. 219, pp. 199–201, 1960.

[69] A. Sezginer, D. Griffin, R. Kleinberg, M. Fukuhara, and D. Dudley, "Rf sensor of a novel nmr apparatus," *Journal of electromagnetic waves and applications*, vol. 7, no. 1, pp. 13–30, 1993.

[70] E. Fukushima and S. Roeder, "Spurious ringing in pulse nmr," *Journal of Magnetic Resonance*, vol. 33, no. 1, pp. 199–203, 1979.

[71] R. K. Cooper and J. A. Jackson, "Remote (inside-out) nmr. i. remote production of region of homogeneous magnetic field," *Journal of Magnetic Resonance*, vol. 41, no. 3, pp. 400–405, 1980.

[72] J. Perlo, "Magnets and coils for single-sided nmr," in *Single-Sided NMR*. Springer, 2011, pp. 87–110.

[73] G. Matzkanin, "Review of nuclear magnetic resonance for nondestructively characterizing materials," *Nondestructive Characterization of Materials*, pp. 793–802, 2003.

[74] C. Nicholls and A. De Los Santos, "Hydrogen transient nuclear magnetic resonance for industrial moisture sensing," *Drying Technology*, vol. 9, no. 4, pp. 849–873, 1991.

[75] R. Paetzold, G. Matzkanin, and A. De Los Santos, "Surface soil water content measurement using pulsed nuclear magnetic resonance techniques," *Soil Science Society of America Journal*, vol. 49, no. 3, pp. 537–540, 1985.

[76] N. Goga, A. Pirnau, L. Szabo, R. Smeets, D. Riediger, O. Cozar, and B. Blumich, "Mobile nmr: applications to materials and biomedicine," *Journal of Optoelectronics and Advanced Materials*, vol. 8, no. 4, p. 1430, 2006.

[77] M. Mallett, M. Halse, and J. H. Strange, "Stray field imaging by magnetic field sweep," pp. 172–175, 1998.

[78] J. Godward, E. Ciampi, M. Cifelli, and P. McDonald, "Multidimensional imaging using combined stray field and pulsed gradients," *Journal of magnetic resonance*, vol. 155, no. 1, pp. 92–99, 2002.

[79] W.-H. Chang, J.-H. Chen, and L.-P. Hwang, "Single-sided mobile nmr with a halbach magnet," *Magnetic resonance imaging*, vol. 24, no. 8, pp. 1095–1102, 2006.

[80] J. L. Paulsen, L. S. Bouchard, D. Graziani, B. Blümich, and A. Pines, "Volume-selective magnetic resonance imaging using an adjustable, single-sided, portable sensor," *Proceedings of the National Academy of Sciences*, vol. 105, no. 52, pp. 20 601–20 604, 2008.

[81] J. Perlo, V. Demas, F. Casanova, C. A. Meriles, J. Reimer, A. Pines, and B. Blümich, "High-resolution nmr spectroscopy with a portable single-sided sensor," *Science*, vol. 308, no. 5726, pp. 1279–1279, 2005.

[82] N. R. Routley and K. J. Carlton, "The halo systema light weight portable imaging system," *Magnetic resonance imaging*, vol. 22, no. 8, pp. 1145–1151, 2004.

[83] H. D. Phuc, "Development of portable low field nmr magnet: Design and construction," Ph.D. dissertation, INSA de Lyon, 2015.

[84] P. J. Prado, "Single sided imaging sensor," *Magnetic Resonance Imaging*, vol. 21, no. 3, pp. 397–400, 2003.

[85] B. Manz, A. Coy, R. Dykstra, C. Eccles, M. Hunter, B. Parkinson, and P. Callaghan, "A mobile one-sided nmr sensor with a homogeneous magnetic field: The nmr-mole," *Journal of Magnetic Resonance*, vol. 183, no. 1, pp. 25 – 31, 2006.

[86] B. Blümich, F. Casanova, and S. Appelt, "Nmr at low magnetic fields," *Chemical Physics Letters*, vol. 477, no. 4-6, pp. 231–240, 2009.

[87] R. Nave, "Nuclear magnetic resonance," http://hyperphysics.phy-astr.gsu.edu/hbase/Nuclear/nmr.html, 2001, accessed: 2017-12-20.

[88] G. Coates, L. Xiao, and M. Prammer, *NMR Logging Principles and Applications*. Halliburton Energy Services, 1999.

[89] D. Kaseman and R. Iyer, "Basics of nmr," https://chem.libretexts.org/Core/Physical_and_Theoretical_Chemistry/Spectroscopy/Magnetic_Resonance_Spectroscopies/Nuclear_Magnetic_Resonance/Nuclear_Magnetic_Resonance_II, 2016, accessed: 2015-05-15.

[90] T. James, "Fundamentals of nmr," http://people.mbi.ucla.edu/feigon/M230B/files/James.pdf, 1998, accessed: 2015-05-30.

[91] F. Casanova and J. Perlo, "Nmr in inhomogeneous fields," in *Single-Sided NMR*. Springer, 2011, pp. 11–56.

[92] M. H. Levitt, *Spin dynamics: basics of nuclear magnetic resonance*. John Wiley & Sons, 2001.

[93] M. Hürlimann and D. Griffin, "Spin dynamics of carr–purcell–meiboom–gill-like sequences in grossly inhomogeneous b0 and b1 fields and application to nmr well logging," *Journal of Magnetic Resonance*, vol. 143, no. 1, pp. 120–135, 2000.

[94] D. I. Hoult and R. Richards, "The signal-to-noise ratio of the nuclear magnetic resonance experiment," *Journal of Magnetic Resonance (1969)*, vol. 24, no. 1, pp. 71–85, 1976.

[95] P. Blümler and F. Casanova, "Hardware developments: Single-sided magnets," in *Mobile NMR and MRI*, 2015, pp. 110–132.

[96] S. M. Ng, "Portable nmr-based sensors in medical diagnosis," in *Applications of NMR Spectroscopy*. Elsevier, 2015, pp. 121–146.

[97] B. Wu, S. A. Altobelli, and E. Fukushima, "Single-sequence multi-slice nmr in strong gradient magnetic fields," *Applied Magnetic Resonance*, vol. 48, no. 7, pp. 739–747, 2017.

[98] D. Jiles, *Introduction to Magnetism and Magnetic Materials*. CRC press, 2015.

[99] J. Keeler, *Understanding NMR spectroscopy*. John Wiley & Sons, 2011.

[100] N. Prabhu Gaunkar, J. Selvaraj, L. Bauer, M. Mina, R. Weber, and D. Jiles, "Design and experimental implementation of a low frequency pulsed magnetic field generator," *IEEE Transactions on Magnetics*, vol. 53, no. 11, p. 6501004, 2017.

[101] R. J. Weber, *Introduction to microwave circuits*. IEEE, 2001.

[102] A. Liberman, E. Bergman, Y. Sarda, and U. Nevo, "Faster imaging with a portable unilateral nmr device," *Journal of Magnetic Resonance*, vol. 231, pp. 72–78, 2013.

[103] N. R. Bouda, M. Mina, and R. J. Weber, "High-current magnetic field generator for transcranial magnetic stimulation applications," *IEEE Transactions on Magnetics*, vol. 50, no. 11, pp. 1–4, 2014.

[104] J. W. Pritchard and M. Mina, "Magneto-optic interferometric switch with resonator configuration," *IEEE Magnetics Letters*, vol. 4, pp. 6 000 104–6 000 104, 2013.

[105] J. Selvaraj, W. S. Theh, N. P. Gaunkar, J. Hong, L. H. Bauer, and M. Mina, "Enhancement for high-speed switching of magneto-optic fiber-based routing using single magnetizing coil," *IEEE Transactions on Magnetics*, vol. 53, no. 11, p. 2503904, Nov 2017.

[106] J. Selvaraj, P. Rastogi, N. P. Gaunkar, R. L. Hadimani, and M. Mina, "Transcranial magnetic stimulation: Design of a stimulator and a focused coil for the application of small animals," *IEEE Transactions on Magnetics*, vol. 54, no. 11, pp. 1–5, Nov 2018.

[107] N. R. Bouda, "Methods of magnetic field switching for biomedical and power applications," Master's thesis, Iowa State University, 2015.

[108] P. Rastogi, R. Hadimani, and D. Jiles, "Investigation of coil designs for transcranial magnetic stimulation on mice," *IEEE Transactions on Magnetics*, vol. 52, no. 7, pp. 1–4, 2016.

[109] L. Smaini, C. Tinella, D. Hélal, C. Stoecklin, L. Chabert, C. Devaucelle, R. Cattenoz, N. Rinaldi, and D. Belot, "Single-chip cmos pulse generator for uwb systems," *IEEE Journal of Solid-State Circuits*, vol. 41, no. 7, pp. 1551–1561, 2006.

[110] V. Novickij, A. Grainys, J. Novickij, and A. Lucinskis, "Programmable pulsed magnetic field system for biological applications," *IEEE transactions on magnetics*, vol. 50, no. 11, pp. 1–4, 2014.

[111] N. Prabhu Gaunkar, J. Selvaraj, W.-S. Theh, R. Weber, and M. Mina, "Pulsed magnetic field generation suited for low-field unilateral nuclear magnetic resonance systems," *AIP Advances*, vol. 8, no. 5, p. 056814, 2018.

[112] D. D. Griffin, R. L. Kleinberg, and M. Fukuhara, "Low-frequency NMR spectrometer," *Measurement Science and Technology*, vol. 4, no. 9, p. 968, 1993.

[113] R. L. Kleinberg, A. Sezginer, D. D. Griffin, and M. Fukuhara, "Novel NMR apparatus for investigating an external sample," *Journal of Magnetic Resonance (1969)*, vol. 97, no. 3, pp. 466–485, 1992.

[114] F. Bert, V. Simonet, B. Canals, J. Robert, S. Petit, and H. Mutka, "Local probes of magnetism, nmr and msr: A short introduction," *École thématique de la Société Française de la Neutronique*, vol. 13, p. 03001, 2014.

[115] R. Schadt and A. English, "Acoustic ringing in nmr or rf circuits," *Journal of Magnetic Resonance, Series A*, vol. 108, no. 2, pp. 244 – 247, 1994.

[116] J. Mispelter, M. Lupu, and A. Briguet, *NMR probeheads for biophysical and biomedical experiments: theoretical principles & practical guidelines*. Imperial College Press, 2006.

[117] C. A. Curto, G. Placidi, A. Sotgiu, and M. Alecci, "An open volume, high isolation, radio frequency surface coil system for pulsed magnetic resonance," *Journal of Magnetic Resonance*, vol. 171, no. 2, pp. 353 – 358, 2004.

[118] A. J. Fagan, G. R. Davies, J. M. Hutchison, and D. J. Lurie, "Continuous wave {MRI} of heterogeneous materials," *Journal of Magnetic Resonance*, vol. 163, no. 2, pp. 318 – 324, 2003.

[119] S. Zhang, X. Wu, and M. Mehring, "Elimination of ringing effects in multiple-pulse sequences," *Chemical Physics Letters*, vol. 173, no. 5, pp. 481–484, 1990.

[120] G. A. Morris and M. J. Toohey, "Removal of acoustic ringing from nmr spectra," *Journal of Magnetic Resonance (1969)*, vol. 63, no. 3, pp. 629 – 633, 1985.

[121] I. Gerothanassis, "Methods of avoiding the effects of acoustic ringing in pulsed fourier transform nuclear magnetic resonance spectroscopy," *Progress in Nuclear Magnetic Resonance Spectroscopy*, vol. 19, no. 3, pp. 267 – 329, 1987.

[122] D.-K. Yang and D. Zax, "Suppression of ring-down in noise spectroscopy," *Journal of Magnetic Resonance*, vol. 158, no. 12, pp. 73 – 78, 2002.

[123] A. Peshkovsky, J. Forguez, L. Cerioni, and D. Pusiol, "Rf probe recovery time reduction with a novel active ringing suppression circuit," *Journal of Magnetic Resonance*, vol. 177, no. 1, pp. 67 – 73, 2005.

[124] H. Dong, Y. Zhang, H.-J. Krause, X. Xie, A. I. Braginski, and A. Offenhäusser, "Suppression of ringing in the tuned input circuit of a SQUID detector used in low-field NMR measurements," *Superconductor Science and Technology*, vol. 22, no. 12, p. 125022, 2009.

[125] K. Takeda, Y. Tabuchi, M. Negoro, and M. Kitagawa, "Active compensation of rf-pulse transients," *Journal of Magnetic Resonance*, vol. 197, no. 2, pp. 242 – 244, 2009.

[126] T. Hopper, S. Mandal, D. Cory, M. Hürlimann, and Y.-Q. Song, "Low-frequency NMR with a non-resonant circuit," *Journal of Magnetic Resonance*, vol. 210, no. 1, pp. 69–74, 2011.

[127] L. B. Casabianca, D. Mohr, S. Mandal, Y.-Q. Song, and L. Frydman, "Chirped CPMG for well-logging NMR applications," *Journal of Magnetic Resonance*, vol. 242, pp. 197–202, 2014.

[128] G. Mamniashvili, Y. Sharimanov, T. Gegechkori, A. Akhalkatsi, T. Gavasheli, and D. Gventsadze, "DIPED 2012: Proceedings: XVIIth International Seminar/Workshop on Direct and Inverse Problems of Electromagnetic and Acoustic Wave Theory, Tbilisi, September 24-27, 2012," *DIPED 2012: Proceedings*, 2012.

[129] M. S. H. Akram, Y. Terada, I. Keiichiro, and K. Kose, "Coupled circuit numerical analysis of eddy currents in an open MRI system," *Journal of Magnetic Resonance*, vol. 245, pp. 1–11, 2014.

[130] N. Prabhu Gaunkar, N. R. Y. Bouda, I. C. Nlebedim, R. L. Hadimani, I. Bulu, K. Ganesan, Y. Q. Song, M. Mina, and D. C. Jiles, "Analysis of ringing effects due to magnetic core

materials in pulsed nuclear magnetic resonance circuits," *Journal of Applied Physics*, vol. 117, no. 17, 2015.

[131] N. Prabhu Gaunkar, I. Bulu, Y. Song, M. Mina, and D. C. Jiles, "Detection and estimation of magnetization induced resonances in unilateral nuclear magnetic resonance (nmr) sensors," *AIP Advances*, vol. 7, no. 5, p. 056634, 2017.

[132] K. M. Gilbert, L. Martyn Klassen, and R. S. Menon, "A low-cost, mechanically simple apparatus for measuring eddy current-induced magnetic fields in mri," *NMR in Biomedicine*, vol. 26, no. 10, pp. 1285–1290, 2013.

[133] A. Reiderman, "Ultra-slim nuclear magnetic resonance tool for oil well logging," Jan. 27 2014, *U*S Patent App. 14/164, 265.

[134] T. Phway and A. Moses, "Magnetisation-induced mechanical resonance in electrical steels," *Journal of Magnetism and Magnetic Materials*, vol. 316, no. 2, pp. 468–471, 2007.

[135] J.-I. Park, S. Lee, I. Yu, and Y. Seo, "Inductive detection of magnetostrictive resonance," *Sensors and Actuators A: Physical*, vol. 140, no. 1, pp. 84–88, 2007.

[136] T. Baird, T. Fields, R. Drummond, D. Mathison, B. Langseth, A. Martin, and L. Silipigno, "High-pressure, high-temperature well logging, perforating and testing," *Oilfield Review*, vol. 5, no. 2/3, pp. 15–32, 1993.

[137] S. Yoon and K. M. Krishnan, "Temperature dependence of magnetic anisotropy constant in manganese ferrite nanoparticles at low temperature," *Journal of Applied Physics*, vol. 109, no. 7, p. 07B534, 2011.

[138] K. Maaz, A. Mumtaz, S. Hasanain, and M. Bertino, "Temperature dependent coercivity and magnetization of nickel ferrite nanoparticles," *Journal of Magnetism and Magnetic Materials*, vol. 322, no. 15, pp. 2199–2202, 2010.

[139] N. Prabhu Gaunkar, I. Nlebedim, I. Bulu, M. Mina, R. Hadimani, Y. Song, and D. Jiles, "Broadband analysis of response from magnetic cores used in inductive sensors for pulsed nuclear magnetic resonance applications," *IEEE Transactions on Magnetics*, vol. 52, no. 7, p. 2800404, 2016.

[140] T. Hopper, S. Mandal, D. Cory, M. Hürlimann, and Y.-Q. Song, "Low-frequency nmr with a non-resonant circuit," *Journal of Magnetic Resonance*, vol. 210, no. 1, pp. 69–74, 2011.

[141] C. Hugon, G. Aubert, and D. Sakellariou, "An expansion of the field modulus suitable for the description of strong field gradients in axisymmetric magnetic fields: Application to single-sided magnet design, field mapping and strafi," *Journal of Magnetic Resonance*, vol. 214, pp. 124–134, 2012.

[142] D. Fabri, M. A. Williams, and T. K. Halstead, "Water t2 relaxation in sugar solutions," *Carbohydrate Research*, vol. 340, no. 5, pp. 889 – 905, 2005, conformations of Oligo- and Poly-saccharides.

[143] G. Coates, L. Xiao, and M. Prammer, "Nmr logging: Principles and applications (halliburton energy services, houston, 1999)," *Google Scholar*, pp. 1–234, 1999.

[144] J. F. Jansen, M. J. Shamblott, P. C. Van Zijl, K. K. Lehtimäki, J. W. Bulte, J. D. Gearhart, and J. M. Hakumäki, "Stem cell profiling by nuclear magnetic resonance spectroscopy," *Magnetic Resonance in Medicine: An Official Journal of the International Society for Magnetic Resonance in Medicine*, vol. 56, no. 3, pp. 666–670, 2006.

APPENDIX MEASUREMENTS ON ORGANIC MATERIALS AND CELLS

This chapter discusses measurements on organic media using a commercially developed portable magnetic resonance sensor. In chapter 7, we have discussed the response of ferromagnets to magnetic resonance signals. In this chapter, we present studies of materials which are not strongly ferromagnetic but can be magnetized in the presence of external applied fields (paramagnets). The measurements were performed using a portable NMR system developed by Schlumberger-Doll Research.

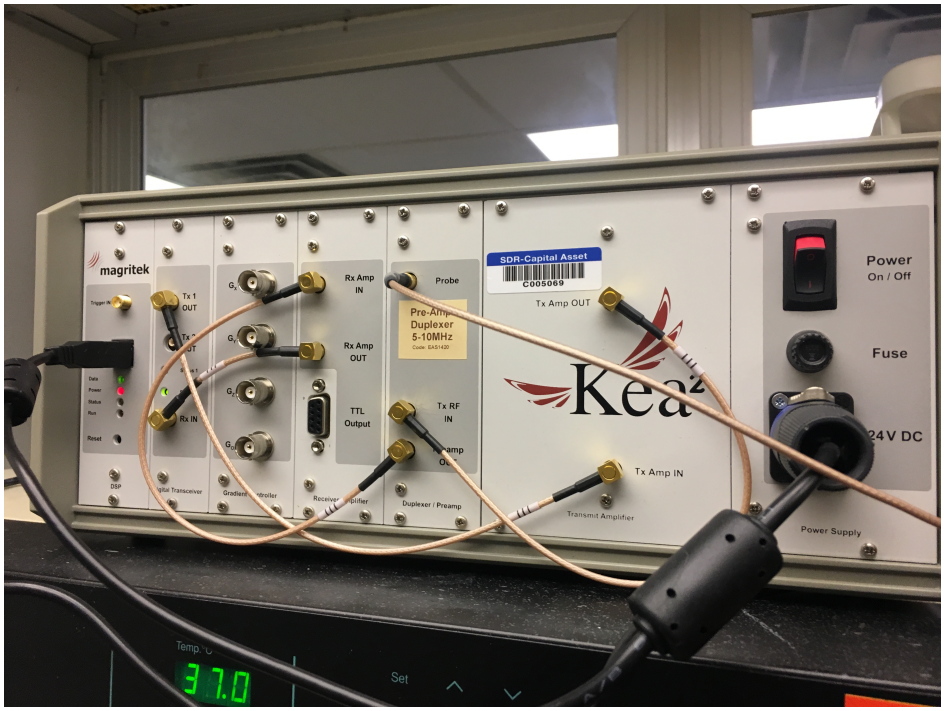

Figure A.1: Measurement system used: Kea2 NMR spectrometer

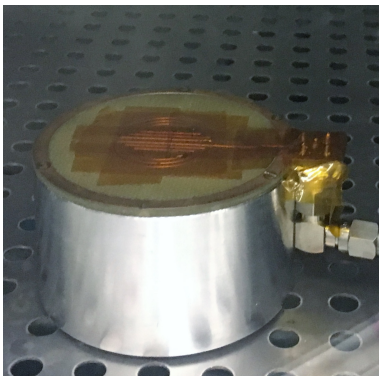

Figure A.2: Permanent magnet sensor. The metal casing encloses 4 permanent magnets (Total height: 0.03 m) and the top surface is the D-coil.

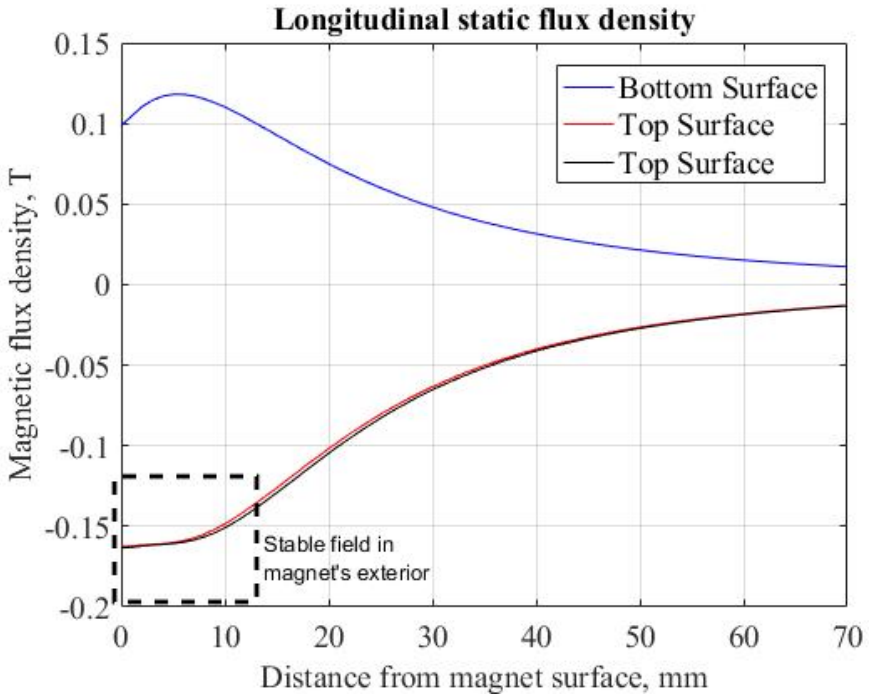

Figure A.3: Magnetic field measured perpendicular to the permanent magnet sensor

The designed system comprised three units, a Kea 2 pulse generation and detection system Fig. A.1 tuned to operate in a frequency range of 5-10 MHz, a portable permanent magnet sensor

comprising of a 0.05 m (outer diameter) x 0.03 m (height) NdFeB ring magnet and a planar double D-shaped coil which was designed to operate at a resonant frequency of 6.7 MHz, both seen in Fig. A.2. The designed sensor has a 10 mm x 10 mm x 10 mm region of sensitivity right above the magnet surface. Therefore, samples can be placed directly on top of the sensor for measurements. The magnetic flux at the exterior of the magnet is shown in Fig. A.3.

From figure A.3, it is seen that a maximum flux density of 0.163 T is obtained up to approximately 10 mm above the magnet surface. For measuring proton NMR, this flux density would correspond to a resonant frequency of 6.85 MHz, however, environmental factors such as temperature and humidity affect the sensor's operation. To study magnetic resonance, a pulsed field is repeatedly applied to the test samples via the D-shaped coil. The Kea2 system has an internal amplifier which may be tuned to operate upto a maximum power level of 100 W. A variety of pulse sequences can be generated using the Kea2 system. Due to the non-uniform field decay in the exterior of the magnet, a CPMG pulse sequence as described in chapter 2 was used for all measurements. The ^{1}H spin-spin relaxation time, T_2 and T_2^* decay times are used as metrics to distinguish between different interactions that exist between paramagnetic species. Two studies were performed using this experimental setup and preliminary findings are described in the following sections.

Examination of sugar solutions

In the initial measurements with this sensor, along with our collaborators we wanted to understand the application space where such sensors could be used. Since the sensor was designed to measure near-surface effects, one choice of biologically relevant experiment was to look into detection of sugar content in human blood, specifically for diabetes detection devices. In order to mimic sugar content in human blood, three different sugar solutions were prepared. The samples chosen were cane sugar, brown sugar and glucose tablets dissolved in water, each with varying weight percentages. Since the response of hemoglobin to an external magnetic field is very weak, these sugar solutions were considered to be a good first approximation of actual human blood samples.

The sugar samples were prepared by weight percentage with a variation from 1 % - 30 % sugar in solution. ^{1}H spin-spin relaxation time or T_2 is estimated via Carr-Purcell-Meiboom-Gill (CPMG) measurements for the sugar solutions. As described in prior work [142], the spin-spin relaxation rate is enhanced for solutions containing carbohydrates and proteins. Therefore, the relaxation rate can be used to indirectly monitor the characteristics of the solute.

Sensor Calibration

To verify the sensor operation, the sensor parameters were first optimized by measuring the response of two water samples, Deionized (DI) water and DI water doped with Nickel chloride. The doped sample was selected since the availability of different ions lead to a faster signal decay time. An operational frequency of 6.7 MHz was selected based on the design of the permanent magnet sensor. The output power level was fixed at -6 dB for the 90^o pulse and -3 dB for the 180^o pulse. Using these settings a pulse duration sweep was performed to identify the optimal pulse width for a 90^o rotation. The pulse duration sweep yielded an operational pulse width of 20 μseconds. The user has a flexibility of choosing the signal power level, operational frequency and pulse duration and can run sweeps on each of these such that an optimal set of parameters is used for measurements. If a non-optimal operational frequency is used, the user will not be able to detect desired NMR signals and most of the measurements will be dominated by noise. A summary of the measurement parameters used for sugar solution measurements is seen in Table. A.1.

Table A.1: Measurement parameters used for DI water and sugar solution measurements

Parameter	Value	Parameter	Value
Frequency	6.7 MHz	Pulse Width	20 μs
Inter-expt time	5 s	Echo time	200 μs
Number of Echoes	4096	Dummy Echoes	2
Pulse Amplitude (90)	-6 dB	Pulse Amplitude (180)	-3 dB
Complex Points	32	Dwell Time	0.5 μs

For the calibration measurements, the test on DI water yielded a T_2 decay time of 1 - 2 seconds and the DI water doped with Nickel chloride yielded a decay time of 500 milliseconds. These are in

the expected decay ranges as per prior literature [92] confirming that the system is sufficiently optimized and calibrated. As seen in equation A.1, the decay time is considered to be a combination of three different effects [143] arising from the bulk solution processes, surface relaxation effects and diffusion in the presence of magnetic field gradients. Each of these effects occur simultaneously. Therefore, assuming the surface decay time to be infinite, the T_2 decay time would include contributions from two sources, namely the bulk media and the diffusion effects.

$$\frac{1}{T_2} = \frac{1}{T_{2,bulk}} + \frac{1}{T_{2,surface}} + \frac{1}{T_{2,diffusion}} \tag{A.1}$$

The diffusion induced relaxation, defined in [143],

$$\frac{1}{T_{2,diffusion}} = \frac{D(\gamma G T_e)^2}{12} \tag{A.2}$$

occurs when a CPMG sequence is applied to materials impacted by magnetic field gradients. Moreover, with extensive field gradients, molecular diffusion contributes to an increase in T_2 relaxation rate [143]. The phenomenon of diffusion does not affect the longitudinal relaxation time T_1. In the equation above, D corresponds to the molecular diffusion coefficient, γ is the gyromagnetic ratio for the proton, G is the field-strength gradient (gauss/cm) and T_e is the inter-echo spacing used in the CPMG sequence. We see that the diffusion relaxation rate will be directly affected by the echo time and the magnetic field gradients. Fig. A.4 plots this and shows that with an increase in echo time, the T_2 decay time decreases. This means that the diffusion effects can be better understood by increasing T_e.

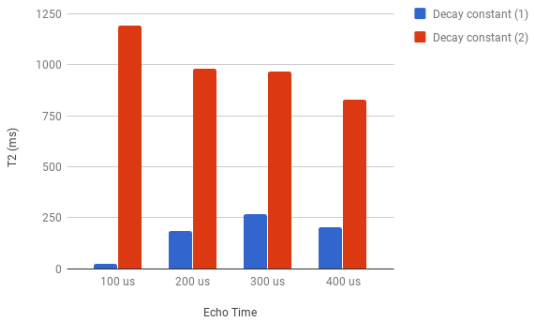

Figure A.4: Effect of echo length on T_2 decay rates

Lastly, it is important to note that if more than one solute interacts with the protons in solution, multiple T_2 decay times can be observed.

Measurements of sugar solutions

As described in literature [142], the presence and interactions of hydroxyl groups with protons can be studied via proton NMR relaxation measurements. In our study, the T_2 decay time for three different sugar solutions, cane sugar, brown sugar and glucose was examined. A bi-exponential fit was used to identify the decay time from the bulk and the diffusion effects respectively. The self-diffusion process of water is assumed to be sufficiently rapid and doesn't affect the decay rate for the proton-hydroxyl interaction.

Since the decay rate is considered to be a combination of internal intrinsic effects and the effect of field gradients and concentration, either term may dominate based on the nature of the solute and interactions between solute and protons in solvent. Generally, bulk decay time is much longer than diffusion induced decay. Here, in Fig. A.5, the variation of decay time for sugar solutions is compared to the calibration sample DI water. It is observed that for all the sugar solutions, T_2 decreases with an increase in sugar concentration. It is noteworthy that the diffusion coefficient is also considered to depend on the sugar concentration. Therefore, besides the bulk decay time, the diffusion decay time is also altered by changes in concentration.

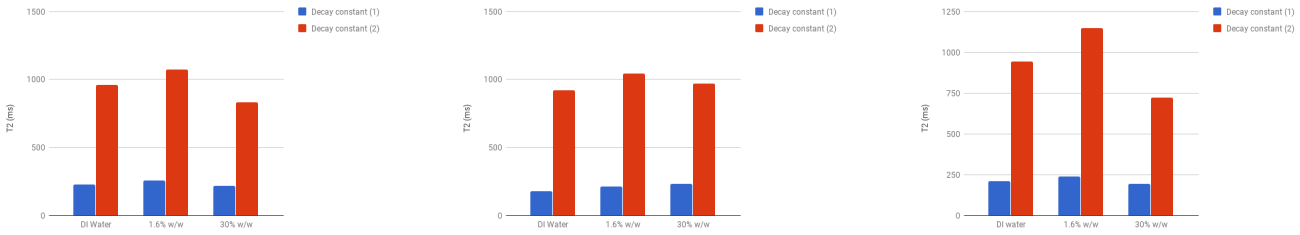

(a) T_2 for cane sugar (b) T_2 for brown sugar (c) T_2 for glucose

Figure A.5: T_2 for different types of sugar solutions in comparison to deionized water

Due to the multi-exponential nature of the T_2 decay, the distribution of decays may be described as in [143],

$$M(t) = \Sigma M(0) e^{-\frac{t}{T_{2i}}} \tag{A.3}$$

where, M(0) corresponds to the initial magnetization from the i^{th} component of relaxation. Then, for the bi-exponential decay, the magnetization, $M(t)$ may be described by,

$$M(t) = M_{bulk}(0) e^{-\frac{t}{T_{2,bulk}}} + M_{diffusion}(0) e^{-\frac{t}{T_{2,diffusion}}} \tag{A.4}$$

As seen in Fig. A.6, the decay rates for 1.6 % sugar solutions are consistently around 1 second. However, the decay rate for glucose is slightly higher than for sugar solutions. Meanwhile, as observed in Fig. A.7, the decay rates for all the sugar solutions decrease with an increase in concentration. Moreover, the glucose solution shows a large reduction in decay rate with an increase in glucose concentration.

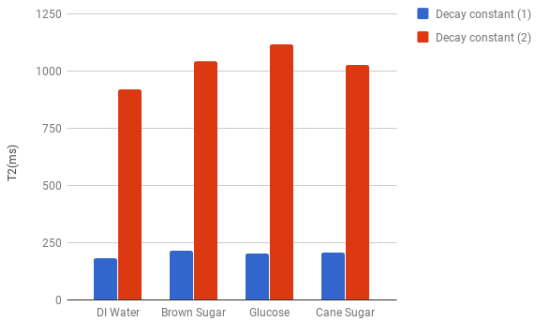

(a) 1.6 % decay time

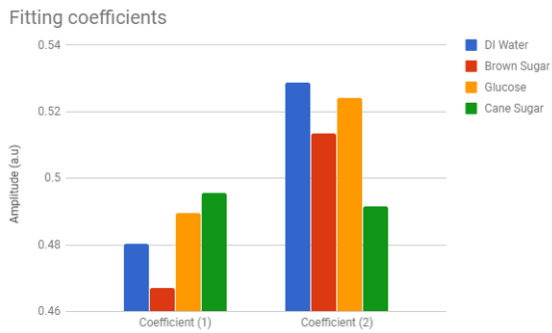

(b) Decay term coefficient

Figure A.6: Comparison of 1.6 weight % solution characteristics

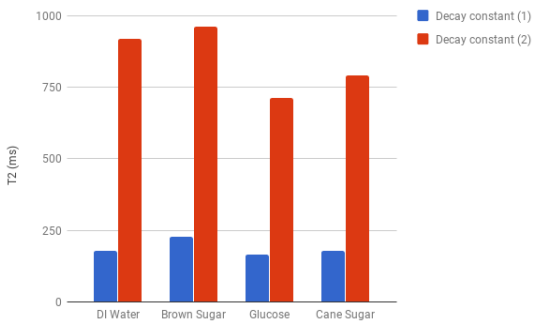

(a) 30 % decay time

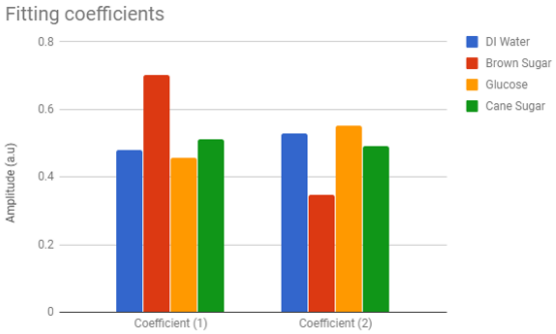

(b) Decay term coefficient

Figure A.7: Comparison of 30 weight % solution characteristics

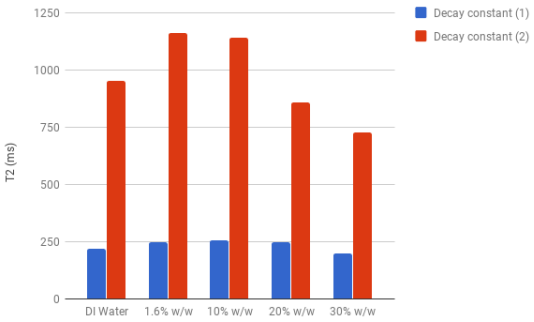

Figure A.8: Comparison of decay rates for glucose solutions

Measurements for 30 % solutions, Fig. A.7, prompted us to further examine the behavior of T_2 decay for glucose solutions with a variation in glucose concentration. As observed in Fig. A.8, with an increase in concentration from 10% to 30 %, the decay time decreased by a factor of half. The change in decay time was insignificant between a 1.6% and a 10% solution. To verify the range of decay times for glucose, the decay characteristics of a comparable sugar, maltose [142] were used. Using a diffusion coefficient of $2.34e^{-9}$ m^2/s for water and the measured T_2 decay times as 0.2 s and 0.8 s respectively, the magnetic field gradients were estimated to be 0.73 T/m and 1.49 T/m. Correspondingly, using a diffusion coefficient of $0.48e^{-9}$ m^2/s for maltose, the effect of diffusion

on the measured T_2 decay time for glucose was estimated. As per Table. A.2, the decay rates for glucose and maltose were comparable, thus validating our experimental measurements.

Table A.2: Comparison of T_2 decay time for glucose (experimental) and maltose (theoretical [142]) solutions

Weight(%)	T_2 (Theoretical)	T_2 (For G = 0.73)	T_2 (For G = 1.49)	T_2
10%	0.1 s	0.1 s	0.1 s	0.2 s, 1.2 s
20%	0.8 s	0.7 s	0.5 s	0.2 s, 0.8 s

All the above experimental measurements suggest that the T_2 decay rate may be used as a valuable parameter for measurements of glucose levels in solutions or even in human blood, thereby serving as a completely non-invasive technique of recording onset of diabetes in humans. Further trials and studies on blood samples will be needed to validate these preliminary observations. However, such measurements are beyond the intended scope of this research.

Examination of stem cells

Stem cells are defined as undifferentiated cells that go on to form various cells which form the human body. These cells are capable of self-renewal [144] and thus have the potential to be extremely valuable in regenerative medicine. Researchers in areas such as tissue engineering are continually seeking new techniques to tackle the issues of cell regeneration and drug delivery. Furthermore, researchers are examining ways of studying cell absorption rates for different drugs. The portable NMR tool can serve as a tool for studying cell absorption rates. As a first test of this system we examine the absorption rate of iron particles in stem cells extracted from rats. While this is a preliminary study, it is expected that the results from this study would enable researchers to study different phenomena at the cellular level using portable NMR sensors.

To study the uptake of particles within stem cells, magnetic resonance experiments were performed using the portable NMR measurement system from Schlumberger Research. The stem cells were prepared by researchers at the Nanovaccine Institute at Iowa State University. The cells were placed within an incubator maintained at 36 ^{o}C with 5% carbon dioxide environment. The sample

of interest was placed in a petri dish atop the permanent magnet sensor as in Fig. A.9. The measurement parameters as in Table. A.3, were calibrated with respect to the cell culture media and also with cells without any iron particles. Frequency, amplitude and pulse width sweeps were performed to obtain optimal measurement parameters. These parameters are summarized in Table. A.3.

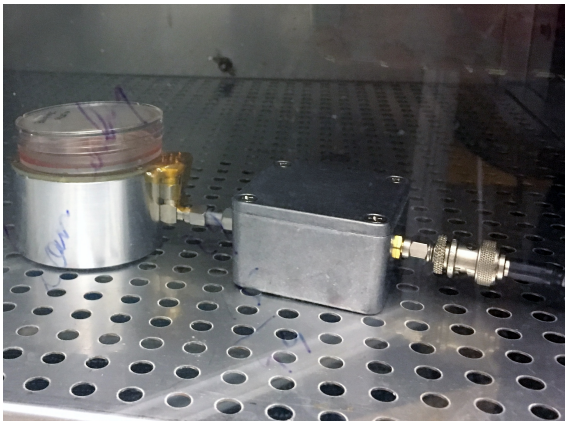

Figure A.9: Stem cell samples placed on permanent magnet sensor

Table A.3: Measurement parameters used for stem cell measurements

Parameter	Value	Parameter	Value
Frequency	6.71 MHz	Pulse Width	18.5 μs
Inter-expt time	5 s	Echo time	200 μs
Number of Echoes	4096	Dummy Echoes	3 - 5
Pulse Amplitude (90)	-10 dB	Pulse Amplitude (180)	-5 dB
Complex Points	32	Dwell Time	0.5 μs
Number of Scans	64	Receiver Gain	40 dB

Similar to the measurements with sugar solutions, two decay rates were assumed, one associated with the bulk material and the other due to diffusion processes. Our study was based on determining if either of these decay rates were affected during the uptake of iron within the cells. Initially, the cell culture media and the stem cells were measured without addition of any iron particles. From Fig. A.10, it is observed that the addition of the stem cells in cell culture media affected the T_2

duration by 20%. However, on addition of the iron particles, as plotted in Fig. A.11 , the T_2 duration initially doubled and then reduced once again by 25% of the original stem cell decay rate.

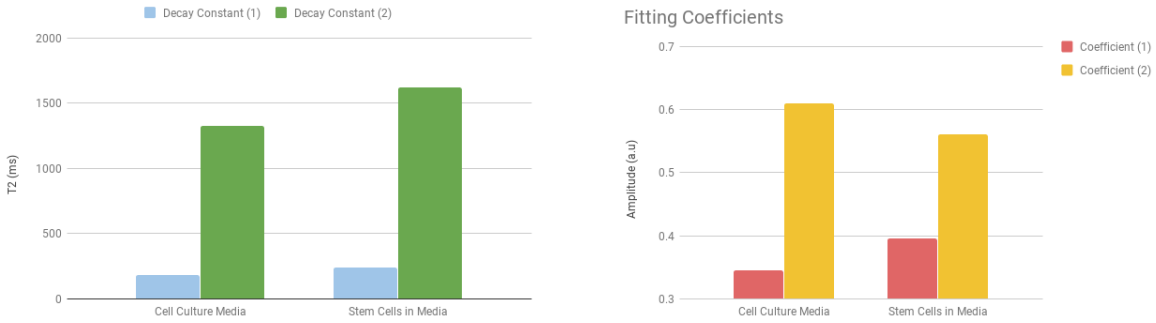

(a) T_2 decay

(b) Decay term coefficient

Figure A.10: Comparison of cell culture media and stem cells

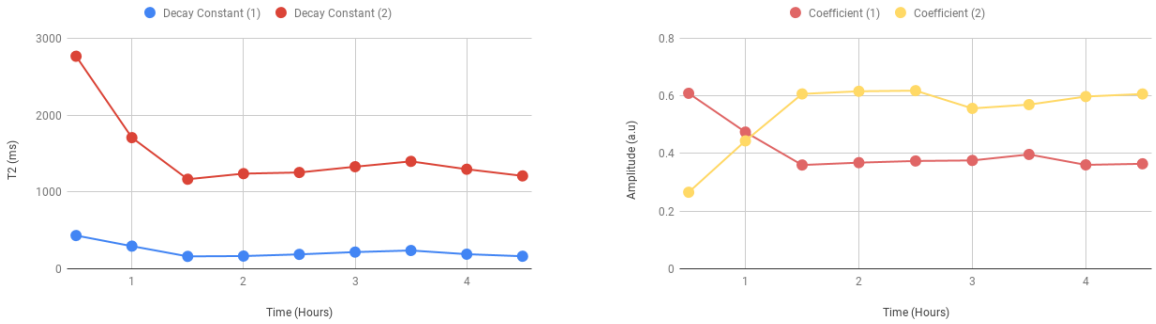

(a) T_2 decay

(b) Decay term coefficient

Figure A.11: T_2 during iron particle absorption process

The iron particle absorption process was studied systematically with a 30 minute interval between each measurement. The sample was placed on the permanent magnet sensor in the interim duration. The researcher's expected that the entire particle absorption process would require approximately 4 hours. Fig. A.11a, shows that after the initial 2 hour time point, the T_2 duration remained constant across all further measurements. Finally, a comparison of the T_2 duration for the

cell culture media and stem cells with or without iron was conducted, Fig. A.12 shows a reduction of T_2 on addition of iron particles to the cells and media.

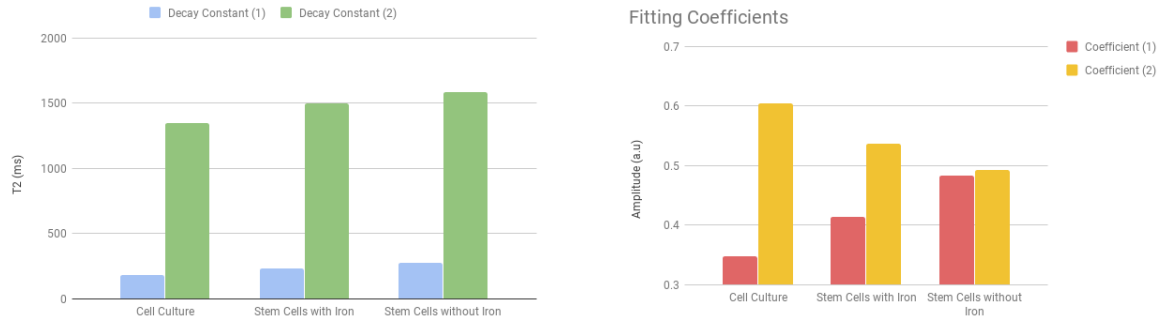

(a) T_2 decay

(b) Decay term coefficient

Figure A.12: Comparison of cell culture media and stem cells

Overall, the observations from Fig. A.11, imply that the iron particle absorption process may occur within a duration of 2 hours and this may be detected via T_2 measurements. While this is a preliminary result, it suggests the utility of the sensor beyond its intended application for oil wells or non-invasive inspections. Further studies may be performed to study the cellular diffusion processes as well as other secondary interactions which might occur during the particle absorption process. One must note that certain basic precautions need to be taken while performing these experiments, while handling the cells and also need to assure that the static field from the permanent magnet doesn't magnetically saturate the particles under investigation.

Future work

The initial measurements demonstrated in this chapter show the breadth of applications where NMR sensors may be used. While our interest was maintained within the realm of biological and organic matter, the applications of the sensor depend on the user's capability of connecting the measured parameters to the phenomenon under investigation. Our preliminary measurements

demonstrate the applicability of such portable magnetic resonance sensors for non-invasive NMR detection for future medical diagnostics and other portable magnetic resonance applications.